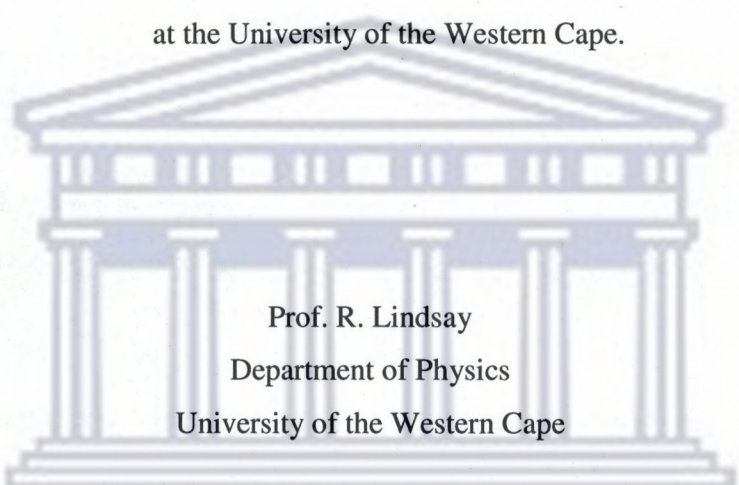


**MEASUREMENTS AND APPLICATIONS OF RADON IN SOUTH
AFRICAN AQUIFER AND RIVER WATERS**

Siddig Abdalla Talha Abdalla

Thesis presented in fulfillment of the requirements for the degree of Doctoral of Physics
at the University of the Western Cape.

Supervisors:



Prof. R. Lindsay
Department of Physics
University of the Western Cape

Prof. dr. R. J. de Meijer
Stichting Earth, the Netherlands

and
The Department of Physics
University of the Western Cape

Dr. R. T. Newman
Group Physics
iThemba LABS

February 2009

DECLARATION

I, the undersigned, hereby declare that the work contained in this thesis is my own original work and that I have not previously in its entirety or in part submitted it at any university for a degree.

Signature:


Date:
Feb. 2009



Measurements and Applications of Radon in South African Aquifer and River Waters

Siddig Abdalla Talha

Department of Physics, University of the Western Cape, Private Bag X17, Bellville, South Africa. Email: stalha@uwc.ac.za

ABSTRACT

In the natural decay series of ^{238}U an inert radioactive gas, ^{222}Rn (radon) is formed in the decay of ^{226}Ra . Because radon is relatively soluble in water, it migrates from places of its generation in rocks and soils to other places either by soil air, or travels with underground water. Therefore, there is a growing interest among hydrogeologists in using radon as a natural tracer for investigating and managing fresh water reservoirs.

This work is aimed at investigating and developing radon-in-water measuring techniques applicable to aquifers and rivers. A gamma-ray spectrometry method using a hyper-pure germanium (HPGe) detector, based at iThemba LABS, Cape Town and Marinelli beakers, has been optimized to measure radon in borehole water *via* the γ -rays associated with the decay of radon daughters ^{214}Pb and ^{214}Bi (in secular equilibrium with their parent). An accuracy better than 5% was achieved. Moreover, long-term measurements of radon in water from an iThemba LABS borehole have been carried out to investigate the role of radon for characterizing aquifers. These investigations led to the development of a simplified physical model that reproduces the time-evolution of radon concentration with borehole pumping and may be used to estimate the time for representative sampling of the aquifer.

A novel method is also proposed in this thesis to measure radon-in-water in the field after grab sampling - a so-called *quasi in-situ* method. The *quasi in-situ* method involves inserting a γ -ray detector in a container of large volume filled with water of interest. The γ -ray spectra are analyzed using an approach involving energy intervals on the high-energy part of the spectrum (1.3 – 3.0 MeV). Each energy interval corresponds to contributions from one of the major γ -ray sources: ^{40}K and the decay series of ^{238}U and ^{232}Th , and cosmic rays. It is assumed that the U interval will be dominated by γ -rays emitted from the radon daughters (^{214}Pb and ^{214}Bi). Minor contributions to an interval with major radionuclide are corrected using an MCNPX simulated standard spectra.

The two methods in this thesis make a significant contribution to measuring and modelling of radon in aquifers and surface waters. It forms a basis for further development in an interactive mode with hydrological applications.

ACKNOWLEDGEMENTS

I am doubly grateful to my supervisor panel consisting of Prof. dr. Rob J. de Meijer, Prof. Robbie Lindsay and Dr. Richard T. Newman for the tireless effort in supervising my thesis amidst their busy schedules. Your scholarly guidance has been immeasurable in light of the detail required for this work. Your availability to share your knowledge and expertise and to devote your time to give comprehensive comment made this work see the light of day. I attribute my deep interest in this field of gamma-ray spectrometry to your motivation and inspiration. You made this possible.

I am highly beholden to iThemba LABS and the Department of Physics, University of the Western Cape (UWC) for not only providing the environment that saw the development and completion of this project, but also for the funding opportunity it provided. The financial assistance and work study opportunity you provided is greatly appreciated. I extend my gratitude to all members of the Lab and the Department in this regard particularly my colleagues Peane Maleka, Nolasco Mlwiolo and Israel N. Hlatshwayo.

Sincere thanks to iThemba LABS-Gauteng for the hospitable and helpful hosts you played during my visit to your Labs. To Dr. U. Horstmann, Prof. B. Th. Verhagen and Mr. M Butler, I say the experience of working with you was enriching to my project.

Many thanks to the collaboration provided by the CSIR people through the radon project (WRC/K5/1685) particularly Dr. J. Bean, Mr. J. Cobbing and Mr. P.J. Hobbs. The partnership you provided gave invaluable input to my project. In the same vein, my thanks extend to the Department of Earth Science, UWC, particularly to Prof. Yongxin Xu, Dr. Shafick Adams and Mr. Shegun Adelana for your endless support during the pumping tests collaboration.

The opportunity to undertake this study would not have been possible without the understanding and support provided by my organization-Sudan Atomic Energy Commission. My earnest appreciation goes to you for granting me leave to pursue this study.

Special thanks to all my friends, especially Mr. Ramadan Ahmed Breima and Dr Adam Khatir Sam. I say your constant encouragement and support meant that I could carry on. Your moral was the spirit that nurtured my determination. Thank you.

My dear Cousin Ustaz Basheer Ibrahim Talha, you gave true expression to brotherhood in your unending encouragement throughout my studies. Your enduring support saw me through all the times. Thank you brother.

Nothing would have reached this point without the foundation planted and made firm by my primary, intermediate, and high school mentors, especially Ustaz Mustafa Al-Tayib Abdalla and Ustaz Ahmed El-Daw Showla (RIP). You laid the rock ground that inspired my dreams. I owe this to you.

To my dear parents, my father Abdalla Talha and my mother Umm Al-Hassan Saleem I could never thank well enough. Yours has been the endurance and sacrifice in abundance and full measure; the pillar of all my endeavors and efforts. I am here because you care. Thank you again.

Finally, my dear Wife: Nosiaba Abdalla Edris. Long way's journey, proves your love and support during the whole course of this work. Special thanks to my daughters Malaz, Marafe and La-alee and Son Abdalla: your existence continues to inspire my work and my life.

To you all, mentioned and unmentioned, I thank you immensely.

Siddig Abdalla Talha

iThemba LABS, February 2009

CONTENTS

CHAPTER 1	Overview and scope of the thesis	1
1.1	Overview of radon in water	1
1.2	Motivation and aim for this study	3
1.3	Scope of the thesis.....	5
CHAPTER 2	Introduction.....	7
2.1	Introduction	7
2.2	Radioactivity	8
2.3	Interaction of radiation with matter.....	10
2.4	Measurement statistics.....	15
2.5	Spectrometry of radionuclides	18
2.6	Radon and hydrogeology	20
2.6.1	Introduction to hydrogeology	21
2.6.2	Radon genesis and transport	23
CHAPTER 3	Radon metrology	28
3.1	Introduction	28
3.2	Alpha spectrometry.....	29
3.2.1	Alpha spectrometry using LSC.....	29
3.2.1.1	LSC (NECSA) and LSC (iTl-G) set-ups.....	30
3.2.1.2	Sampling and measurement procedures	32
3.2.2	The RAD7 radon monitor	33
3.2.2.1	The RAD7 set-up	33
3.2.2.2	Sampling and measurement procedure.....	35
3.3	Gamma-ray spectrometry	38
3.3.1	Using a HPGe detector	38
3.3.1.1	The HPGe set-up	39
3.3.1.2	Sampling and measurement procedures	40
3.3.1.3	The HPGe Calibration procedure	42
3.3.1.4	Simulated HPGe photopeak efficiencies	44
3.3.1.5	Investigation of coincidence summing	45
3.3.1.6	The HPGe and the RAD7 inter-comparison.....	47
3.3.2	MEDUSA technology.....	47
3.3.2.1	Introduction	47
3.3.2.2	The MEDUSA set-up	48
3.3.2.3	The MEDUSA <i>in-situ</i> measurement and analysis procedures	50
3.4	Generation and calibration of standard spectra	53
CHAPTER 4	Radon measurement at the iThemba LABS aquifer.....	56
4.1	Introduction	56
4.2	Sampling and analyses procedures.....	57
4.3	iThemba LABS borehole	59
4.3.1	Site description	59
4.3.2	Borehole casing	61
4.4	Gamma ray spectrometry of ²²² Rn using a HPGe detector	62
4.4.1	Background measurement.....	62
4.4.2	Pumping Tests	63

4.4.2.1	²²² Rn measurements	63
4.4.2.2	Supported radon	66
4.5	Modelling: time evolution of radon concentration.....	67
4.5.1	Model description	67
4.5.2	Model applied to pumping tests.....	68
4.6	Summary and conclusion.....	70
CHAPTER 5	<i>Radon-in-water measurements in mining areas</i>	72
5.1	Introduction.....	72
5.2	Description of sites	73
5.2.1	Study area A: the West Rand Basin (WRB).....	73
5.2.2	Study area B: the Vaal River	75
5.3	Sampling procedures.....	75
5.3.1	Grab samples	75
5.3.2	In-situ measurement.....	77
5.4	Analysis procedures	78
5.5	Results	80
5.5.1	Uranium and supported radon results	80
5.5.2	Total radon results	81
5.5.3	In-situ MEDUSA results.....	84
5.6	Summary, discussion and conclusion	91
CHAPTER 6	<i>In-field radon measurement in water: A novel approach</i>	93
6.1	Introduction.....	93
6.2	Experimental set-ups.....	94
6.3	Spectral analysis using the hybrid approach.....	95
6.4	The KCl measurements	100
6.4.1	The MEDUSA-drum KCl measurements	100
6.4.2	The MEDUSA-tank KCl measurements.....	103
6.5	The ²²²Rn measurements.....	105
6.5.1	The MEDUSA-drum ²²² Rn measurements	106
6.5.2	The MEDUSA-tank ²²² Rn measurements	108
6.6	Background investigations	112
6.6.1	The MEDUSA-drum background measurements	112
6.6.2	The MEDUSA-tank background measurements.....	115
6.7	Geometry effect	120
6.8	Summary, discussion and conclusion	122
CHAPTER 7	<i>Summary, conclusions and outlook.....</i>	124
7.1	Introduction.....	124
7.2	Achievements.....	125
7.2.1	Validation of the HPGe method.....	125
7.2.2	Radon for representative sampling of aquifers	126
7.2.3	A model for predicting time of borehole sampling.....	126
7.2.4	Radon-in-water measurements in mining areas	127
7.2.5	A novel method for measuring radon in the field	128
7.3	Conclusions, outlook and recommendations.....	129
References.....		131

LIST OF FIGURES

Figure 2-1: Schematic illustration of the natural decay series, ^{238}U and ^{232}Th	10
Figure 2-2: Schematic illustration of Compton scattering.....	11
Figure 2-3: Illustration of the relative importance of the photoelectric absorption, the Compton scattering and pair production	13
Figure 2-4: A γ -ray spectrum of KCl dissolved in tap water and measured <i>in-situ</i> using a CsI(Na) detector as an illustration of the various features of γ -rays spectra.	20
Figure 2-5: Schematic illustration of (a) an unconfined aquifer and (b) a confined aquifer including some hydrological concepts related to aquifers.....	22
Figure 2-6: An exaggerated schematic drawing of mineral grains illustrating the radon generation.	24
Figure 2-7: A plot showing the partition coefficient between water and air ($F_{w/air}$) as a function of temperature.....	26
Figure 3-1: Illustration of the various functions of a Liquid Scintillation Counting (LSC) system	31
Figure 3-2: A drawing of the internal detection part of a TR-LSC system showing a sample in its holder surrounded by the BGO guard and viewed by the two PM tubes.....	32
Figure 3-3: A photo and a flowchart of a RAD7 RAD-H ₂ O showing the units and measurement sequences of the RAD7 set-up.....	34
Figure 3-4: Schematic overview of (a) Radon (^{222}Rn) and (b) Thoron (^{220}Rn) decay chains besides an output summery of a typical RAD7 measurement	35
Figure 3-5: Schematic illustration of the HPGe experimental set-up.....	40
Figure 3-6: A photo of radon-tight water sample containers used with the RAD7 and the HPGe measurements.	41
Figure 3-7: Measured (points) and MCNPX simulated (solid line) FEP efficiencies for the HPGe detector in the geometry of screw-top Marinelli beaker	45
Figure 3-8: Correlation between the HPGe and the RAD7 for radon concentration in the range between 1.0 and 45.0 Bq/l.	47
Figure 3-9: A photo and a flowchart showing the various components of the MEDUSA set-up.	49
Figure 3-10: Two MEDUSA measuring geometries: (a) A photo of the MEDUSA detector suspended from onboard a boat in the Vaal River (b) a photo of the MEDUSA detector lying down by the river bank.	52
Figure 3-11: Simulated standard spectra of ^{40}K (dotted-line), ^{232}Th (solid line) and $^{238}\text{U/Rn}$ (dashed-line) for the iThemba LABS MEDUSA detector inserted in a tank filled with water...54	54
Figure 3-12: An HPGe spectrum of ^{238}U decay series including ^{222}Rn simulated with the MCNPX code in geometry of screw-top Marinelli beaker filled to the top.	55
Figure 4-1: A Photo showing two water pumps used in the pumping tests of this study beside the iThemba LABS borehole.....	58
Figure 4-2: A map showing the location of iThemba LABS, where the borehole is situated, in Cape Town, South Africa	60

Figure 4-3: Depth profiles of electrical conductivity (EC) and temperature of the iThemba LABS borehole measured on 11 Aug. 2006.....	62
Figure 4-4: A small part (including two radon related γ -ray peaks) of three spectra of an empty Marinelli beaker, a beaker filled with tap water and a beaker filled with groundwater measured on the HPGe detector.....	63
Figure 4-5: Schematic visualization of the physical model showing the model initial assumptions and elucidating the mathematical derivation of the model.	68
Figure 4-6: ^{222}Rn concentration for test PT5 (~24 hour duration) at a pumping rate of 0.015 m^3/min	70
Figure 4-7: ^{222}Rn concentration for test PT10 (72 hour duration) at a pumping rate of 0.060 m^3/min	70
Figure 5-1: A map showing the two study areas of mining activities near Krugersdorp and Orkney	74
Figure 5-2: Correlation between the various techniques applied to measure radon in water samples collected from the WRB and the Vaal River mining areas.....	84
Figure 5-3: <i>In-situ</i> measurements along the Vaal river with the MEDUSA detector suspended from onboard a boat while it was moving.	86
Figure 5-4: Plot of <i>in-situ</i> measurements along the Vaal river and in front of steams entering the river with the MEDUSA detector suspended from onboard a boat.	87
Figure 5-5: Spectra of <i>in-situ</i> measurements along the Vaal river with the MEDUSA detector suspended from onboard a boat compared to a background spectrum measured in the Theewaterskloof dam	88
Figure 5-6: A spectrum measured with the MEDUSA detector dragged on the Vaal River-bed compared to a background spectrum measured in the Theewaterskloof dam.	89
Figure 5-7: The response (as activity concentration of U, Th and K) of the MEDUSA detector dragged on the riverbed while the boat was moving	90
Figure 6-1 A photo of the iThemba LABS MEDUSA detector mounted on a 210-litre steel drum and on a 1000-liter plastic tank.	95
Figure 6-2: A MEDUSA measured γ -spectrum illustrating the four energy intervals of the hybrid analysis approach.	96
Figure 6-3: A cosmic rays spectrum measured with the MEDUSA detector lowered few centemetrs below the water-surface of the Theewaterskloof dam.....	99
Figure 6-4: A plot of ^{40}K count rate (measured with the MEDUSA-drum geometry) in the interval 0.4 – 1.6 MeV versus the added KCl masses	102
Figure 6-5: The relation between the count rate of ^{40}K in the interval 0.4 – 1.6 MeV and the KCl masses added to the tank filled with tap water.	105
Figure 6-6: The MEDUSA-drum field measurement of U/Rn in a borehole water and a tap water versus the radon concentrations determined by the HPGe detector.	107
Figure 6-7: Radon-in-water concentration (Bq/l) and count rate (cps) measured using the HPGe detector and the MEDUSA-tank set-up, respectively, versus the decay time	110
Figure 6-8: Correlation between Rn concentrations measured in the field (using MEDUSA-tank) and in the laboratory (using the HPGe detector).	111
Figure 6-9: Variations of count rate of U/Rn, Th and cosmic rays measured, in the period of 14 to 16 July 2008, with the MEDUSA detector inside the tank filled with tap water.	119

LIST OF TABLES

Table 2-1: The most significant γ -ray energies (E_γ of $I_\gamma > 2.0\%$) and their branching ratios ($I_\gamma \%$) associated with the decay of various nuclides in the ^{238}U decay series	9
Table 2-2: An estimation of relative γ -ray photons which are attenuated by traversing various distances in water of density 1 g/cm^3 surrounding a detector.....	15
Table 2-3: Some values of the partition coefficient ($K_{w/air}$) of ^{222}Rn between water and air for temperatures in the range from 0 to 100°C	25
Table 3-1: Details of some measurements that are used for estimating the RAD7 collection efficiency.....	38
Table 3-2: FEP efficiencies for the iThemba LABS HPGe detector obtained by dissolving KCl salt in a screw-top Marinelli beaker filled to the top with water.	44
Table 3-3: FEP efficiencies simulated using the MCNPX code for geometry of the HPGe detector and a screw-top Marinelli beaker.....	45
Table 3-4: Average ratio of concentrations obtained by applying the simulated efficiencies to 34 measurements of groundwater samples for investigating coincidence summing effect.	46
Table 4-1: Date, elapsed pumping time, and total radon concentrations for pumping tests PT1 to PT5.. ..	64
Table 4-2: Date, elapsed pumping time and total radon concentrations for pumping tests PT6 to PT10.	65
Table 4-3: Supported radon in groundwater samples from the iThemba LABS borehole.	66
Table 4-4: Details of pumping tests and the model parameters extracted by least squares regression.....	69
Table 5-1: Details of grab samples collected from mining areas including GPS coordinates of sampling points.....	76
Table 5-2: Summary of the <i>in-situ</i> γ -ray spectrometry measurements using the MEDUSA detector.	78
Table 5-3: Measurement mode, sample size, measuring time and the minimum detectable activity (MDA) for the various techniques used in this study to measure radon in water.....	79
Table 5-4: Activity concentrations of ^{238}U , ^{234}U and ^{226}Ra and activity ratios for 10 samples collected together with the radon samples in Table 5-5 from the WRB area.....	81
Table 5-5: Total radon concentration for study area A (WRB) measured using the RAD7, the HPGe, and the LSC (NECSA).....	82
Table 5-6: Radon concentrations of samples collected from study area B and measured using the RAD7, the HPGe, the LSC (iTL-G) and the LSC (NECSA).	83
Table 6-1: Activity concentration of ^{40}K (measured and calculated) obtained from various quantities of KCl dissolved in the drum filled with tap-water.....	101
Table 6-2: MEDUSA-drum gross and net count rate in the interval (0.4 – 1.6 MeV) for the tap-water only and added KCl measurements	101
Table 6-3: KCl salt dissolved in the tank filled with tap water and the corresponding measured and calculated radioactivity concentrations of ^{40}K	104
Table 6-4: MEDUSA-tank gross and net count rate in the energy interval (0.4 – 1.6 MeV) for five KCl spectra and two tap-water spectra	104

Table 6-5: Gross and net count rate in interval III (U/Rn) for various drum measurements	107
Table 6-6: Spectra details and the corresponding radon gross and net count rate in the energy interval III (U/Rn) for MEDUSA-tank measurements	109
Table 6-7: MEDUSA-drum count rate in a number of intervals, for four spectra of KCl dissolved in water, three spectra of tap-water, a spectrum of an empty drum, the Theewaterskloof cosmic ray spectrum and a simulated standard spectrum of Th.....	113
Table 6-8: Cosmics corrected CR for the MEDUSA-drum in the various energy intervals and the corresponding weighted averages CR and the associated chi-square values.....	114
Table 6-9: The cosmics corrected count rates associated with the MEDUSA-drum spectra, listed in Table 6-8, corrected further for thorium contribution	115
Table 6-10: Count rate associated with MEDUSA-tank spectra in the energy interval $1.6 < E_{\gamma} < 3.0$ MeV, subdivided into a number of intervals	116
Table 6-11: The cosmics corrected CR in the subintervals for the measured spectra of Table 6-10 and the corresponding weighted averages CR.....	117
Table 6-12: The cosmics corrected count rates of Table 6-11 corrected further for thorium contribution.....	118
Table 6-13: Mass attenuation coefficients for various γ -ray energies and the corresponding shielding factors.....	121
Table 6-14: Shielding factors determined by dividing the CR of each of the intervals when the tank was empty by those when the tank was filled with water for various heights of the MEDUSA detector from the bottom of the tank.....	122



CHAPTER 1 OVERVIEW AND SCOPE OF THE THESIS

1.1 Overview of radon in water

Radon is a chemically inert, naturally occurring radioactive noble gas, which is relatively soluble in water and in non-aqueous phase liquids. There are three radon isotopes: ^{219}Rn (half-life = 3.96s), ^{220}Rn (half-life = 55.6 s) and ^{222}Rn (half-life = 3.825 days). These isotopes arise from the decay series of ^{235}U , ^{232}Th and ^{238}U , respectively. Because of its much longer half-life ^{222}Rn is the isotope that has proved useful as a natural tracer in the context of hydrogeological processes. Therefore, the term radon (or Rn) in this thesis refers to ^{222}Rn unless otherwise stated.

The applications of radon as a tracer include studies of aquifer flow rates, estimation of groundwater recharge rates, interaction between groundwater and surface water through discharge processes, estimation of groundwater residence times, and to study seismic activities [Bertin and Bourg, 1994; Bonotto and Mello, 2006; Burnett and Dulaiova, 2003; Cook *et al.*, 2003a; Corbett *et al.*, 1997; Dehnert *et al.*, 1999; Dubinchuk, 1981; Ellins *et al.*, 1990; Erees *et al.*, 2007; Hoehn and Gunten, 1989; Hussain *et al.*, 1999, Lehmann and Purtschert, 1997; Papp *et al.*, 2008; Schwartz, 2003; Snow and Spalding, 1997; Tuccimei, 2005; Wu *et al.*, 2004].

For these applications radon-in-water can either be measured in the laboratory after collecting representative samples or measured in-field. For many studies, it is convenient to measure radon concentrations (in water) on site during the field work instead of sending samples to a laboratory for analysis. Field-based measurements allow one to modify the sampling strategy in real time instead of having to wait for laboratory results, which are often only received after the field trip has finished.

Field-based measurement of radon in water has been carried out either by counting α -particles emitted by the radon and its daughters, ^{218}Po and ^{214}Po [Cosma *et al.*, 2008; Burnett and Dulaiova, 2003; Schubert *et al.*, 2006], or by measuring γ -rays emitted mainly by the radon progeny ^{214}Pb and ^{214}Bi [Tsabaris and Ballas, 2005; Osman *et al.*, 2008].

In addition to α - and γ -radiation, radon in water can be detected by measuring the β -decay (and sometimes its associated Cherenkov radiation) or a combination of all the radiation types emitted in the decay of radon or its daughters. Details on the general

radiation detection principles can be found in several textbooks [Debertin and Helmer, 2001; L'Annunziata, 2003; Leo, 1994; Knoll, 2000].

The following types of radiation detectors have been used for the measurement of radon activity concentrations in water:

- **Gamma-ray spectrometers** [Bertolo and Bigliotto, 2004; Bonotto and Mello, 2006; Countess, 1976; Countess, 1978; Danali and Margomenou, 1993; Erlandsson *et al.*, 2001; Farai and Sanni, 1992; Ghose *et al.*, 2000; Hamanaka *et al.*, 1998; Johnston and Martin, 1997; Lucas, 1964; Povinec *et al.*, 2006; Sanchez, *et al.*, 1995; Shizuma *et al.*, 1998; Solecki, 2002; Talha *et al.*, 2008; Takeyasu *et al.*, 2006],
- **Liquid-scintillation counting (LSC)** (radon in scintillator cocktail) [Al-Masri and Blackburn, 1999; Barnett *et al.*, 1995; Cook *et al.*, 2003; Freyer *et al.*, 1997; Hamanaka *et al.*, 1998; Prichard and Gesell, 1977; Prichard, 1983; Vitz, 1991],
- **Solid scintillation detectors** (radon stripped from sample) [Bonotto, 2004; Bonotto and Mello, 2006; D'Alessandro and Vita, 2003; L'Annunziata, 2003a; Lucas, 1957; Mathieu *et al.*, 1988; Oliveira *et al.*, 2003; Snow and Spalding, 1997; Zhuo *et al.*, 2001],
- **Solid-state nuclear track detectors (SSNTD)** [Bowring and Banks, 1995; Durrani and Ilic, 1997; Marques *et al.*, 2004; Singh *et al.*, 1984; Surbeck, 1993; Tommasino, 1990; Vasarhelyi *et al.*, 1997],
- **Alpha-particle spectrometers** [Burnett *et al.*, 2001; Burnett and Dulaiova, 2003; Dulaiova *et al.*, 2005; Lee, 2006],
- **Electret ion chambers** [Amrani and Cherouati, 1999; Dua *et al.*, 1995; Ellins *et al.*, 1990; Kotrappa *et al.*, 1988; Kotrappa *et al.*, 1990; Kotrappa and Jester, 1993],
- **Ionization chambers [IC]** [Pohl and Pohl-Ruling, 1976],
- **Gas proportional chambers** [Vogel *et al.*, 1999], and
- **Cherenkov radiation detectors** [Al-Masri and Blackburn, 1999; L'Annunziata, 2003b].

Gamma-ray spectrometry and α -spectrometry using both LSC and a DurrIDGE RAD7 (www.durridge.com) detector are the methods of choice for this study and will be discussed further in CHAPTER 3.

In South Africa radon has been measured since the 1980s on an irregular basis by various research groups [Vogel *et al.*, 1999; Verhagen *et al.*, 2003; Bean, 2006; Hobbs, 2008]. At present, there are several research groups carrying out studies related to water and they have been trying to link up their ongoing research with radon measurements. Among these groups is the groundwater group at the Department of Earth Sciences, University of the Western Cape and the CSIR Natural Resources and the Environment (www.csir.co.za), in addition to the Water Research Commission (www.wrc.org.za).

1.2 Motivation and aim for this study

As presented in section 1.1, considerable attention has been given to using radon (^{222}Rn) as a unique natural tracer in hydrogeological applications. The high variability of geological formations and consequently hydrogeological systems complicates the task of studying these systems. As a result, numerous studies have been carried out even within one region to study the various hydrogeological systems such as aquifers. With regards to aquifers, most of the studies are derived by either searching for fresh water or protecting existing bodies of fresh water. This is evidenced from the international recognition of the urgent need to manage fresh water resources (constituting less than 0.5 % of all water on Earth) in lakes, rivers and reservoirs, in a sustainable manner. So, for example, sub-Saharan Africa is predicted to experience severe water scarcity by 2025 [Rickwood, 2002]. In terms of a potable resource, groundwater is of particular importance as it constitutes more than 98% of the available supply, with flow in many perennial streams also maintained by aquifer-derived base flow. An understanding of a given aquifer's flow characteristics, and its interaction with adjacent surface water resources, is crucial if the total water resource is to be managed sustainably. Moreover, fractured-rock aquifers predominate in South Africa [Wu *et al.*, 2003], with 40% of the population currently dependent on groundwater supplies. Radon measurements, therefore, have the potential to significantly assist with local water-resource management.

One of the recent efforts at addressing the issue of fresh water in South Africa is that both academia and national research organizations, such as the Water Research Commission (WRC), came to a realization that the full potential of ^{222}Rn as a hydrological tracer is yet to be exploited. This is important since the tracer also has potential applications during pollution studies, particularly in areas adjacent to gold mines in the Witwatersrand Basin where uranium concentrations are relatively high in

gold-bearing deposits and associated mine waste. As such, measurements of ^{222}Rn in water can potentially be used to identify mine-derived water in a given stream. This recognition of using the radon as a hydrological tracer in South Africa led to the launch of a multi-disciplinary project as a joint undertaking between the WRC, the Council of Scientific and Industrial Research (CSIR) in South Africa and the iThemba LABS (Laboratory for Accelerator-Based Sciences: www.tlabs.ac.za). The project explores the use of radon as tracer to assess the possible influence of gold-mining activities on the fresh water aquifers in the West Rand Basin area near Krugersdorp and part of the Vaal River near Orkney.

This latest development of applying radon as a tracer has motivated the work of this thesis. The principle idea is to investigate aspects of radon measurement methodologies within the context of the project with a focus on the available radon measuring techniques. Since there was no dedicated radon measurement laboratory, the logical approach and one of the aims of this thesis is to first optimize a laboratory-based method (since it can be operated under controlled environment) so that it can be used as a reference method. The first available detector at iThemba LABS was a hyper-pure germanium (HPGe) γ -ray detector. Thus the first aim is to *optimize the measurement of radon in water via γ -ray spectrometry using the HPGe detector and screw-top Marinelli beakers*. The optimization involves investigating statistical and systematic uncertainties due to sampling, measurement and analysis. The reason for using the HPGe detector at iThemba LABS for measuring radon in borehole water was due to the availability of a developed borehole (equipped with pump and connected to power), which is convenient for a long-term study of the time evolution of radon concentrations during sampling. The long-term study may also reveal some characteristics of the aquifer to be studied by using radon. This led to the second aim, which is *to develop a model that may describe the radon concentration as function of the pumping time and that includes a dependence on the aquifer*. The third aim is *to develop an in-field radon measurement technique based on a MEDUSA system [de Meijer et al., 1997] that comprises a CsI(Na) scintillation detector*, which is also available at iThemba LABS.

In the endeavor of optimizing the HPGe method or developing an in-field method for measuring radon in-water, one has to keep in mind hydrogeologists' requirements. In hydrogeological applications of radon measurements, minimum detectable activity (MDA) and precision is of primary importance while accuracy is less important. In fact,

if one considers the uncertainties associated with geological and hydrological description of radon-genesis properties of aquifers, an accuracy of 25%, arising from systematic uncertainties, for the method is more than adequate.

When measuring low radon concentrations, the precision can be improved by increasing both the measuring time and the sample volume. However, increasing the measuring time may not be advantageous for some hydrogeological studies especially those involve surveying large areas in a time frame restricted by the half-life of the radioactive tracer. Thus for radon measurements in hydrological applications, particularly field measurements, short measuring times are always a merit. Increasing the sample volume is a trade-off between the accessibility of sample source and obtaining a homogeneous representative sample.

1.3 Scope of the thesis

The rest of this dissertation is organized to consist of six chapters. The basics of radioactivity measurement and of hydrogeological concepts are introduced in CHAPTER 2. The introduction to radioactivity involves discussing interaction of radiation with matter, statistics associated with radioactivity measurement, and spectrometry of radionuclides. The hydrogeological concepts are treated within the context of radon genesis and transport.

The set-ups and general methodologies of radon measurement techniques used in this work are presented in CHAPTER 3. These techniques are: alpha spectrometry using Liquid Scintillation Counting (LSC), α -spectrometry using a DurrIDGE RAD7 radon monitor, and γ -ray spectrometry using a HPGe detector and the MEDUSA system. The HPGe calibration measurements are presented in this chapter as well. In addition to measurements, γ -ray transport was simulated using the MCNPX code [Briesmeister, 2000] for validating various measurements. The generation of γ -ray spectra by means of the MCNPX simulation code is described in section 3.4.

In chapter 4, the measurements of radon in water by γ -ray spectrometry using the HPGe detector for this study are presented. The measurements include pumping tests at a borehole to determine characteristics of a iThemba LABS aquifer. Based on the borehole measurements, a simplified physical model describing the change of radon concentration with the pumping time was developed and applied to the measurements. The model and associated results will be presented in section 4.5.

CHAPTER 5 presents the measurements and results of radon in water in two mining areas: West Rand Basin near Krugersdorp, and the Vaal River near Orkney. The measurements involve grab-sample measurements analyzed by (1) α -spectrometry using the DurrIDGE RAD7 radon monitor, two liquid scintillation counters one at the Nuclear Energy Corporation of South Africa (NECSA) in Pretoria (www.necsa.co.za) and one at the iThemba LABS-Gauteng in Johannesburg, (2) γ -ray spectrometry using the HPGe detector at iThemba LABS - Cape Town and *in-situ* γ -ray spectrometry of radon in the Vaal River using the MEDUSA system.

A novel method for measuring radon in the field is proposed in CHAPTER 6. The method is based on γ -ray spectrometry using the MEDUSA detector placed inside a large container filled with groundwater (using two geometries) and the spectra are analyzed using a new approach. The chapter includes a description of the set-up, the new approach of analyzing the MEDUSA measured γ -ray spectra, the results of calibrating the method and a test of the method by measuring radon in water from the iThemba LABS borehole.

The outcomes of this study are summarized in CHAPTER 7. Conclusions and recommendations for future work are also presented in this chapter.



UNIVERSITY of the
WESTERN CAPE

CHAPTER 2 INTRODUCTION

Two aspects are important when measuring radon in water. One is the measurement principle underlying to radon measurement. The second aspect is related to the use of radon as a tracer within the context of geology and hydrogeology. Since radon is radioactive, the first aspect generally falls within the broad field of radioactivity measurement.

The basics of radioactivity measurement and of hydrogeology concepts in the framework of a multi-disciplinary topic are introduced in this chapter. A brief introduction to radioactivity is presented (section 2.2) followed by a description of the interaction of radiation with matter (section 2.3). Statistics associated with radioactivity measurements is treated in section 2.4. Radon and radionuclides in general may be measured using spectrometry, which is introduced in section 2.5. Finally, the radon genesis and transport are briefly discussed in section 2.6.

2.1 Introduction

Radioactivity is the process in which atomic nuclei decay and emit radiation. This phenomenon has been in existence on earth since its formation. Radionuclides which were already present at the time of formation of the Earth such as ^{235}U , ^{238}U , ^{232}Th , and ^{40}K are called primordial radionuclides. In contrast, radionuclides that have been formed by human activities are called anthropogenic as for example strontium (^{90}Sr) and plutonium (^{239}Pu). In addition, there is the cosmic radiation, which constitutes of particles of high energies that originate from space outside the Earth's atmosphere.

Radioactivity is a unique property of matter and does not generally change with any physical changes of state or chemical transformations. The fact that the behavior of radionuclides is governed by natural laws makes it possible to reliably calculate and measure these radionuclides when they are involved in processes e.g. migration within hydrological systems.

In this chapter, some of the concepts and mathematical relations associated with radioactivity such as the decay law; types of radiation and the way they interact with matter; statistics associated with radioactivity measurements; spectrometry of radionuclides using γ -ray detectors (e.g. HPGe and CsI(Na)) and alpha detectors (e.g. Si ion implanted detectors) are briefly presented [Debertin and Helmer, 2001; Heyde, 1999; Knoll, 2000; Krane, 1988; Lilley, 2001; Leo, 1994].

A presentation on a background to radon in relation with geology and hydrogeology is also given.

2.2 Radioactivity

Natural radionuclides such as potassium (^{40}K), decay series of thorium (^{232}Th) and uranium (^{238}U) are present in soil, rocks and groundwater with various concentrations. Due to their instability, these radionuclides are naturally transformed to their subsequent progeny *via* various decay processes (modes) such as emission of electromagnetic radiation (X- and gamma-rays) and corpuscular radiation (α -particles, β -particles, internal conversion electrons and Auger electrons). Further details on these decay modes can be found in numerous text books [e.g. Debertin and Helmer, 2001; Heyde, 1999; Knoll, 2000; Krane, 1988; Leo, 1994]. Of particular interest to the current work are the decays *via* γ -rays (emitted when a nucleus spontaneously disintegrates to a lower energy state of the same nucleus) and by α - particles (^4He nuclei of discrete energies emitted from the heavy parent nuclei, which are unstable due to unfavorable Z/N ratio of nucleons). The becquerel (Bq), the SI unit of radioactivity, is defined as one disintegration per second.

For any radionuclide, the decay process takes place with a unique decay constant: i.e. the probability per unit time, λ (s^{-1}). The decay constant is characteristic for that particular radionuclide. For a sample of N nuclei the mean number of nuclei decaying during time interval dt is given by: $dN = -\lambda N dt$ (with the minus sign indicating the decrease in numbers). A solution to this equation is given by the radioactive decay law:

$$N(t) = N_0 e^{-\lambda t}, \quad 2-1$$

where N_0 is the number of nuclei at time $t = 0$.

Related quantities to λ are its average or mean lifetime, τ , and its half-life time, $T_{1/2}$. The half-life time is the time required for the original number of nuclei in the sample to decay to half its value while τ is the time for a sample's radioactivity to decay to $1/e$ of its original value. Using Eq. (2-1), it can be shown that:

$$\tau = \frac{1}{\lambda} \text{ and } T_{1/2} = \frac{\ln 2}{\lambda}. \quad 2-2$$

Some radionuclides experience a chain of radioactive decays if the daughter is also radioactive. This chain ends with a stable final nucleus.

Generally, a radionuclide can disintegrate in more than one decay mode. The relative number of atoms that decay by a particular decay mode to the total number of atoms decayed is called the branching ratio (BR).

In a decay chain, a condition called secular equilibrium may occur where the activities of the parent nucleus and of the short-lived daughter ($\lambda_{\text{parent}} \ll \lambda_{\text{daughter}}$) are equal. The secular equilibrium assumption underpins most of the nuclear techniques used for measuring parent radionuclides indirectly through their progeny. For example, ^{222}Rn in water has been determined by measuring the γ -ray photons associated with its progeny ^{214}Pb and ^{214}Bi .

Examples of decay chains are the natural decay series of ^{238}U and ^{232}Th shown in the top and the bottom part of Figure 2-1, respectively. The figure shows the half-lives and decay modes of the members of the decay series: horizontal arrows represent α -decay whereas arrows slanting diagonally down indicate beta decay. The radionuclides printed in bold in shaded boxes are the ones that significantly decay *via* γ -ray emission. The dominant γ -ray emitters in the ^{238}U series, their energies together with their respective emission intensities (I_γ) are presented in Table 2-1. The ^{238}U and the ^{232}Th series contain gaseous isotopes of radon (^{222}Rn in the U-series, and ^{220}Rn in the Th-series). The half-life time of ^{220}Rn is too short for practical measurements in this series, but ^{222}Rn measurements are possible and constitute the main focus of this thesis.

Table 2-1: The most significant γ -ray energies (E_γ of $I_\gamma > 2.0\%$) and their branching ratios (I_γ %) associated with the decay of various nuclides in the ^{238}U decay series [Firestone, 1998].

Radionuclide	E_γ (keV)	I_γ (%)
^{234}Th	63.3	4.8 \pm 0.6
^{234}Th	92.3/92.8	2.8 \pm 0.3
^{214}Pb	241.9	7.50 \pm 0.10
^{214}Pb	295.2	18.5 \pm 0.3
^{214}Pb	351.9	35.8 \pm 0.5
^{214}Bi	609.3	44.8 \pm 0.5
^{214}Bi	768.4	4.80 \pm 0.07
^{214}Bi	934.1	3.03 \pm 0.05
^{214}Bi	1120.3	14.8 \pm 0.2
^{214}Bi	1238.1	5.86 \pm 0.08
^{214}Bi	1377.7	3.92 \pm 0.08
^{214}Bi	1408.0	2.8 \pm 0.4
^{214}Bi	1509.2	2.12 \pm 0.04
^{214}Bi	1729.6	2.88 \pm 0.06
^{214}Bi	1764.5	15.36 \pm 0.20
^{214}Bi	2204.2	4.86 \pm 0.09
^{210}Pb	46.5	4.25 \pm 0.04

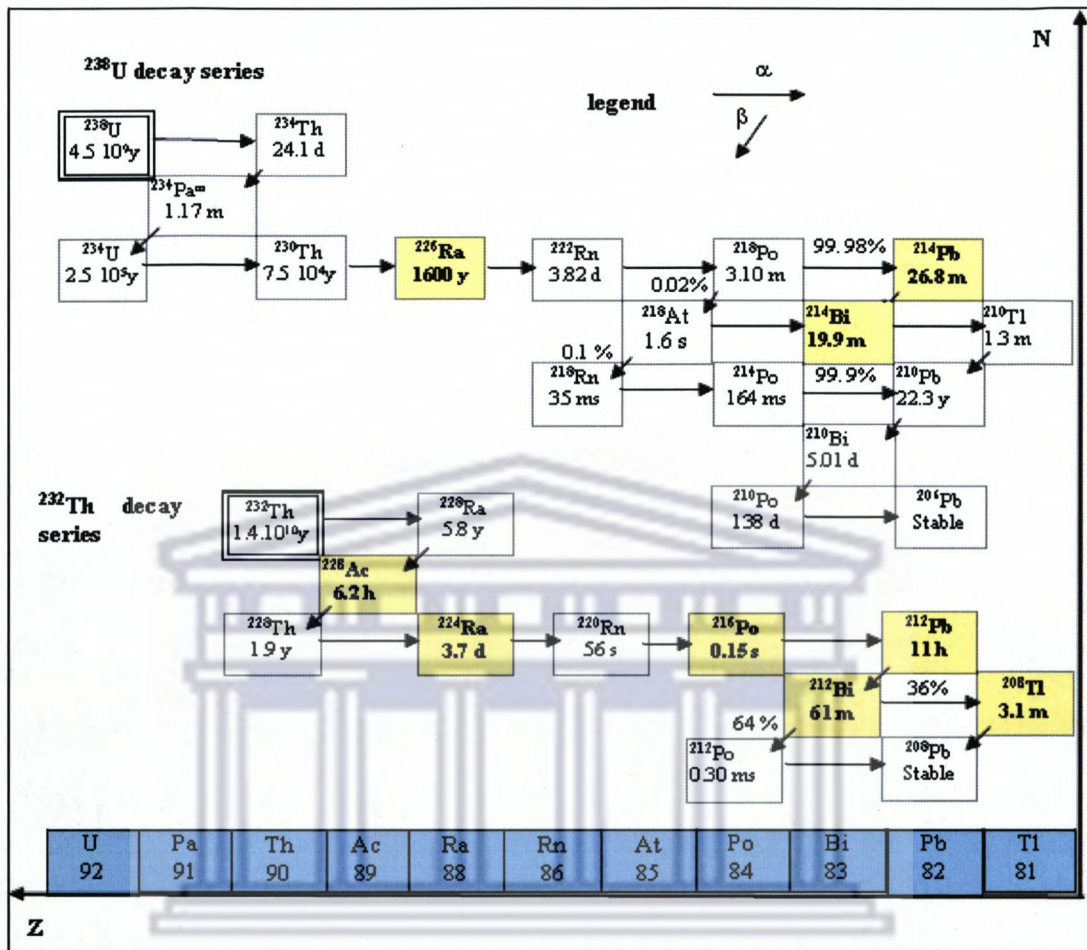


Figure 2-1: Schematic illustration of the natural decay series ^{238}U and ^{232}Th . The half-life ($T_{1/2}$) of each radionuclide is indicated in the box (y: years, d: days, m: minutes and s: second). The radionuclides printed in bold (and in a shaded box) are the ones which decay *via* significant γ -ray emission, while the arrows represent α - and β -decay as indicated in the legend [Firestone, 1998; Krane, 1988].

2.3 Interaction of radiation with matter

The mechanism *via* which the ionizing radiation, such as γ -ray and α/β - particles, loses energy when it passes through materials is important for detecting and measuring these radiations. This section presents some of the various ways in which radiation interacts with matter [Debertin and Helmer, 2001; Knoll, 2000; Krane, 1988; Lilley, 2001; Leo, 1994].

The probability for radiation to interact with matter is expressed as a cross-section. Charged particles like α - and β -particles interact mainly directly with electrons in matter through the Coulomb force and, as a consequence, the electrons are either excited to a higher atomic or molecular orbit or ejected. This leads to ionization in the medium.

The mean distance travelled by α - and β -particles, emitted in natural decay, in air or solid materials is in the range of micrometers and a few centimeters, respectively.

The γ -rays are electrically neutral and have to indirectly interact with matter predominantly through three processes:

- Photoelectric absorption process in which a γ -ray photon is completely absorbed by a bound atomic electron and as a result a photoelectron is ejected. Experimental studies show that the cross-section (per unit mass) for photoelectric absorption, σ_{τ} (m^2kg^{-1}), can be approximated as $\sigma_{\tau} \propto \frac{Z^n}{E_{\gamma}^m}$, where Z is the absorber's atomic number, E_{γ} is the energy of the γ -ray, and ($4 \leq n < 5$) and ($3 \leq m \leq 3.5$). Photoelectric absorption increases with decreasing energy and increases with Z number of the absorbing material. This implies that photoelectric absorption dominates at low energies in high Z materials.

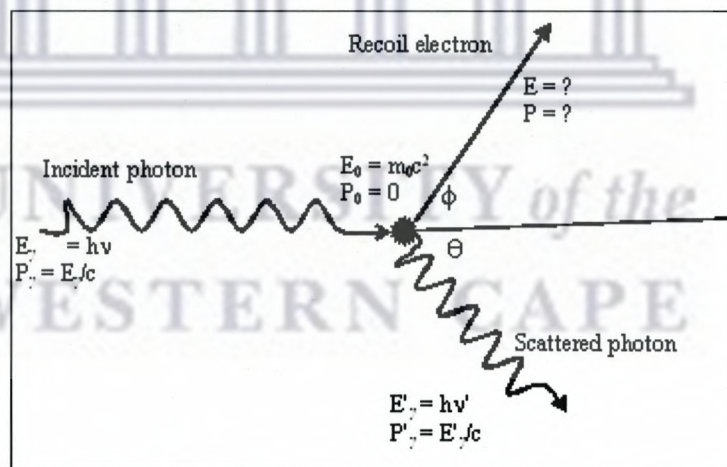


Figure 2-2: Schematic illustration of Compton scattering. An incident photon ($E_{\gamma} = h\nu$) transfers part of its energy to a loosely bound electron which recoils at angle ϕ and the photon scattered at angle θ with energy $E'_{\gamma} = h\nu'$ [Krane, 1988].

- Compton scattering: The process is illustrated in Figure 2-2, which depicts an incident photon transferring part of its energy to a loosely bound outer atomic electron. The photon then scatters at angle θ with energy $E'_{\gamma} < E_{\gamma}$ of the incident photon and the electron recoils at an angle ϕ . Using relativistic kinematics and applying the conservation of energy and momentum, it can be shown that:

$$E'_\gamma = \frac{E_\gamma}{1 + \frac{E_\gamma}{m_0 c^2} (1 - \cos \theta)},$$

2-3

where $m_0 c^2 = 0.511$ MeV is the electron rest mass energy.

In Figure 2-2, the scattering angles can take values from 0° to 180° (head-on collision) and hence the energy transferred to the electron varies from zero at $\theta = 0^\circ$ to a

maximum energy of $T_{\max} (\text{MeV}) = \frac{2 E_\gamma^2 / m_0 c^2}{1 + 2 E_\gamma / m_0 c^2}$ at $\theta = 180^\circ$. This highest value is

called the Compton edge. Thus, in Compton scattering a continuum of energies is transferred to electrons and constitutes the known Compton continuum. The Compton scattering cross-section, σ_c ($\text{m}^2 \text{kg}^{-1}$), is almost independent of Z and inversely proportional to E_γ i.e. $\sigma_c \propto 1/E_\gamma$.

- **Pair production:** In this interaction, a pair of an electron and a positron is created by a photon of energy > 1.022 MeV, in the vicinity of an atomic nucleus. The nucleus is required for momentum conservation. The emitted positron slows down until it eventually interacts with an electron, forming an intermediate state which subsequently annihilates with the electron. In the annihilation two 0.511 MeV γ -rays are emitted in opposite directions. The magnitude of the pair production cross-section, σ_κ , depends upon the absorber atomic number, Z , and incident photon energy, E_γ , and can simply be expressed as: $\sigma_\kappa \propto Z^2 f(E_\gamma, Z)$.

The two annihilation γ -rays either interact further in the material or escape.

Figure 2-3 illustrates schematically the regions in which each of the three processes: photoelectric, Compton and pair production, as functions of the absorber's Z number and the incident photon energy ($h\nu$), dominate. The solid lines show the regions where the probability of two neighboring processes is nearly equal. It can be seen from the figure that the photoelectric absorption dominates the energy range up to $E_\gamma \sim 0.5$ MeV. As the energy of incident photons increase, Compton scattering takes over and dominates the energy range up to $E_\gamma \sim 5$ MeV. The pair-production interaction dominates from $E_\gamma \sim 5$ MeV.

For the natural decay series discussed in section 2.2, the maximum emitted γ -ray (with significant branching ratio) is at energy 2.6 MeV from ^{208}Tl (^{232}Th series). This

means that photoelectric absorption and Compton multi-scattering are the predominant processes in the interaction of γ -rays emitted from natural decay series with matter.

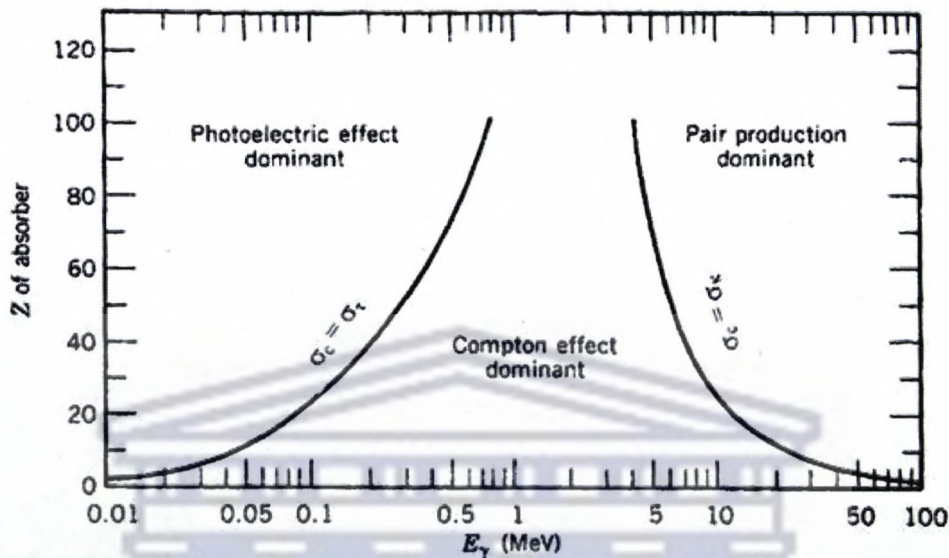


Figure 2-3: Illustration of the relative importance of the photoelectric absorption, the Compton scattering and pair production as functions of incident photon energy (E_γ) and absorbers Z number. The solid lines show regions at which the probability of two neighboring processes is almost equal [Knoll, 2000; Krane, 1988].

For the current work, γ -ray spectrometry was carried out *in-situ* and in the laboratory. Thus, γ -rays that undergo photoelectric absorption in the materials of these detectors or in which the full energy of the Compton scattering is deposited into the detector give rise to the so-called full-energy peaks (FEP) of the γ -ray spectrum as described in section 2.5 and illustrated in Figure 2-4. In case of incomplete energy deposition, Compton scattering contributes only to the Compton continuum.

The three γ -ray interaction processes outlined above are responsible for removing photons from a γ -ray beam passing through a medium before hitting a detector material. This removal or attenuation process is best illustrated by assuming the γ -ray beam to be mono-energetic. The probability per unit path length that the photon can be removed or attenuated from the beam is called the linear attenuation coefficient, μ (cm^{-1}). This linear attenuation coefficient is the sum of probabilities of the three interaction processes: $\mu = \tau(\text{photoelectric}) + \sigma_c(\text{Compton}) + \kappa(\text{pair})$.

The attenuation process of the monoenergetic beam is described by:

$$I = I_0 e^{-\mu x}$$

2-4

where 'I' is the number of photons transmitted, 'I₀' is the number of photons that would have been transmitted if there were no medium and x is the thickness of the medium.

A more practical attenuation coefficient is the mass-attenuation coefficient, μ_m (g^{-1}cm^2) defined as: $\mu_m = \frac{\mu}{\rho}$, where ρ (g/cm^3) is the density of the attenuating medium.

Thus, in Eq. 2-4, μ is replaced by μ_m and the 'x' is replaced with what is called the mass thickness of the medium given in the unit of g cm^{-2} . For the energies relevant to this thesis, where Compton scattering dominates and density can be approximated to be proportional to Z, the cross section for Compton scattering is practically independent of material for a certain energy.

A few mass-attenuation coefficients for water (of density $1 \text{ g}/\text{cm}^3$) and their corresponding γ -ray energies are presented in Table 2-2. The table also shows an estimation of the relative attenuation of γ -rays by traversing various distances in the water. The estimated values were based on Eq. 2-4 and the mass attenuations coefficients taken from Debertin and Helmer, 2001. These estimated values have been used in CHAPTER 6 as a guide for placing a CsI detector in a container filled with water in order to shield the background γ -rays originating outside the container and to measure radon in the water. It can be seen from the table that about 50 cm depth of water can shield more than 90% of the γ -rays associated with natural radionuclides such as ^{40}K and the decay series of ^{232}Th and ^{238}U . It should be pointed out here that Eq. 2-4 is a strong approximation valid for a monoenergetic pencil beam. In practice, γ -rays scatter several times and thereby change direction and energy, thus causing an enhanced transmission often called the build-up effect.

Table 2-2: An estimation of the relative attenuation of γ -rays (%) by traversing various distances in water of density 1 g/cm^3 for several γ -ray energies based on their corresponding mass attenuation coefficients taken from Debertain and Helmer (2001).

E_γ (MeV)	$\mu_m(\text{cm}^2/\text{g})$ For water	Relative attenuated γ -ray photons $(I_0 - I)/I_0$ in %				
		25 cm	40 cm	50 cm	75 cm	100 cm
0.3	0.12	94.9	99.1	99.7	100.0	100.0
0.6	0.09	89.3	97.2	98.9	99.9	100.0
1	0.07	82.9	94.1	97.1	99.5	99.9
1.5	0.06	76.3	90.0	94.4	98.7	99.7
2	0.05	70.9	86.1	91.5	97.5	99.3
3	0.04	62.9	79.6	86.3	94.9	98.1

2.4 Measurement statistics

Measurement of nuclear decay processes is associated with statistical fluctuations. In the context of the current work, measurement statistics is divided into two parts. The first part is the statistics associated with measurements that are produced by a detector and its associated software package, an example being the statistics associated with analyzing FEPs of a γ -ray spectrum. For details of various distributions like Gaussian, Binominal distribution and Poisson distribution, refer to standard text books [e.g. Debertain and Helmer, 2001; Gilmore and Hemmingway, 1995; Knoll, 2000; Leo, 1994; Lyons, 1986].

The second part includes the statistics associated with radioactivity analysis where derived quantities, such as activity concentration and photopeak efficiencies, are to be calculated from measured quantities.

For a set of ' n ' measurements determining one quantity and of equal uncertainties the average and the variance are given by:

$$\mu_x = \frac{1}{n} \sum_{i=1}^n x_i \quad \text{and} \quad \sigma_x^2 = \frac{1}{n-1} \sum_{i=1}^n (x_i - \mu_x)^2.$$

2-5

The square root of σ_x^2 is referred to as standard deviation [Debertain and Helmer, 2001].

When the measurement data are associated with unequal uncertainties, the best estimates are the weighted average and the variance, which are given by:

$$\mu_{wt} = \frac{\sum_{i=1}^n \frac{x_i}{\sigma_{x_i}^2}}{\sum_{i=1}^n \frac{1}{\sigma_{x_i}^2}}, \quad \text{where} \quad \sigma_{wt}^2 = \left[\sum_{i=1}^n \frac{1}{\sigma_{x_i}^2} \right]^{-1}.$$

2-6

The quality of such data can be checked using the chi-square, χ^2 , test where the reduced chi-square, χ_R^2 , is given by:

$$\chi_R^2 = \frac{1}{n-m} \frac{\sum_{i=1}^n (x_i - \mu_{wt})^2}{\sum_{i=1}^n \sigma_{x_i}^2}.$$

2-7

where 'm' is the number of degrees of freedom. A reduced chi-square is a number of a distribution with expectation value 1 and a width depending on the number of degrees of freedom [Bevington and Robinson, 2003]. A value close to unity is an indication of consistent measurement data.

Uncertainties referred to as external, that account for all uncertainties of non-statistical nature e.g. systematic, may be estimated from the χ^2 -analysis as the square root of the variance, σ_{ext}^2 , where $\sigma_{ext}^2 = \sigma_{wt}^2 \chi_R^2$ [Debertin and Helmer, 2001].

Intermezzo 2.1: Variance relations and confidence level

For illustrating the variance associated with combined measurements, we consider two measurements 'A' and 'B', with number of counts N_A and N_B , respectively. Then the variance rules can be approximated as follows [Gilmore and Hemingway, 1996; Dorfman *et al.*, 1980]:

- $\text{var}(N_A \pm N_B) = \text{var}(N_A) + \text{var}(N_B) \pm 2\text{cov}(N_A, N_B)$, i.e. the variance is additive.

The covariance term is to account for interrelation between N_A and N_B . For a single measurement with N counts, $\text{var}(N) = N$. However, caution must be taken as this latter relation is only applied when treating dimensionless numbers such as number of counts.

- $\text{var}(kN_A) = k^2 \text{var}(N_A)$, where k is constant. For example for the count rate $n_A = N_A/T$, the variance is given as: $\text{var}(n_A) = (1/T^2) \text{var}(N_A)$.
- $\text{var}(N_A N_B) \approx (N_B)^2 \text{var}(N_A) + (N_A)^2 \text{var}(N_B) + 2N_A N_B \text{cov}(N_A, N_B)$.
- $\text{var}\left(\frac{N_A}{N_B}\right) \approx \left(\frac{N_A}{N_B}\right)^2 \left\{ \frac{\text{var}(N_A)}{(N_A)^2} + \frac{\text{var}(N_B)}{(N_B)^2} - \frac{2\text{cov}(N_A, N_B)}{N_A N_B} \right\}$.

If a set of data can be assumed to follow Gaussian distribution, the probability of finding a value 'x' in the interval (x_a, x_b) is defined as: $p(x_a, x_b) = \int_{x_a}^{x_b} f(x) dx$ where $p(-\infty, +\infty) = 1$. So, it is very common to characterize the confidence in

determining the value of 'x' by 1σ ; 2σ ; or 3σ . The probabilities associated with these confidence levels are: $p(\mu_x - \sigma, \mu_x + \sigma) = 0.68$, $p(\mu_x - 2\sigma, \mu_x + 2\sigma) = 0.95$ and $p(\mu_x - 3\sigma, \mu_x + 3\sigma) = 0.997$.

The minimum detectable activity (MDA) of the detector system is an often used quantity in the context of radioactivity measurement. The MDA is calculated from a background count rate (n_{Bg}) measured in a geometry and ambient environment similar to that of the sample. At 2σ confidence level, the MDA can be estimated according to [Strom and Stansbury, 1992; Lee *et al.*, 2008]:

$$MDA (Bq/l) = \frac{2.7 + 3.3 \sqrt{T_s n_{Bg} (1 + T_s / T_{Bg})}}{T_s f_d}, \quad 2-8$$

where T_{Bg} and T_s are the background and sample measuring times, respectively, and f_d is an expression that takes into account some of the detector, the γ -ray radiation and the sample parameters.

For the case of a gamma-ray branching out with emission intensity I_γ and FEP efficiency ϵ ($Bq.s$)⁻¹, and sample volume, $V(l)$, the f_d -factor is given by $f_d = I_\gamma * \epsilon_s * V$. Thus, f_d is a conversion factor from counts to concentrations and has dimensions of $(Bq.s.l^{-1})^{-1}$.

Intermezzo 2.2: Uncertainty propagation

Uncertainty propagation is needed in the cases where the value of a physical quantity is derived from a mathematical formula including a number of quantities. For example, the volumetric activity concentration obtained by γ -ray spectrometry using a hyper-pure germanium (HPGe) detector is derived from parameters such as the FEP efficiency, the relative γ -rays intensity, ... etc. In general, uncertainties associated with a quantity $u = u(x; y, \dots)$ are given by:

$$\sigma_u^2 = \left(\frac{\partial u}{\partial x}\right)^2 \sigma_x^2 + \left(\frac{\partial u}{\partial y}\right)^2 \sigma_y^2 + \dots + 2 \left(\frac{\partial u}{\partial x}\right) \left(\frac{\partial u}{\partial y}\right) \sigma_x \sigma_y + \dots \quad 2-9$$

The terms $2 \left(\frac{\partial u}{\partial x}\right) \left(\frac{\partial u}{\partial y}\right) \sigma_x \sigma_y + \dots$ are called the covariance terms, and account for possible linear correlation between each pair of variables. This term is equal to zero when the variables are independent. However, ignoring this term in the calculation of uncertainty potentially leads to underestimating the overall uncertainty (if the

parameters have positive correlation) or overestimating the uncertainty (if the parameters have negative correlation). The linear correlation between variables can also be expressed by a correlation coefficient, $\rho(x, y)$, which is related to covariance by:

$$\rho(x, y) = \frac{\text{cov}(x, y)}{\sigma_x \sigma_y} = 2 \left(\frac{\partial u}{\partial x} \right) \left(\frac{\partial u}{\partial y} \right). \quad 2-10$$

An example of uncertainty propagation that involves a correlation calculation is when applying a model to fit experimental data as for example, the model $\varepsilon(E) = a(E/E_0)^{-b}$, where $E_0 = 1$ MeV. This model has been used in this thesis to fit the HPGe FEP efficiencies for the geometry of a Marinelli beaker in the energy range $0.3 \leq E \leq 1.76$ MeV (more details in subsection 3.3.1.3). The parameters 'a' and 'b' are estimated from fitting the model to the measured efficiencies. The weighted fitting is achieved by applying the least-squares minimization procedure in which one looks for 'a' and 'b' that minimize the sum of square residuals:

$$R^2 = \sum_{i=1}^n \frac{(\varepsilon_i(E) - aE_i^{-b})^2}{\sigma_{\varepsilon_i}^2} \quad 2-11$$

At the minimum, $\partial R^2 / \partial a = 0$ and $\partial R^2 / \partial b = 0$. Analytical solutions for obtaining the parameters are straightforward for linear models (functions). For nonlinear function, as in the efficiency example above, the less time consuming method is by using computation approaches e.g. applying Taylor expansion to the function, see for example Debertain and Helmer, 2001. For this work, commercial statistical packages were used to extract these fitting parameters and their associated uncertainties.

2.5 Spectrometry of radionuclides

One of the objectives of measuring radionuclides is to identify them and determine their concentrations in a geological matrix either directly in the field, *in-situ*, or by taking a representative sample to the laboratory. One way of doing such measurements is through the analysis of the radiation spectrum/spectra associated with the radionuclide (spectrometry). This section introduces some basic concepts and principles associated with γ -ray and α -particles spectrometry [Debertain and Helmer, 2001; Gilmore and Hemingway, 1996; Knoll, 2000].

The properties of the ionizing radiation and its interaction with matter led to the development of measuring systems (detectors and electronics), where the electronics display the response of these detectors to the various radiation interactions. The interaction of radiation with a detector material generates electric charges that are collected to make the electrical signals. In radiation spectrometry, the detectors are operated in what is called pulse mode in which events of radiation interactions are recorded in separate pulses. The amplitude distribution of these pulses is proportional to the energy deposited by radiation incident on the detector's active volume. The output of a detector system is then a pulse-height spectrum in which the number of pulses recorded per channel (or counts per channel) is plotted versus the channel number. The detector set-up may be energy calibrated using for example a reference source and consequently the spectrum could also be presented as count rate versus energy, as illustrated in Figure 2-4 and described in the next paragraph.

One can observe some features of a gamma-ray spectrum in Figure 2-4, which is a spectrum of KCl dissolved in tap water and measured *in-situ* using a CsI(Na) detector (see CHAPTER 3). The figure shows ^{40}K and ^{232}Th FEPs at 1.46 and 2.61 MeV, respectively. The ^{232}Th FEP is due to γ -rays originating from Th present in soil and in building materials around the measurement location. FEPs are described in section 2.3. The part of the spectrum on the left of the K photopeak is the Compton continuum, which is also described in section 2.3. The Compton edge, which occurs at $E_\gamma \sim 1.2$ MeV, is also shown in the figure. The pair-production interaction is not expected to contribute significantly to the spectrum shown in Figure 2-4 because pair-production only dominates at $E_\gamma \geq 5.0$ MeV as can be seen from Figure 2-3. Proper determination of the area under the FEP and its centroid is imperative for identifying unknown radionuclides both quantitatively and qualitatively.

The radionuclide identification also relies on the detector energy resolution, which is defined as the capability of the system to resolve two adjacent peaks. The energy resolution is characterized by the full-width at half maximum (FWHM). The width of the peak is caused by the fluctuation associated with recording the number of pulses. Pulses are proportional to the number of charge carriers, N_{cc} . Thus assuming the charge carriers obey Poisson statistics, the energy resolution can be expressed by:

$$R(E_0) = \frac{FWHM}{E_0} = \frac{2.35}{\sqrt{N_{cc}}}$$

where E_0 is the peak centroid energy. Thus, $R(E_0)$ will decrease as N increases.

It can be noticed that the peaks shown in Figure 2-4 are broad and imply a low number of charge carriers. The energy to create charge carriers, which are light photons in the scintillator detectors such as the CsI that was used to collect the spectrum in Figure 2-4, is about 100 eV. This latter value is high compared to the energy required to create charge carriers (electron-hole pair) in semiconductors; only 3 eV. This means that for a particular γ -ray energy the number of charge carriers is less in scintillation detectors than it is for semiconductors.

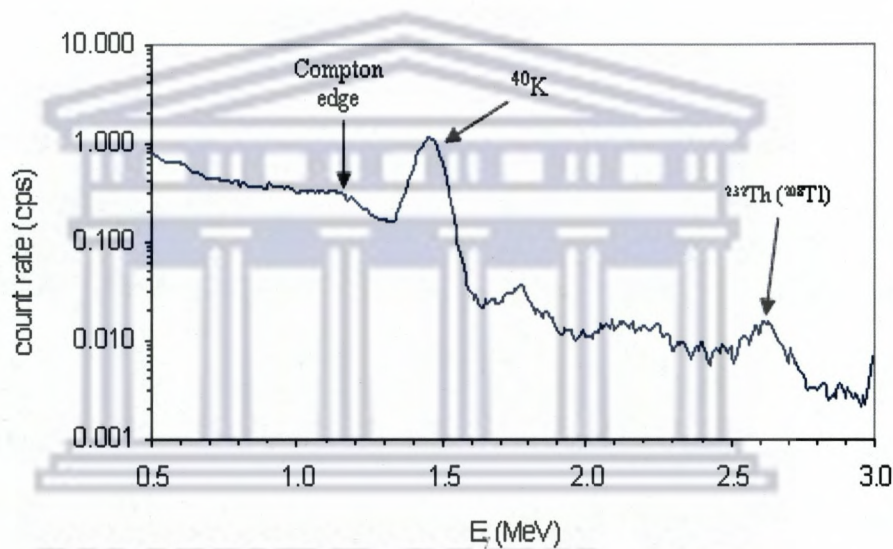


Figure 2-4: A γ -ray spectrum of KCl dissolved in tap water and measured *in-situ* using a CsI(Na) detector. The spectrum illustrates the detector response due to interaction of various γ -rays with the detector's material. The ^{40}K and ^{232}Th peaks shown are photopeaks due to photoelectric absorption and full deposited energy of Compton interaction. The part designated Compton continuum is mainly due to K (1.46 MeV) photons Compton scattered (inside the detector material) at various angles reaching the Compton edge at scattering angle of 180° . This Compton edge corresponds to $E_\gamma \sim 1.2$ MeV.

2.6 Radon and hydrogeology

The half-lives of natural radionuclides such as the radionuclides in the U and Th decay series range from microseconds to billions of years and as such have been used as natural clocks for studying various hydrological processes [Clark and Fritz, 1997; Lehmann and Purtschert, 1997]. For example, measurements of ratios of activity concentrations less than unity or much greater than unity characterize the state of disequilibria between the members of the U and Th decay series. This is more pronounced in the ^{238}U series due to the greater solubility of U (dissolved and

transported as U^{6+}) as compared to Th during chemical weathering [Kraemer and Genereux, 2000]. Both equilibrium and disequilibrium in the ^{238}U decay series have been utilized to study geological and hydrogeological systems [Dosseto *et al.*, 2008; Vigier *et al.*, 2001; Suksi, 2001; Andersson *et al.*, 1995; Kronfeld *et al.*, 1994].

Radon is produced by alpha decay of radium in the natural decay series of uranium (U) and thorium (Th) as can be seen in Figure 2-1. The U and Th have the tendency to be enriched in molten or partially melted rocks at the time of formation of igneous and metamorphic rocks. Therefore, U and Th are mobilized by both geological and hydrogeological processes and precipitate in permeable places. Eventually, radon is formed from the radioactive decay of radium in the decay series of U and Th. As explained in CHAPTER 1, the main radon isotopes are ^{222}Rn (in the ^{238}U series) and ^{220}Rn (in the ^{232}Th series). ^{222}Rn has a diffusion distance of about 220 cm in air and 2.2 cm in water. The diffusion distance, defined as $\sqrt{D\tau}$, is the distance traversed by the radon over its mean life time, τ , where D (m^2s^{-1}) is the diffusion coefficient. The diffusion distance of ^{220}Rn is 2.85 cm in air and 0.0285 cm in water [Durrani and Ilić, 1997]. Hence, ^{222}Rn is the most useful isotope in the context of hydrogeological applications.

To make use of radon as a hydrogeological tracer, a better understanding of geology (pertaining to radon genesis) and hydrogeology (for radon transport) is required. This section presents an introduction to geology and hydrogeology. The section comprises two parts; the first part introduces some concepts of hydrogeology. The second part presents a short background to radon genesis and transport in connection with its progenitors and the various geological formations.

2.6.1 Introduction to hydrogeology

The terms hydrogeology and geohydrology refer to the distribution and movement of groundwater in soils and rocks of the Earth's crust. Regions in which all pore spaces are filled with water is referred to as the saturated zone (or phreatic zone); and the region in which some of the pore spaces are filled with air is called the unsaturated zone (or vadose zone). The water that is held between the soil's pore spaces and in rock fractures and micro-fissures is what one can term groundwater. In the Earth's crust, layers of weathered rocks are in most cases underlain by consolidated rock, of variable thickness, that is given the term bedrock. The underground layers of permeable rocks or permeable

unconsolidated materials, such as gravel, silt, sand and clay, which contains extractable groundwater, are known as aquifers.

Two types of aquifer are illustrated in Figure 2-5. Figure 2-5a shows an unconfined aquifer, which is hydraulically connected to the ground surface, i.e. can receive recharge water directly from the surface. The term phreatic aquifer is used interchangeably with unconfined aquifer. Confined aquifers, as opposed to unconfined, are water-bearing layers that lie between two impermeable rocks (confining beds). Figure 2-5b depicts a well tapping a confined aquifer with an illustration of the cone of depression and potentiometric surface [Kelly, 2006].

When groundwater is withdrawn from an unconfined aquifer e.g. by pumping a well, a gradual drop (of a conical shape) in the water table develops around the well. This drop of the water table is called the cone of depression, which influences the radon transport in the unconfined zone above the water table. For confined aquifers, the hydrostatic potential raises the water in a well that taps the aquifer. An imaginary surface at the level to which the water in the well would rise is called the potentiometric surface. Another characteristic of a confined aquifer is that when the recharge point is higher than the point of discharge, as for example the well tapping the aquifer, the groundwater may freely flow at the surface. This particularly occurs when the surface is low enough to the extent that it intersects or passes below the level of the water table. In such a case, the wells from which water flows at the surface are called artesian wells. In addition, the water flow at the surface could also form water bodies such as swamps, oases, lakes, and springs.

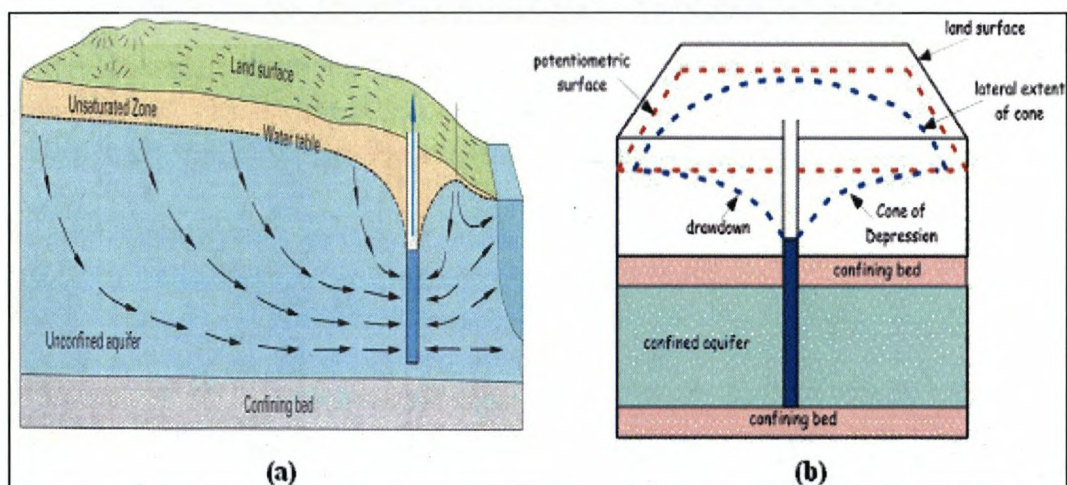


Figure 2-5: Schematic illustration of (a) a well tapping an unconfined aquifer, a confined bed, an unsaturated zone and a water table. (b) a well tapping a confined aquifer with illustration of cone of depression and potentiometric surface [Kelly, 2006].

Pumping of groundwater from a well/borehole for studying aquifer system characteristics *in-situ* is called a pumping test. In the field of hydrogeology, the pumping test studies includes, but are not limited to, collecting data of water levels, time-drawdown, distance-drawdown, etc. These data are then analyzed with the help of pumping test models to derive further parameters related to the characteristics of the aquifer [Walton, 1987].

In this work, the *in-situ* measurements during pumping tests include determining radon in water concentrations. The details of these pumping tests will be discussed in CHAPTER 4.

2.6.2 Radon genesis and transport

Uranium in a +6 oxidation state forms soluble compounds and eventually gets mobilized by groundwater. The U then precipitates in permeable places, such as fissures, of chemically reducing conditions. However, this leaching and fixation process is unstable because of the changing oxidation/reduction conditions in groundwater systems. Locally, in a range of a kilometer square, U and ^{226}Ra (the parent of ^{222}Rn) concentration may vary with types of soil or along shallow faults and fractures [Cothorn and Smith, 1987].

A ^{226}Ra atom, residing in a mineral grain, decays by ejecting an α -particle (^4He) and forms a ^{222}Rn atom that recoils in a direction opposite to that of the α -particle. By this recoil process, the ^{222}Rn atom may be released (emanate) from the mineral grains. This process is called direct recoil emanation which is the dominant radon emanation process. Depending on the grain density, the direction of recoil and the location of the ^{226}Ra atom in the grain, the radon atom moves a distance of 0.02 to 0.07 μm and could possibly land in a pore space [Durrani and Ilić, 1997]. Figure 2-6 illustrates how some radon atoms have been able to emanate from the grains. The emanation occurs when radon atoms recoil in a direction of adjacent air pores or water-filled pores. If the pore space is filled with air, the radon atom may cross the pore space and get imbedded and immobilized in an adjacent grain. The range of the recoil radon atom in water is less compared to its range in air, therefore, the radon atom may end up in water and hence the emanation rate increases with increasing pore water.

Radon concentration in air pores or in water filled pores is determined by the number of radon atoms emanated into the pore space, the porosity (ratio of pore volume to total volume), and the water content of the soil. In addition, these radon

concentrations decrease because some of the radon atoms are moved away from the source either with the moving soil air or with the flowing water.

Under the condition of no ventilation, the maximum radon concentration in a soil's pores filled with air or water, C_{\max} (Bq m^{-3}), is given by [Durrani and Ilić, 1997]:

$$C_{\max} = Aed \frac{1-p}{p}$$

2-13

where A is the specific activity (Bq kg^{-1}) of ^{226}Ra in the soil, ' e ' is the emanation coefficient (the ratio of total amount of radon that emanate to the pore space to the radon produced in the mineral grains [DeWayne and Green, 2000]), ' d ' is the compact density (normal for mineral soils = 2700 kgm^{-3}) and ' p ' is the porosity. C_{\max} is sometimes called equilibrium concentration where the radon concentration in water is in secular equilibrium with emanation from the aquifer rocks.

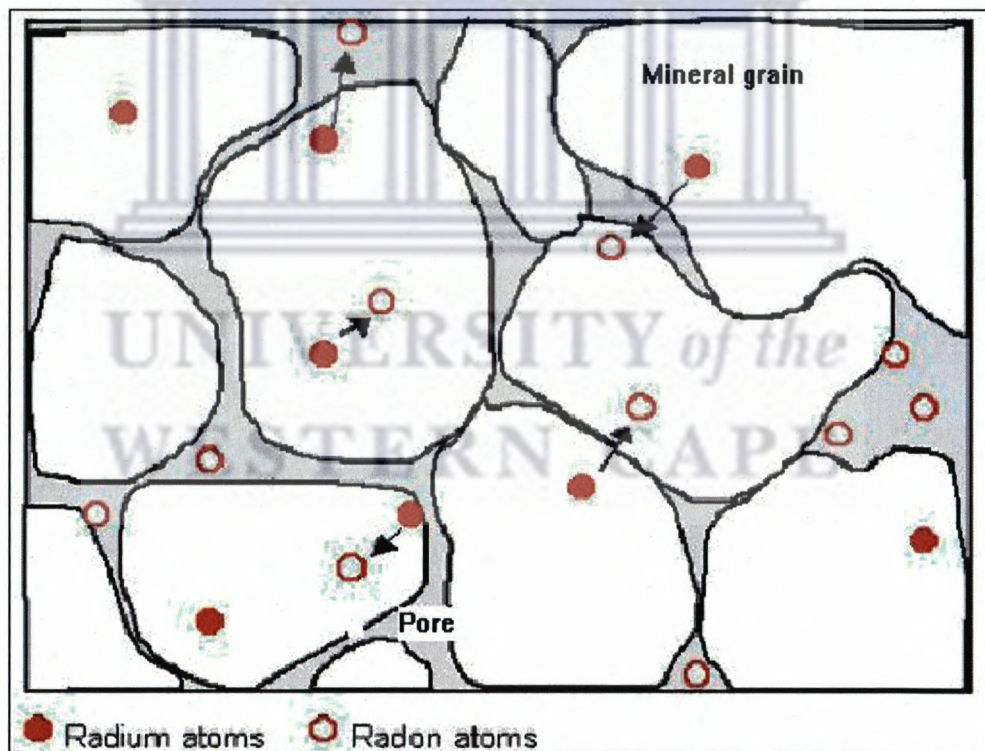


Figure 2-6: An exaggerated schematic drawing of a suite of mineral grains illustrating the radon generation. Radium atoms decay to radon and the radon atoms are dislodged from the grain by the recoil process. Some of these atoms may emanate to the pore space that are filled with water or air from which radon could be transported further by geo-gases or water flow. Adapted from Speelman (2004).

The emanation rate, e , is generally vary with the grain size. For example, e is higher for fine clay than it is for sand. However, the radon emanation could be high even for

coarse grains due to high concentration of ^{226}Ra resulting from the initial weathering of these mineral grains.

The distribution of radon in the pores between water and air phases depends on the water temperature and the atmospheric partial pressure of radon. When radon concentration reaches equilibrium between water and air, the partition coefficient is called the Ostwald solubility coefficient¹, which decreases with temperature. Because of this partitioning, radon in water has been determined by measuring radon in air degassed from the water in question [e.g. Surbeck, 1996; Schubert *et al.*, 2006]. Table 2-3 shows values of the partition coefficient at various temperatures taken from two references. The partition coefficient dependence on temperature T (in °C) has also been parameterized by the relation [Kluge *et al.*, 2007]:

$$K_{w/air}(T) = 0.105 + 0.405e^{-0.0502T}$$

2-14

Table 2-3: Some values of the partition coefficient ($K_{w/air}$) of ^{222}Rn between water and air for temperatures in the range from 0 to 100 °C [Cecil and Green, 2000].

Temperature (°C)	Partition coefficient ($K_{w/air}$)
0	0.51
0	0.53 ^{*2}
5	0.42
6	0.43*
10	0.35
15	0.28*
20	0.255
26	0.22*
30	0.2
40	0.16
50	0.14
60	0.127
70	0.118
80	0.112
90	0.109
100	0.107

¹ In the context of radon, the Ostwald coefficient represents the radon solubility per volume in water and is defined as “the ratio of the concentration of gas per unit volume of liquid phase to the concentration of gas per unit volume of gas phase” [Davis *et al.*, 2002]. This definition is based on atmospheric partial pressure of the radon and the coefficient is expressed as $\text{g mol } l^{-1}(\text{of liquid}) / \text{g mol } l^{-1}(\text{of vapour})$.

² Values marked with * are taken from Durrani and Ilić (1997).

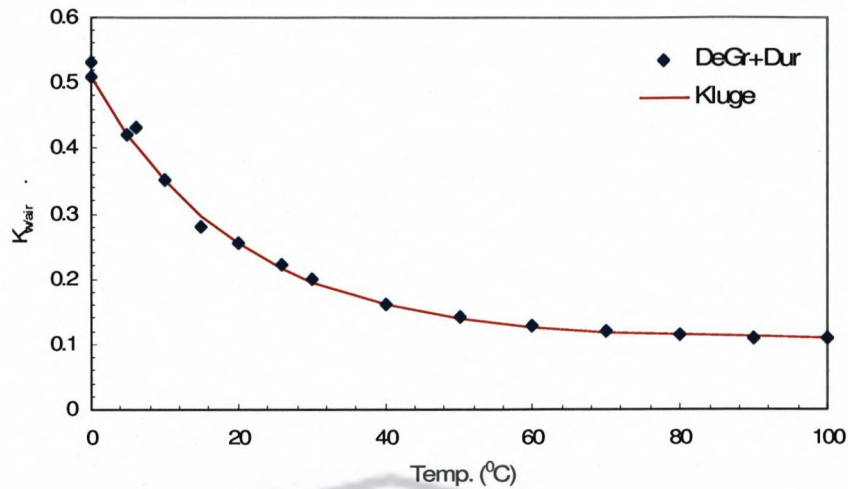


Figure 2-7: Partition coefficient between water and air ($F_{w/air}$) as a function of temperature. The data points were taken from DeWayne and Green, 2000 and Durrani and Ilić, 1997. The fit (solid line) was obtained using Eq. 2-14 [Kluge *et al.*, 2007].

The $K_{w/air}$ values presented in

Table 2-3 are plotted against temperature as shown in Figure 2-7, and fitted with Eq. 2-14. It can be seen from Figure 2-7 that there is good agreement between the data and the solid line obtained from the equation.

Generally, the radon content in air pores is higher than that in water filled pores. Taking the percentage of water in the pores (F) and the partition coefficient ($K_{w/air}$) into consideration, the maximum radon concentration in the air pores, some of which are filled with water, can be estimated by:

$$C_{\max} = \left\{ Aed \frac{1-p}{p} \right\} [F(K_{w/air} - 1) + 1]$$

2-15

The diffusion coefficient of ^{222}Rn , D (m^2s^{-1}), is small in water ($10^{-9} \text{m}^2\text{s}^{-1}$) compared to that in air ($10^{-5} \text{m}^2\text{s}^{-1}$). Therefore, for soil below the water table, the radon is unlikely to move by diffusion. If the water is stagnant, the radon content in completely water-filled pores reaches a maximum in a similar way as the air pores given by Eq. 2-13. The increase of water content in the pores increases the radon emanation and exhalation from that soil. As a result, radon concentration in these types of water has been found to exceed the equilibrium radon concentration in air.

In fault zones and fracture bedrocks, high radon concentrations have been attributed to the fact that geo-gasses (such as CO₂, CH₄ and N₂) carry radon from its source at bedrock surfaces where uranium and its decay series were precipitated [Durrani and Ilić, 1997].

Regarding radon transport in liquids, liquid diffusion transports radon from microcrystalline fractures in grains into pore spaces of aquifers. Unlike its parents' uranium and radium, radon is chemically inert and, therefore, it is transported by water flow without hardly any chemical interaction. The only constraints on radon transport by water is its half-life and the radon outgassing either by exposure to air (as in the case of surface waters) or by elevated temperatures due to change in Ostwald coefficient. Another limiting factor for radon transport by water is the presence of liquid organic pollutants [Cothorn and Smith, 1987]. Radon is quite soluble in many organic liquids and therefore when these liquids are present in an aquifer, the radon concentration partitions between water and the liquids. This characteristic of radon partitioning between the various phases has been utilized in using radon as natural tracer for identifying and quantifying non-aqueous phase liquid (NAPL) in contaminant environments as has been described for example by Semprini *et al.* (2000), Schubert *et al.* (2005) and Schubert *et al.* (2007).

When radon leaves a saturated zone, it moves as a gas through dry permeable materials. This particularly occurs when groundwater is pumped out of an aquifer resulting in a lower water table. The fluctuation in the water table causes advective gas transport, which possibly augments radon transport through the unsaturated zone [DeWayne and Green, 2000].

At the soil/air interface, pressure driven flow transports soil gas into the air. For permeable soils, decreasing pressure draws radon-rich air from the ground. Also, at least experimentally, it has been found that increasing temperature increases the radon exhalation rate from soils [Cothorn and Smith, 1987]. This could possibly be attributed to the fact that increasing temperature decreases the amount of radon adsorption onto the soil materials [DeWayne and Green, 2000].

CHAPTER 3 RADON METROLOGY

There are several techniques and methods for measuring radon (^{222}Rn) in water. A review of some of these techniques is presented in CHAPTER 1, section 1.1. This chapter describes the set-ups and methodologies of four radon measurement techniques that are used in this study. These techniques are: alpha spectrometry using Liquid Scintillation Counting (LSC), alpha spectrometry using a DurrIDGE RAD7 radon monitor (subsection 3.2.2), gamma-ray spectrometry using a hyper-pure germanium (HPGe) detector, and *in-situ* γ -ray spectrometry using the MEDUSA system (section 3.3). The latter method makes use of simulated gamma-ray spectra obtained using the MCNPX simulation code described in section 3.4.

3.1 Introduction

Radon (^{222}Rn) can be detected by measuring the alpha, beta (and sometimes by its associated Cherenkov radiation) or gamma radiation, or a combination of these, emitted in the decay of radon or its daughters (^{218}Po , ^{214}Pb , ^{214}Bi , and ^{214}Po). The radon measurements are based on mainly three modes of measurement [Tykva and Sabol, 1995]:

- i. Instantaneous mode in which radon concentration is determined at a time when a sample (most commonly air or water) is taken or “grabbed”. This mode is therefore sometimes referred to as a grab-sampling mode,
- ii. Continuous mode in which radon concentrations are determined as a function of time, and
- iii. time integrating mode in which radon concentrations are time averaged over a period (generally a few days to a year)

Measurements can be made in the field or samples can be taken and measured in a more controlled environment such as laboratories where background contributions can be reduced by shielding the detector (e.g. by using lead) from ambient gamma radiation. Continuous and time integrating measurements are generally made *in-situ*, while instantaneous measurements can be made in the laboratory or *in-situ*.

This chapter describes the set-up and general measurement procedure of the four techniques for measuring radon in water outlined above. In section 3.2, the set-up and procedures for alpha spectrometry are described. This section is divided into two subsections: subsection 3.2.1 presents the set-up, measurement and calibration

procedures for two LSC systems. LSC measures radon by detecting and processing the scintillation light generated as a result of energy deposition by the alpha particles emitted from radon and its daughters ^{218}Po and ^{214}Po . Subsection 3.2.2 presents the set-up of the RAD7 and its measurement procedure. With the RAD7, radon in water is measured by stripping off the radon rich-air from the water sample, drying the air and counting alphas emitted from ^{218}Po and ^{214}Po using a planar silicon detector. The γ -ray spectrometry of radon in water using the HPGe detector and screw-top Marinelli beaker is discussed in subsection 3.3.1. The subsection describes the HPGe set-up, measurement and calibration procedure. The radon concentration is derived from six γ -ray lines emitted from the radon daughters ^{214}Pb and ^{214}Bi assuming secular equilibrium. Subsection 3.3.2 presents an introduction to *in-situ* γ -ray spectrometry using the MEDUSA technology. The γ -rays are detected by means of a CsI(Na) detector and the spectra are analysed using the full-spectrum analysis method (FSA), which is based on fitting the measured spectrum with a number of standard spectra and a measured background spectra. The calibration of the HPGe and the MEDUSA detectors involves some Monte Carlo simulations. The procedure of generating spectra using the MCNPX simulation code is described in section 3.4.

3.2 Alpha spectrometry

3.2.1 Alpha spectrometry using LSC

One of the oldest techniques of detecting ionizing radiation is *via* the scintillation light that is produced when radiation interacts with certain materials called 'scintillators'. In the scintillation process, the ionizing radiation excites the scintillator material molecules. These molecules partly de-excite by emitting visible light, which is collected by means of a light sensor such as a Photo-Multiplier Tube (PMT), and then converted into electrical pulses. The commonly used scintillators are inorganic (e.g. silver-activated zinc sulphide $\text{ZnS}(\text{Ag})$), and organic-based liquids (e.g. toluene) and plastics. The liquid scintillators are widely used for low-level radioactivity detection particularly when the radioactive material is dissolvable in the liquid scintillator cocktail (solvent and solute). When a radioactive material is dissolved in a liquid scintillator, nearly all the radiation emitted passes through a considerable portion of the scintillator and hence the counting efficiency could approach 100%. Unfortunately not all energy deposited in the liquid scintillation (LS) cocktail is converted into light: some of the de-

excitation modes do not emit light. This effect is termed quenching. Consequently, the counting efficiency decreases [Knoll, 2000]. The quenching is either chemical - causing energy losses in the transfer from solvent to solute; or color quenching, which is the attenuation of light photons in the colored solution. The overall effect of quenching is that it reduces the number of the photons produced in the LS cocktail.

This section presents the set-ups of two LSC systems used in the present work to measure radon in water; one LSC situated at the Nuclear Energy Corporation of South Africa (NECSA) and the second is situated at iThemba LABS-Gauteng (iTL-G). The sampling and measurement procedures are also described in this section.

3.2.1.1 LSC (NECSA) and LSC (iTL-G) set-ups

Figure 3-1 presents schematically the main components and their functions within an LS counter. Figure 3-1a is a flow chart illustrating a water sample mixed with a cocktail consisting of a scintillator and a solvent. The radiation emitted in the decay of radon and its progeny causes excitation of the scintillator molecules, which subsequently de-excite by emitting light. The emitted light is collected by photomultiplier tubes (PMTs) and converted into electrical pulses that are amplified by auxiliary electronics. The intensity of the scintillation light is linearly proportional to the deposited alpha energy [L'Annunziata, 1998].

Next, this signal is manipulated (sorted, digitized, and stored as counts) and displayed as a spectrum on a 4000-channel multi channel analyzer (MCA). Each channel corresponds to energy 0.5 keV. Thus, the 4000 channels are equivalent to energy range 0 to 2000 keV. In LS cocktails, the kinetic energy of an alpha particle is shifted by a factor of about 10, e.g. alpha energy of 6.0 MeV appears at ~ 600 keV. The shift in the alpha energy is due to the fact that α -particles produce pulses of longer duration in the LS cocktail compared to beta pulses. The consequence is that in the LSC, the alpha spectrum overlaps with high-energy beta spectrum. Hence, LSCs usually incorporate a pulse-shape discrimination mechanism to distinguish between pulses from alphas and of high-energy betas [Kobayashi, 1988].

One of the LSC systems that have been used for this study is a Packard TRI-CARB 3170 TR/SL model. Figure 3-1b shows a schematic diagram of the detection section of the TRI-LSC set-up. It shows the sample holder viewed by two PM tubes (PMT1 and PMT2) which detect the light pulses in coincidence and subsequently sum them. The pulses of the PMTs are fed into auxiliary electronics that incorporates Pulse Shape

Discriminator (PSD) electronics. The sample holder is surrounded by a bismuth germanate (BGO: $\text{Bi}_4\text{Ge}_3\text{O}_{12}$) guard detector. The PSD electronics distinguish between α , β and γ pulses while the BGO acts as anti-coincidence shield against pulses generated in the liquid scintillator due to γ -rays from the environmental, and muons from cosmic radiation [Kessler, 1989; Kobayashi, 1988].

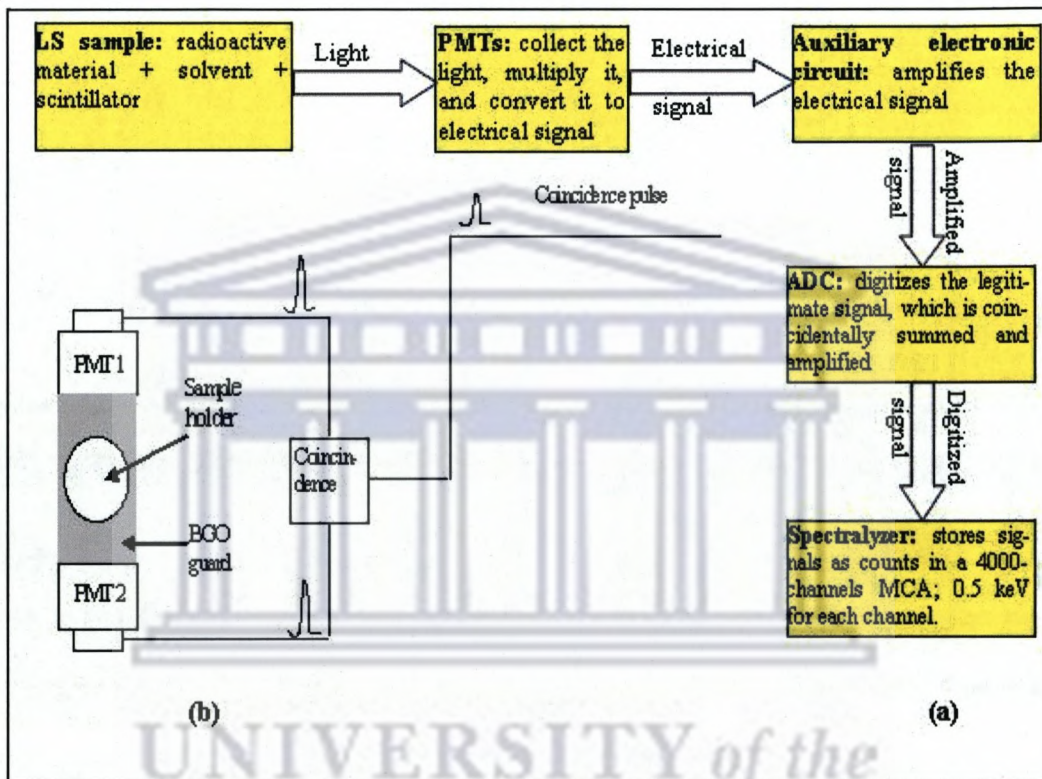


Figure 3-1: Illustration of LSC principle. (a) Flow chart summarizing the main components of a Liquid Scintillation counter, their respective functions and outputs. (b) Schematic diagram of a detection section of a Packard TRI-LSC system [Kobayashi, 1988].

A sketch of the internal detection part of type TR-LS system is shown in Figure 3-2. It depicts a BGO surrounding a sample in its holder and viewed by two PM tubes. Figure 3-2 also shows the various sources of background radiation, which the BGO reduces (<http://las.perkinelmer.com>).

Samples in this work were analysed by the LSC set-up of NECSA in Pretoria and iThemba LABS-Gauteng (iTL-G). The two set-ups differ in sample preparation and counting procedure. These procedures are described below.

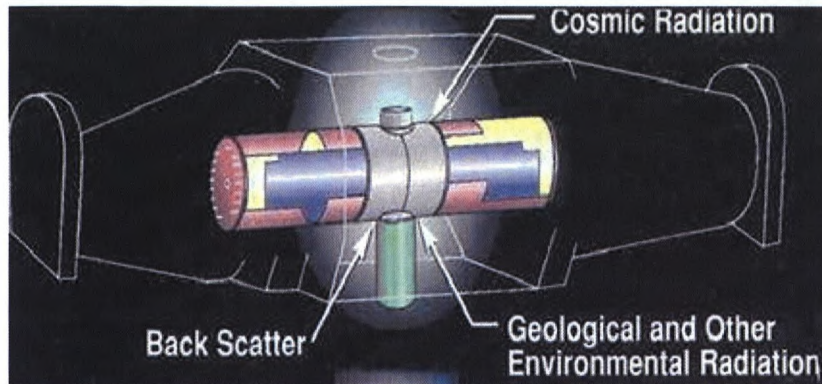


Figure 3-2: A drawing of the internal detection part of a TR-LSC system showing a sample in its holder surrounded by the BGO guard and viewed by the two PM tubes. (<http://las.perkinelmer.com>).

3.2.1.2 Sampling and measurement procedures

For the iTL-G LSC, water samples were collected in a one-litre bottle and then decanted into a two-litre bottle. Thirty millilitre of Ultima Gold LLT scintillation liquid was added to the water sample in the two-litre bottle and shaken vigorously for five minutes. Next the radon concentrated liquid (aliquot) is separated from water by means of density separation using funnels. Finally, 20 ml of the aliquot is extracted and placed into the LSC vial. For this study, all water samples were prepared in the field in counting vials and transported to the laboratory. Efforts were made to minimize radon losses during sampling, handling and sample transport.

At the iTL-G, the vials are loaded into a cassette and the cassette is in turn loaded into the LSC instrument and counted. At the time of current study, counting efficiency of this LSC was not determined and radon concentration was obtained in counts per minute (CPM).

The sample CPM is the net count rate i.e. corrected for background. The background measurements are obtained by measuring a radon-free water sample (e.g. old rain water) in the same sample geometry. The uncertainty in the count rate is estimated as:

$$\sigma = \sqrt{\frac{CPM_{sample} + CPM_{background}}{T}}$$

3-1

where T is the counting time (=50 minutes) for both sample and background.

Samples for counting with the NECSA LSC were prepared by syringing about 7 ml of water from the bulk sample through a 0.45 µm membrane filter (to remove solid particles) into a glass vial that already contains 13 ml of Ultima Gold LLT scintillation

liquid. The vial was capped and shaken thoroughly for mixing the liquid, stored in an upside down position and transported in this position to the laboratory at NECSA.

At the NECSA RadioAnalysis laboratory, samples were measured twice where each sample was counted for three hours. The first measurement took place after radioactive equilibrium has been established (3 hours). The second measurement was after three weeks (for ^{222}Rn to be in equilibrium with ^{226}Ra). The difference between the first and second measurement gives the count rate due to unsupported radon. The system was efficiency calibrated using a ^{241}Am alpha source. The efficiency values range between 79 and 82%. The LSC measures alpha (no distinction on energy) and therefore measures for each radon decay the alphas emitted by ^{222}Rn , ^{218}Po and ^{214}Po . Assuming secular equilibrium between radon and its progeny the count rate has to be divided by three.

Possible interferences from beta emitters are monitored using ^{90}Sr (beta emitter) standards and were found to be negligible for measurements of this study. In this study we use the minimum detection level (MDL) at the 95% confidence level [Kotze, 2008]. Typical MDL values were in the range 0.095 - 6.6 Bq/l. It must be pointed out that because the supported radon is subtracted, some of the gross alpha results obtained by this method are negative and/or less than the MDL values.

3.2.2 The RAD7 radon monitor

The DurrIDGE RAD7 technology also measures radon by alpha counting. In this section, the RAD7 set-up and the sampling and measurement procedures are briefly discussed.

3.2.2.1 The RAD7 set-up

The DurrIDGE RAD7 (www.durrIDGE.com) radon monitor used in this work is version 2.5f 991128, model 711 and serial # 01052. It is owned by the Department of Physics, University of the Western Cape (UWC), Bellville, South Africa. The system comprises three main units shown in Figure 3-3 that can be described as follows:

1. The RAD7 unit, which contains a microcomputer, a built-in air pump (1l/min flow rate), a measurement chamber (0.7l hemisphere) coated on the inside with an electrical conductor and in its centre a planar silicon alpha detector is situated;
2. Radon-in-water accessory (RAD7 RAD-H₂O), which consists of glass vials of volumes 40 ml or 250 ml for water sample measurement; desiccant (a substance of high affinity for water) columns; an aerator assembly (consisting of check

valve, stainless steel aerator, Teflon coupler, special vial cap, Teflon spacer and glass frit); tubing and filters. In this study only a 250 ml vial was used.

3. An infrared (IR) printer through which the RAD7 output results (such as the one shown in Figure 3-4c) is printed out.

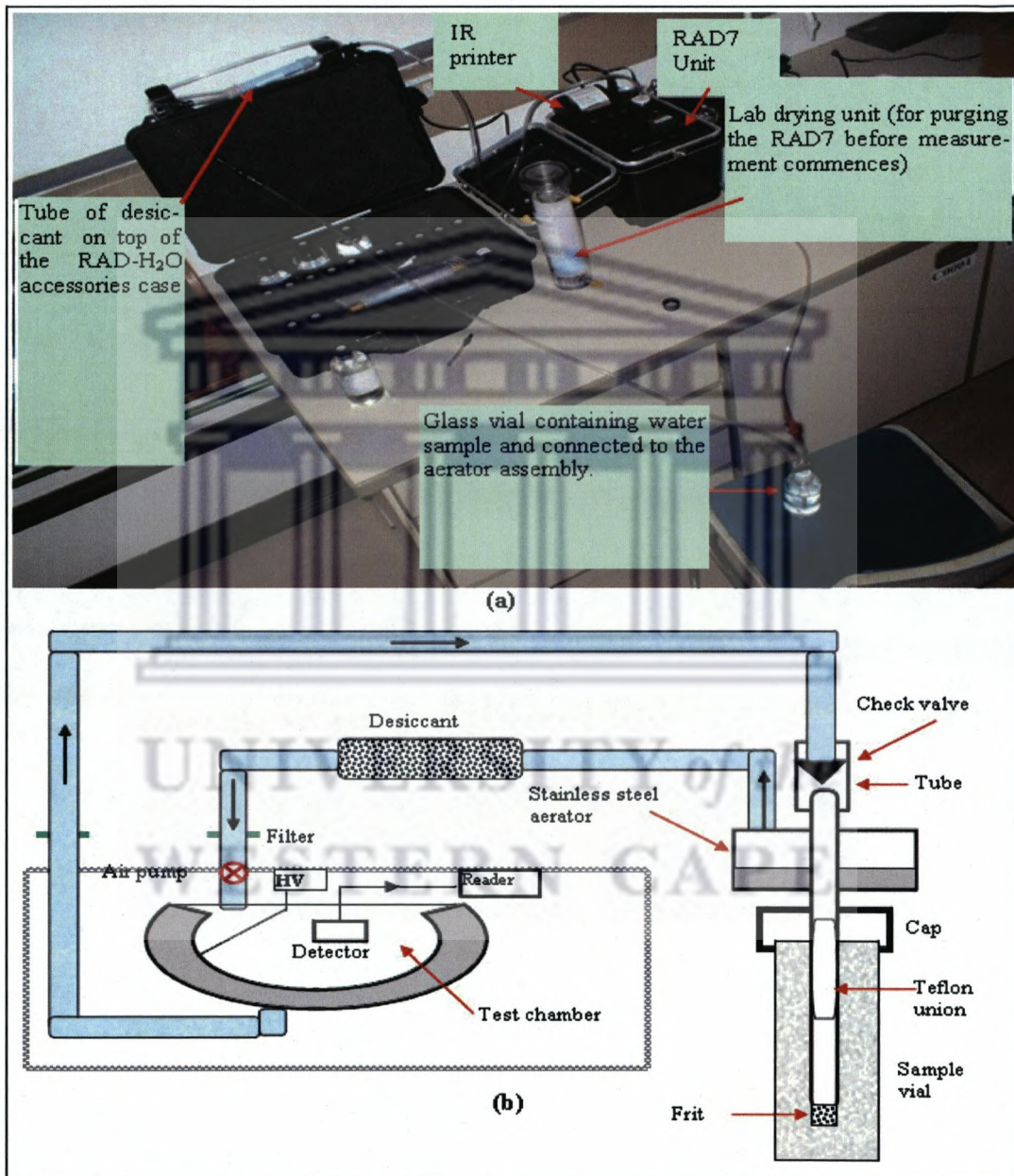


Figure 3-3: RAD7 set-up: (a) a photo of RAD7 RAD-H₂O showing the various units, namely a microcomputer, a built-in air pump, a test chamber and a planar silicon alpha detector. (b) Schematic illustration of the measurement sequences where some of the RAD7 unit constituents are depicted.

The RAD7 system measures the ²²²Rn concentration in water, in a grab sampling mode, by bubbling out radon-rich air, drying it, counting the α-particles emitted in the

decay of the ^{222}Rn progeny, ^{218}Po and ^{214}Po , and analyses of the α -spectra. The set-ups for all default functions are pre-programmed and controlled by the microcomputer. In particular, there is protocol Wat250 for radon in water measurements using a 250 ml vial. This protocol controls the pumping cycle and the counting cycle.

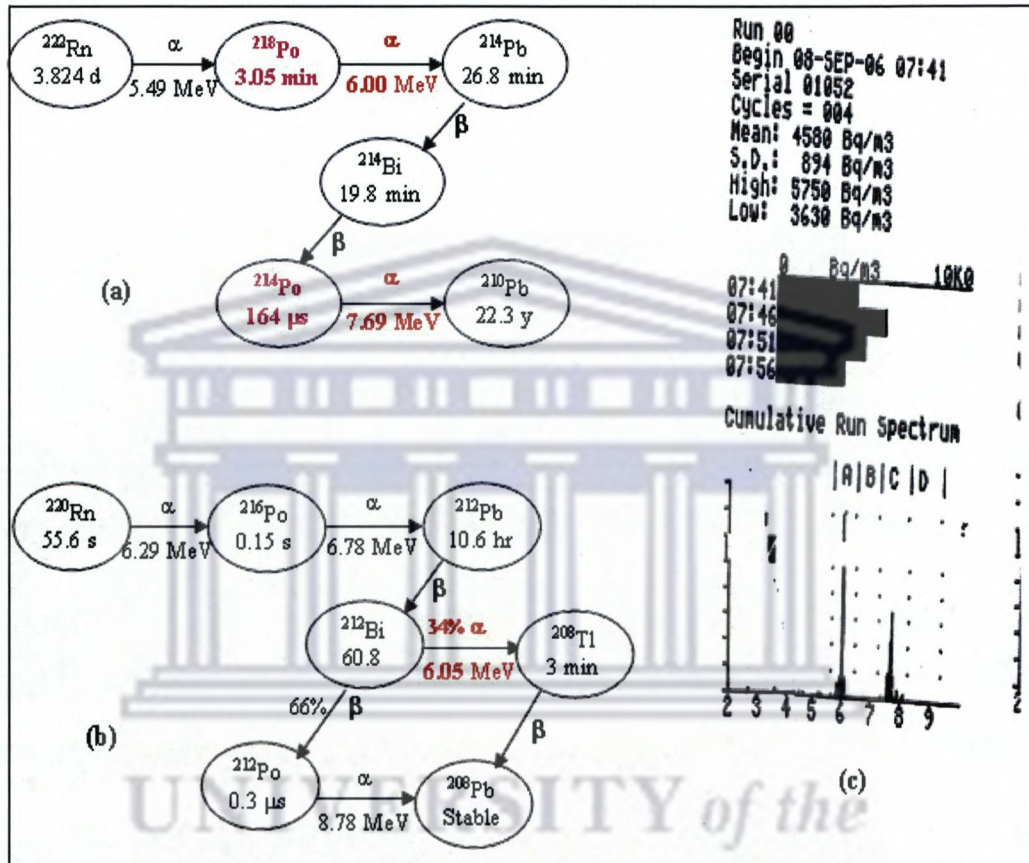


Figure 3-4: Schematic overview of (a) radon (^{222}Rn) and (b) Thoron (^{220}Rn) decay chains showing the decay mode (α and β), the half-lives (s: second; m: minute; h: hour; d: day; y: year) and the various α -particle energies in MeV; (c) Output summary provided by the RAD7 for a typical measurement showing information on the measurement time, the mean radon concentration and its standard deviation, a bar chart for the complete set of readings and a cumulative spectrum. In the cumulative spectrum, the main four windows are shown separated by dots.

3.2.2.2 Sampling and measurement procedure

For this RAD7 system, the water samples are placed in 250 ml glass vials and capped. Care was taken not to allow the water sample to be in contact with air. The RAD7 was first purged with dried and radon-free air to dry and clean the system. The purging continues until the relative humidity (RH) becomes less than 6% before starting the sample test.

The microcomputer automatically executes all the subsequent steps: starting by pumping air in a closed loop for five minutes causing radon to be released from the water sample by bubbling; the radon-rich air is then dried by passing through a Drierite desiccants and eventually accumulates in the test chamber. During these five minutes, equilibrium is established between the radon concentration in water and air, according to the partition coefficient³ (described in CHAPTER 2). After bubbling, the system waits for another five minutes. After these 10 minutes, ^{218}Po will almost reach equilibrium with ^{222}Rn . Next the RAD7 runs four counting cycles of five minutes each. Thus, the RAD7 completes the sample measurement in 30 minutes.

Inside the test chamber, the high-voltage circuit charges the conductor creating an electric field throughout the chamber. ^{222}Rn inside the chamber decays to ^{218}Po and ^{214}Po as positive ions. Before these ions are neutralized, they are attracted by the electric field and may be deposited onto the detector. At the detector, half of the α -particles emitted by the polonium hit the detector's active surface and produce a signal that is proportional to the α -particle energy. In this way, the RAD7 measures some of the α -particles emitted by radon and/or thoron daughters and it distinguishes between the various radionuclides by their α -particle energy.

The RAD7 then processes and stores these signals and accumulates their results in a spectrum with energy scale 0 to 10 MeV. This spectrum scale is divided into 200 channels of 0.05 MeV each. The 200 channels are grouped into 8 energy ranges (windows) of which four are major: A, B, C and D, see the bottom of Figure 3-4c. In Figure 3-4c, windows A and C are for radon and contain ^{218}Po ($E_{\alpha} = 6.00$ MeV) and ^{214}Po ($E_{\alpha} = 7.69$ MeV) peaks, respectively. Windows B and D are for thoron and contain ^{216}Po ($E_{\alpha} = 6.78$ MeV) and ^{212}Po ($E_{\alpha} = 8.78$ MeV) peaks, respectively. However, in the cases where "old" thoron is present inside the detector, i.e. when window D contains counts, window A will contain 34% of the counts in window D as illustrated in Figure 3-4b. This is because the RAD7 cannot discriminate between the ^{212}Bi ($E_{\alpha} = 6.05$ MeV) and the ^{218}Po ($E_{\alpha} = 6.00$ MeV).

It must be noted that the RAD7 is calibrated only if the prescribed settings are strictly followed. The final ^{222}Rn concentration in water is derived by averaging the results from the four five-minute cycles of the air removed from the sample. Figure 3-4c

³ The partition coefficient (PC) (described in CHAPTER 2) depends on the temperature, e.g. PC = 0.51, 0.25, and 0.11 at 0 °C, 20 °C and 100 °C, respectively.

indicates the printed output results of a typical measurement. The print-out is a test summary that shows the run number, date and time of the measurement, serial number of the instrument, the number of cycles in the test, the radon in water average value and its standard deviation, highest and lowest readings, a bar chart and a cumulative α -spectrum. When the RAD7 is operated under the prescribed procedures, the minimum detection limit is 0.4 Bq/l (1σ) ^{222}Rn .

Intermezzo 3.1: Estimation of the RAD7 alpha collection efficiency

Assuming a radon concentration in a 250 ml water sample to be 1 Bq/l, it is expected to yield on average 0.25 α -particles of ^{218}Po per second, assuming ^{218}Po is in equilibrium with ^{222}Rn . Hence, a 250 ml vial containing water with a radon concentration of n Bq/l is expected to yield $75 n \alpha$ particles of ^{218}Po per five minutes. The expected and calculated number of alpha particles corresponding to various radon concentrations in a number of samples is listed in Table 3-1. The table shows the radon concentration and its uncertainty, the corresponding sample code, date of measurement and the relative humidity (RH). Also presented in the table are the expected and calculated number of alphas, N^{exp} and N^{cal} , respectively; the estimated collection efficiency and its uncertainty.

The expected number of alphas was estimated from the uncertainty associated with the RAD7 radon concentration. For example, a sample of radon concentration having 25% uncertainty is expected to have originated from 16 ± 4 alpha particles. The collection efficiency equals the expected divided by the calculated α particles: $N^{\text{exp}}/N^{\text{cal}}$. From Table 3-1, one notices that the uncertainty increases with decreasing radon concentration and it is almost independent of relative humidity. Interestingly, the collection efficiency was almost constant over the entire range of radon concentrations between 1 and 66 Bq/l. The weighted average of the collection efficiency was determined to be $(1.85 \pm 0.07) \%$ associated with a reduced chi-square value of 0.2.

In conclusion, the large uncertainties associated with the radon concentration measured with the RAD7 are likely due to the small collection efficiency of the instrument.

Table 3-1: Details of samples measured with the RAD7. The table shows the radon concentration and its uncertainty and the corresponding sample code, date of measurement and the relative humidity (RH). Also presented in the table are the expected and calculated number of alphas (N^{exp} and N^{cal} , respectively); the estimated collection efficiency and its uncertainty.

Sample code	Date measured	conc. Bq/l	$\sigma_{\text{conc.}}$ Bq/l	$\sigma_{\text{conc.}}$ (%)	N^{exp}	N^{cal}	Coll. eff. (ϵ)	σ_{ϵ}	RH (%)
UWC4-10	22/3/07	1.06	1.16	109.4	0.8	80	0.011	0.011	19
UWC4-10	22/3/07	1.66	1.34	80.7	1.5	125	0.012	0.010	15
UWC4-12	23/3/07	1.66	1.34	80.7	1.5	125	0.012	0.010	16
UWC4-12	23/3/07	1.97	1.44	73.1	1.9	148	0.013	0.009	20
UWC4-3	20/3/07	2.11	1.47	69.7	2.1	158	0.013	0.009	12
UWC4-3	20/3/07	2.27	1.51	66.5	2.3	170	0.013	0.009	16
UWC-4-1	20/3/07	3.46	1.78	51.4	3.8	260	0.015	0.007	13
UWC-4-1	20/3/07	3.78	1.85	48.9	4.2	284	0.015	0.007	17
WRB #57	28/2/08	11.5	2.93	25.5	15.4	863	0.018	0.005	14
WRB #57	28/2/08	12.2	3.06	25.1	15.9	915	0.017	0.004	11
UWC-2	16/3/07	12.7	3.09	24.3	16.9	953	0.018	0.004	24
UWC-2	16/3/07	14.5	3.28	22.6	19.5	1088	0.018	0.004	19
UWC-10	17/3/07	16	3.44	21.5	21.6	1200	0.018	0.004	16
UWC-10	17/3/07	19.6	3.77	19.2	27.0	1470	0.018	0.004	19
WRB #11	28/2/08	20.5	3.87	18.9	28.1	1538	0.018	0.003	14
WRB #11	28/2/08	21.6	3.95	18.3	29.9	1620	0.018	0.003	11
UWC-3	16/3/07	21.9	3.97	18.1	30.4	1643	0.019	0.003	15
UWC-3	16/3/07	24.6	4.19	17.0	34.5	1845	0.019	0.003	20
UWC-12	16/3/07	24.6	4.19	17.0	34.5	1845	0.019	0.003	15
UWC-12	16/3/07	27.5	4.42	16.1	38.7	2063	0.019	0.003	19
WRB #05	28/2/08	30.3	4.61	15.2	43.2	2273	0.019	0.003	13
WRB #05	28/2/08	33	4.81	14.6	47.1	2475	0.019	0.003	17
WRB #26	26/2/08	45.9	5.61	12.2	66.9	3443	0.019	0.002	10
WRB #30	26/2/08	51.7	5.96	11.5	75.2	3878	0.019	0.002	20
WRB #20	26/2/08	66.2	6.71	10.1	97.3	4965	0.020	0.002	14

3.3 Gamma-ray spectrometry

3.3.1 Using a HPGe detector

The non-destructive gamma-ray technique using a HPGe detector involves the collection of a water sample in radon-tight containers. The method is based on detecting gamma radiation emitted in the decay of the radon short-lived daughters: ^{214}Pb and ^{214}Bi . The sample is measured after waiting for a period of at least three hours to allow for secular equilibrium (see section 2.2) between ^{222}Rn , ^{214}Pb and ^{214}Bi . Measurements are carried out at a laboratory under low-background conditions achieved by shielding the detector (e.g. by using lead) from ambient gamma radiation. Measurements are generally made over a period of few hours. Standard nuclear electronics are used to process pulses from the detector, *via* a multi-channel analyzer (MCA) system, into a gamma-ray spectrum. Some of the γ -ray photopeaks associated with the decay of ^{214}Pb and ^{214}Bi (see Table 2-1) are then analyzed to extract the activity concentration of radon

in the water sample. For this, the detector must be energy and efficiency calibrated. One of the main advantages of this HPGe non-destructive method is that it allows the measurement of other γ -ray emitting nuclides simultaneously. The following subsections describe the HPGe set-up at the iThemba LABS and its measurement and calibration procedures.

3.3.1.1 The HPGe set-up

The hyper-pure germanium (HPGe) detector, used for this study, is located at the Environmental Radioactivity Laboratory (ERL) of the iThemba LABS, South Africa. It is a Canberra *p*-type detector (model GC4520) with a 45 % relative efficiency and has a resolution of 2 keV FWHM (full-width-at-half-maximum) at the 1.33 MeV γ -line of ^{60}Co . Figure 3-5 illustrates the HPGe set-up. Figure 3-5a shows schematic cross-section of the detector inside the lead castle, connected to liquid nitrogen, and a Marinelli beaker fitted on top of the detector. The detector has a crystal diameter of 62.5 mm and a length of 59.0 mm and is encased in a 10 cm thick lead castle lined with 2.0 mm thick copper (Figure 3-5b) to reduce background (mainly X-rays emitted from the lead shielding and high energy γ -rays from building materials not fully absorbed in the shielding) in the sample spectra [Debertin and Helmer; 2001]. Figure 3-5c (left) is a photo showing the detector together with its built-in pre-amplifier kept at liquid nitrogen temperature and (right) schematic of the various units interfaced to the HPGe detector to measure and process the detector's signal. The cooling is crucial for germanium detectors to reduce the leakage current and hence improve the resolution [Knoll, 2000]. The HPGe detector at the ERL operates at a bias voltage of +3500 volts. The amplifier output is linked to a multi-channel analyzer (MCA) system. For this study, two types of MCA systems, with their software packages were used. The first was an OxfordWin (Oxford Instruments Inc.) MCA and software (version 3.80). The second was a Palmtop MCA from the Institute of Nuclear Research of the Hungarian Academy of Sciences (Atomki), 2005. The two software packages were used for both data acquisition and gamma-ray spectral analysis.

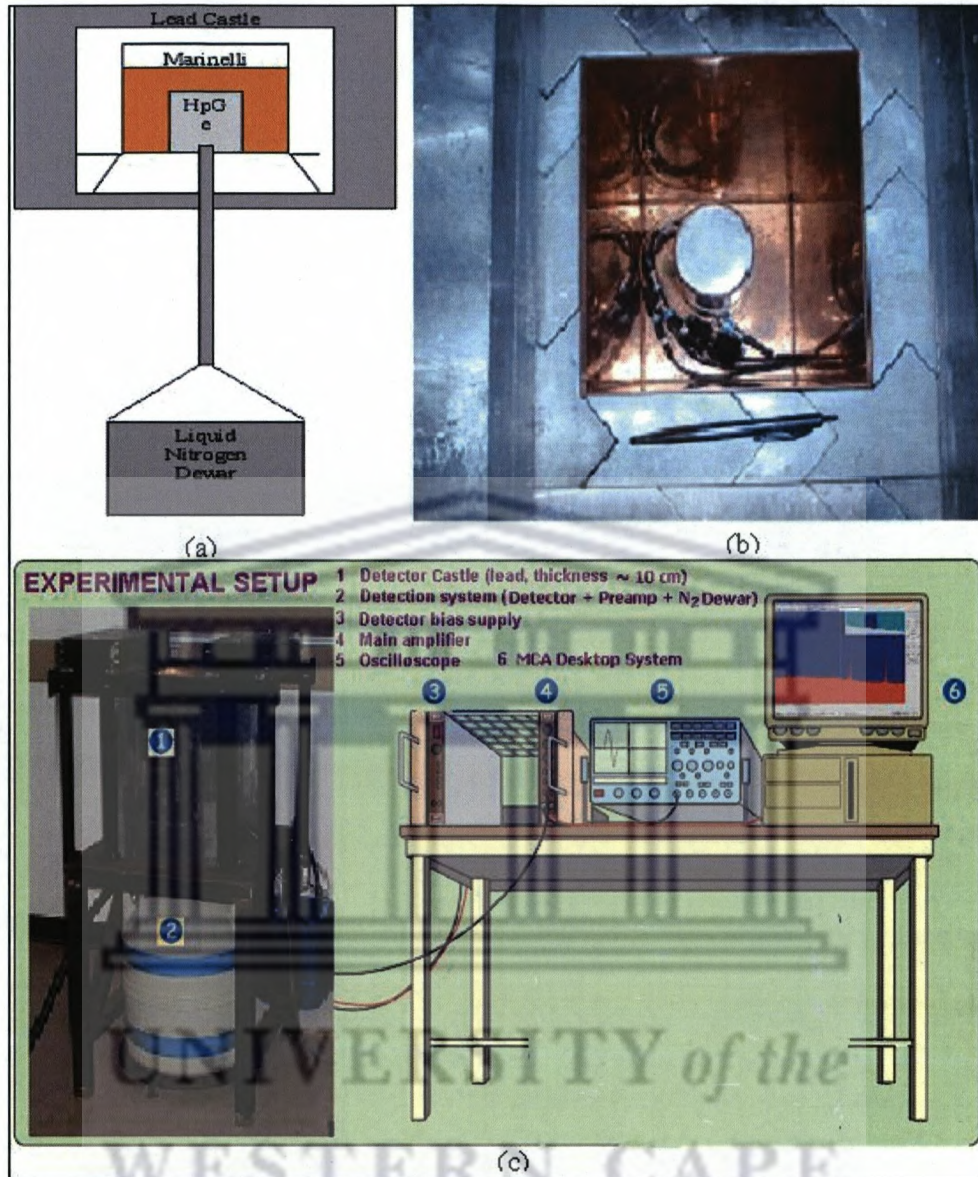


Figure 3-5: Illustration of the HPGe experimental set-up. (a) Schematic cross section of the detector inside the lead castle, connected to the liquid nitrogen and a Marinelli beaker fitted on top of the detector. (b) A top view photo of the HPGe crystal inside the lead castle lined with copper. (c) Overall photo of the HPGe set-up with a photo (left) of the lead castle housing the detector and supported on a mechanically rigid cryostat connected to a liquid nitrogen Dewar. On the right hand side of (c): schematic of the various units used with the HPGe detector to measure and process the detector's signal; photos adapted from [Damon, 2005].

3.3.1.2 Sampling and measurement procedures

Samples for the HPGe measurements are stored in radon tight containers e.g. glass jars and Marinelli beakers (see Figure 3-6) or collected directly in the measuring beakers; typically screw-top Marinelli beakers type AEC - Amersham, code NQB2205 with volume of $(1.3 \pm 1.0\%)$ liters. Since we sample clear water, there was no specific sample preparation applied. However, considerable caution was always observed to

avoid agitating water during sampling, sample transport or during sample measurements. To avoid radon being collected into the air space on top of the water sample, the container was always filled to the top. It is assumed that adsorption of radon daughters on beaker walls is negligible as discussed in subsection 3.3.1.5.

Some of the γ -lines of interest (e.g. 0.609 and 1.120 MeV) are reported to have been associated with systematic effects such as coincidence summing [Sanchez *et al.*, 1995; Garcia-Talavera *et al.*, 2001]. Thus far, there is no consensus on specific γ -lines to determine the radon concentration. In this study the weighted average of radon concentration was derived from the intensity of the six γ -lines emitted by radon daughters: 0.295, 0.352 MeV (from ^{214}Pb) and 0.609, 0.934, 1.120 and 1.765 MeV from ^{214}Bi .

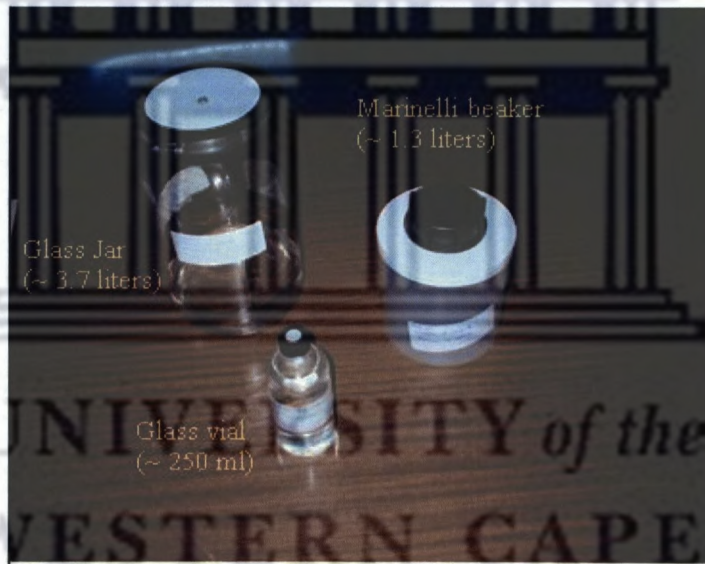


Figure 3-6: Radon-tight water sample containers; the glass jar is used when a bulk water sample is required to be split into sub-samples. The screw-top Marinelli beaker (type AEC - Amersham, code NQB2205) is used for the HPGe measurement, while glass vials are used for the RAD7 measurement (see subsection 3.2.2.2).

Spectra were analyzed using the OxfordWin and the Palmtop software which were discussed in subsection 3.3.1.1. With the OxfordWin, the regions of interest (ROIs) for both photopeak and continuum were set manually. Then the OxfordWin uses its built in algorithm to deduce the net counts in the photopeak area and its uncertainty. In the case of the Palmtop, only the photopeak ROIs were set manually and the software calculates the net counts in the photopeak area and its percentage uncertainty. The photopeak area

net counts and their uncertainties are then used in the extraction of radon concentration in the water sample.

3.3.1.3 The HPGe Calibration procedure

At the ERL, the HPGe energy calibration is conducted on a weekly basis using a reference ^{232}Th source: IAEA/RGTh-1 provided by the International Atomic Energy Agency (IAEA) sealed in a Marinelli beaker [Report: IAEA/RL/148, Vienna, 1987].

To quantify radionuclide concentration in an unknown sample, one needs to determine the counting efficiency at each of the photopeak energies for the geometry of measurement. The detector full-energy peak (FEP) efficiency as a function of energy, in the geometry of a screw-top Marinelli beaker filled to the top with water, was determined by means of a two-step approach similar to the one described by Croft and Hutchinson (1999).

The first step involves the calculation of the relative FEP efficiencies as: $\varepsilon_{rel}(E_i) = \frac{n(E_i)_{sample} - n(E_i)_{Bg}}{I_\gamma}$; where $n(E_i)$ is the count rate (cps) of each γ -ray line

(E_i) emitted with intensity I_γ in the radon decay. The relative efficiencies were obtained by measuring two types of water sample of unknown ^{222}Rn concentrations; one sample from a semi-cased borehole at iThemba LABS (iTTL) and the second one from a borehole located at Durbanville (Dv), both in the Western Cape Province of South Africa.

In the second step, the relative efficiencies are converted to an absolute scale using the absolute FEP efficiency at 1.46 MeV of ^{40}K measured with two Marinelli beakers filled with tap water (of insignificant radon concentration) and spiked with potassium chloride (KCl, impurity of 1.133% (see intermezzo 6.1)) powder of masses 50 g and 75 g. The tap water in a screw-top Marinelli beaker filled to the top was first measured for determining background, which was then used to correct for the ^{40}K net counts obtained from KCl mixtures measurement. The absolute FEP efficiency of the detector at the ^{40}K

energy line was calculated using the relation: $\varepsilon_{abs}(E) = \frac{n(^{40}\text{K})_{corr}}{I_\gamma * A}$; where $n(^{40}\text{K})_{corr}$ is

the ^{40}K count rate corrected for background. 'A' is the radioactivity of the dissolved KCl powder (50 g or 75 g) obtained from the calculation of the radioactivity of one kg of KCl that amounts to $(1.625 \pm 0.018) \times 10^4$ Bq/kg. This latter value was obtained by

utilizing the atomic fraction of ^{40}K in natural potassium ($1.17 \times 10^{-4} \pm 0.85\%$), Avogadro's number (6.02×10^{23} atoms/mol), and the half-life of ^{40}K ($4.027 \times 10^{16} \pm 0.63\%$) seconds [Firestone, 1998]. More details on the KCl activity calculation are presented in CHAPTER 6 (intermezzo 6.1).

The scaling factor (F_K), which converts relative efficiency to absolute efficiency, was then obtained using the relation:

$$F_K = \frac{\varepsilon_{abs}(^{40}\text{K})}{\varepsilon_{rel}(^{40}\text{K})}$$

3-2

The relative efficiency of K, $\varepsilon_{rel}(^{40}\text{K})$, was determined from fitting the relative efficiencies of the six γ -ray lines. The fit was achieved by means of least square minimization using the model: $\varepsilon(E) = a(E/E_0)^{-b}$, where $E_0 = 1$ keV, 0.295 MeV $\leq E \leq 1.765$ MeV, $a > 0$ and $0 < b < 1.0$ [Croft and Hutchinson, 1999].

The above procedure yields four sets of absolute FEP efficiencies presented in Table 3-2. A weighted average efficiency of each of the six γ -ray lines was calculated from the four measured efficiencies as presented in column eight of Table 3-2. The table also shows the associated uncertainties and reduced chi-square values. These FEP efficiencies have been validated using MCNPX simulations. The validation result is presented in subsection 3.3.1.4 and it shows good agreement between the efficiencies obtained by the KCl method and their counterparts obtained from simulations with the MCNPX code.

Similar to the relative efficiencies, the weighted average FEP efficiencies in Table 3-2 may be fitted with the model: $\varepsilon(E) = a(E/E_0)^{-b}$, where uncertainties associated with the interpolated efficiencies follow from the discussion in the intermezzo 2-2 (Eq. 2-9 and Eq. 2-10). The estimates of a and b and their uncertainties were determined using the statistical package Physica [Chuma, 1994] and found to be as follows: $a = 1.111 \pm 0.0002$ (Bq s) $^{-1}$, $b = 0.7345 \pm 0.0020$ and $\rho(a,b) = -0.836$.

Table 3-2: FEP efficiencies in the energy range 0.295 to 1.765 MeV for the iThemba LABS HPGe detector and a geometry of a screw-top Marinelli beaker filled to the top with water. The efficiencies were obtained by measuring 50 g and 75 g of KCl (dissolved in tap water of insignificant radon concentration) to scale relative efficiencies obtained by measuring radon-rich water (of unknown concentration) collected from boreholes located at iThemba LABS (iTL) and Durbanville (Dv). The last two columns presented the weighted average and the reduced chi-square, respectively. The weighted average quoted uncertainties are internal.

nuclide	${}^4E_\gamma$ (MeV)	I_γ (%)	FEP Efficiencies (%)					
			50 g (iTL)	50g (Dv)	75g (iTL)	75g (Dv)	wt. Av.	χ_R^2
${}^{214}\text{Pb}$	0.295	18.5 (3)	2.66(5)	2.73(5)	2.74(5)	2.75(9)	2.71(3)	0.5
${}^{214}\text{Pb}$	0.352	35.8 (5)	2.34(4)	2.40(4)	2.41(4)	2.42(10)	2.38(2)	0.6
${}^{214}\text{Bi}$	0.609	44.8(5)	1.57(3)	1.59(3)	1.61(3)	1.62(9)	1.592(16)	0.4
${}^{214}\text{Bi}$	0.934	3.03(5)	1.15(3)	1.16(3)	1.18(3)	1.18(9)	1.163(18)	0.2
${}^{214}\text{Bi}$	1.120	14.8(2)	1.01(3)	1.01(3)	1.03(3)	1.04(8)	1.018(18)	0.16
${}^{40}\text{K}$	1.460	10.7(2)	0.83(3)	0.83(3)	0.85(3)	0.85(8)	0.837(18)	0.12
${}^{214}\text{Bi}$	1.765	15.4(2)	0.72(3)	0.72(3)	0.74(3)	0.74(7)	0.729(18)	0.10

3.3.1.4 Simulated HPGe photopeak efficiencies

The detector FEP-efficiency calibration using the KCl method for the HPGe detector and a Marinelli beaker filled to the top was described in subsection 3.3.1.3 above. This procedure involves listed branching ratios (Firestone 1996) and the assumption that coincident summing is negligible; see subsection 3.3.1.5.

This section presents the FEP efficiencies of $E_\gamma = 0.295, 0.352, 0.609, 0.934, 1.120$ and 1.765 MeV, which are simulated for the geometry of the HPGe detector and screw-top Marinelli beaker filled to the top with water of radon concentration 1 Bq/l. This simulation was based on the Monte Carlo code MCNPX 2.6 b. The MCNPX simulations are described in detail in section 3.4. The parameters of the HPGe detector used for the simulations were optimized in a previous study [Damon, 2005]. The nuclides, γ -ray energy, γ -ray emission intensity (I_γ) and the simulated efficiencies are listed in Table 3-3. These simulated efficiencies were compared to the measured efficiencies (Table 3-2) and plotted in Figure 3-7. As the figure shows, the simulated efficiencies are in good agreement with their counterparts obtained by the KCl method.

⁴ The energies of the six γ -ray lines and their emission intensities (I_γ) were taken from the Table of Isotopes by Firestone (1998).

Table 3-3: FEP efficiencies in the energy range 0.295 to 1.765 MeV simulated using the MCNPX code for geometry of the iThemba LABS HPGe detector and a Marinelli beaker filled to the top with water containing radon of concentration 1 Bq/l.

Nuclide	E_γ (MeV)	Emission intensity (I_γ %)	Simulated eff. (%)
^{214}Pb	0.295	18.5 ± 0.3	2.7 ± 0.3
^{214}Pb	0.352	35.8 ± 0.5	2.36 ± 0.19
^{214}Bi	0.609	44.8 ± 0.5	1.55 ± 0.13
^{214}Bi	0.934	3.03 ± 0.05	1.2 ± 0.6
^{214}Bi	1.120	14.80 ± 0.20	0.99 ± 0.18
^{214}Bi	1.765	15.36 ± 0.20	0.71 ± 0.15

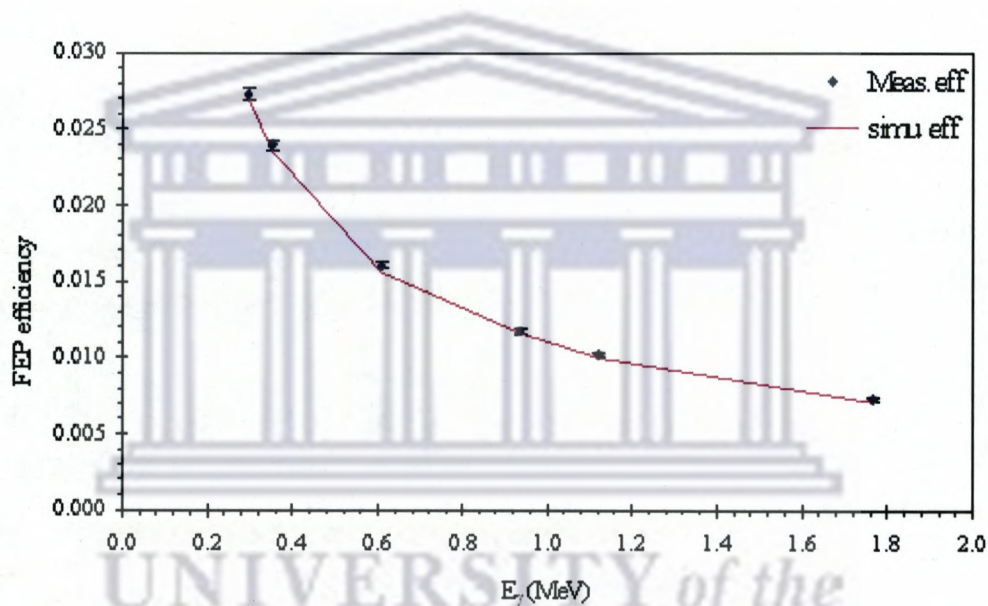


Figure 3-7: Measured (points) and MCNPX simulated (solid line) FEP γ -ray detection efficiencies for the iThemba LABS HPGe detector in the geometry of screw-top Marinelli beaker (filled to top) for the energy range 0.295 to 1.765 MeV (see the text for more details).

3.3.1.5 Investigation of coincidence summing

Some of the γ -lines that were used to derive the radon concentrations, for example 0.609 and 1.120 MeV from ^{214}Bi , are reported to be associated with systematic effects such as coincident summing-out [Garcia-Talavera *et al.*, 2001]. Coincident-summing effects for the geometry of our screw-top Marinelli beaker were investigated using the simulated efficiencies of the six γ -lines described in subsection 3.3.1.4. These simulated efficiencies were applied to 34 water samples, with various radon concentrations, and the radon concentration was derived from each of the six γ -lines separately. A weighted average of radon concentration from the four γ -lines 0.295, 0.352, 0.934 and 1.765

MeV, which are not expected to be affected significantly by coincident summing, was determined. The ratio between the concentration derived from each line and the weighted average was calculated. The results of applying the simulated efficiencies to the measurements of the 34 samples are presented in Table 3-4. The average ratio of radon concentrations derived from the 0.609 MeV γ -line indicates that the effect of coincident summing for this particular γ -ray is $6 \pm 3 \%$. In view of the uncertainties in the ratios for the other γ -rays, the overall effect on the weighted average is at maximum a few percent.

Hence, it is concluded that coincident summing does not play a significant role in the present analysis. The overall systematic uncertainty of a few percent in the absolute activity concentration is considerably smaller than the anticipated accuracy.

The HPGe radon measurements were checked further by checking the effective radon-decay constant. This involved extracting the effective ^{222}Rn decay constant, λ , for four water samples measured several times over four days using the HPGe detector. Depending on the ^{222}Rn concentration, the measurement time for these samples ranged between seven and ten hours. The decay of the ^{222}Rn concentrations was fitted with an exponential decay curve: $c * e^{-\lambda t}$. The effective ^{222}Rn decay constants for the four samples were found to be: $(2.51 \pm 0.05) \times 10^{-6} \text{ s}^{-1}$, $(2.11 \pm 0.02) \times 10^{-6} \text{ s}^{-1}$, $(2.08 \pm 0.11) \times 10^{-6} \text{ s}^{-1}$, and $(2.27 \pm 0.10) \times 10^{-6} \text{ s}^{-1}$, with a weighted average of $(2.16 \pm 0.08) \times 10^{-6} \text{ s}^{-1}$, which is consistent with the known λ -value of $2.10 \times 10^{-6} \text{ s}^{-1}$. This implies that there was no significant ^{222}Rn loss, due to radon leakage or adsorption effect, during the measurement process.

Table 3-4: Average ratio (1σ) of concentrations obtained by applying the simulated efficiencies to 34 measurements of groundwater samples. Each ratio was calculated from the radon concentration derived from one γ -line divided by the weighted average of concentrations derived from the four γ -lines 0.295, 0.352, 0.934 and 1.765 MeV, which are not significantly affected by coincident summing.

E_γ (MeV)	Mean of ratio
0.295	0.99 ± 0.03
0.352	0.99 ± 0.01
0.609	0.94 ± 0.03
0.934	1.02 ± 0.10
1.120	0.97 ± 0.06
1.765	1.07 ± 0.06

3.3.1.6 The HPGe and the RAD7 inter-comparison

The results of measurements on the HPGe and the RAD7 were compared for water samples with radon concentrations ranging from 1 to 45 Bq/l. The correlation between the two detectors is presented in Figure 3-8. The points are the data whereas the solid line is the weighted linear fit obtained by a least-squares minimization procedure. The slope and the intercept of the straight line were found to be 0.93 ± 0.04 and -0.03 ± 0.4 , respectively. The reduced chi-square of the fit was determined to be 1.8. This good correlation result also supports the finding that coincidence-summing effects are insignificant for the HPGe method.

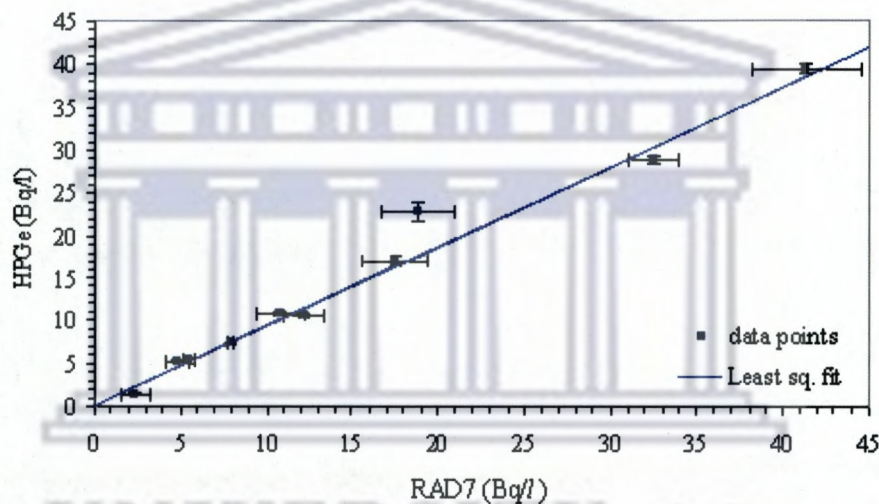


Figure 3-8: Correlation between the HPGe and the RAD7 for radon concentration in the range between 1.0 and 45.0 Bq/l. The solid line represents the weighted fit obtained by means of a least squares minimization procedure. The reduced chi-square of the fit is 1.8 and slope of the straight line is 0.93 ± 0.04 (Bq/l)/(Bq/l).

3.3.2 MEDUSA technology

3.3.2.1 Introduction

MEDUSA is an acronym for Multi-Element Detector for Underwater Sediment Activity. The detector system was developed by the Nuclear Geophysics Division of the Kernfysisch Versneller Instituut (KVI) at the University of Groningen in the Netherlands in collaboration with the British Geological Survey (BGS) [de Meijer *et al.*, 1997]. The MEDUSA technology was patented by the University of Groningen (RuG) in the Netherlands. The patent is currently held by MEDUSA Explorations BV, a RuG spin-off company.

The MEDUSA system generically comprises a gamma-ray detector, software tools (for measurement, analysis and display of results), a water-pressure sensor (determining water depth), and an acoustic device for measuring bottom coarseness. For spatial radioactivity measurements, the MEDUSA system can be interfaced with a positioning system device e.g. global position system (GPS).

The MEDUSA was first used for measuring the activity concentrations of natural radionuclides in underwater environments, in particular on sea- and river- beds [de Meijer *et al.*, 1997; de Meijer, 1998; Hendriks *et al.*, 2001; Venema *et al.*, 2001]. For these studies, the γ -ray detector used was bismuth germanate (BGO) scintillator crystal, which has the advantages of being available in large volume, having high density and high Z-value, and that it can be operated at ambient temperature.

The MEDUSA system at iThemba LABS has similar components as above except that the BGO γ -ray detector is replaced by a cesium iodide crystal, CsI(Na). This is because the CsI crystal has a more stable light output at variable temperatures compared to BGO detectors.

3.3.2.2 The MEDUSA set-up

Figure 3-9a shows a photo and a flow-chart diagram of the iThemba LABS MEDUSA detector system illustrating its main components and their interlinkage. These components are:

1. The detector assembly unit in its aluminium/stainless steel casing contains a gamma-ray detector (CsI(Na) crystal of 15 cm length and seven cm diameter), a photo-multiplier tube (PMT), a Cockcroft Walton high-voltage generator, spectroscopic amplifier, a temperature sensor (AD590), a pressure sensor, a microphone, and a telemetry board. The output of the amplifier is sent to the telemetry board where the detector signal, along with signals from a pressure sensor, temperature sensor and microphone, are digitized. The pressure sensor data are used for bathymetric measurements in underwater work while the microphone data are used to infer the coarseness of the sediment over which the detector moves. The detector unit is connected to an ALADIN interface box *via* an armored co-axial cable.
2. The ALADIN interface box that contains a data acquisition system. The box was supplied by the German company ANTARES Datensysteme GmbH and the

word ALADIN stands for ANTARES Log Acquisition and Data Interpretation System. For further details on the ALADIN refer to www.antares-geo.de.

- Software tools installed on a laptop for measurement and interpretation of radioactivity. The software programs are MEDUSA data logger (MDL), MEDUSA data synchronizer (MDS) and MEDUSA post analysis (MPA). First spectra are acquired *via* MDL software; then spectra are synchronized using MDS (first step of analysis) and the last step of analysis is using MPA to interpret results in various forms (see Figure 3-9).

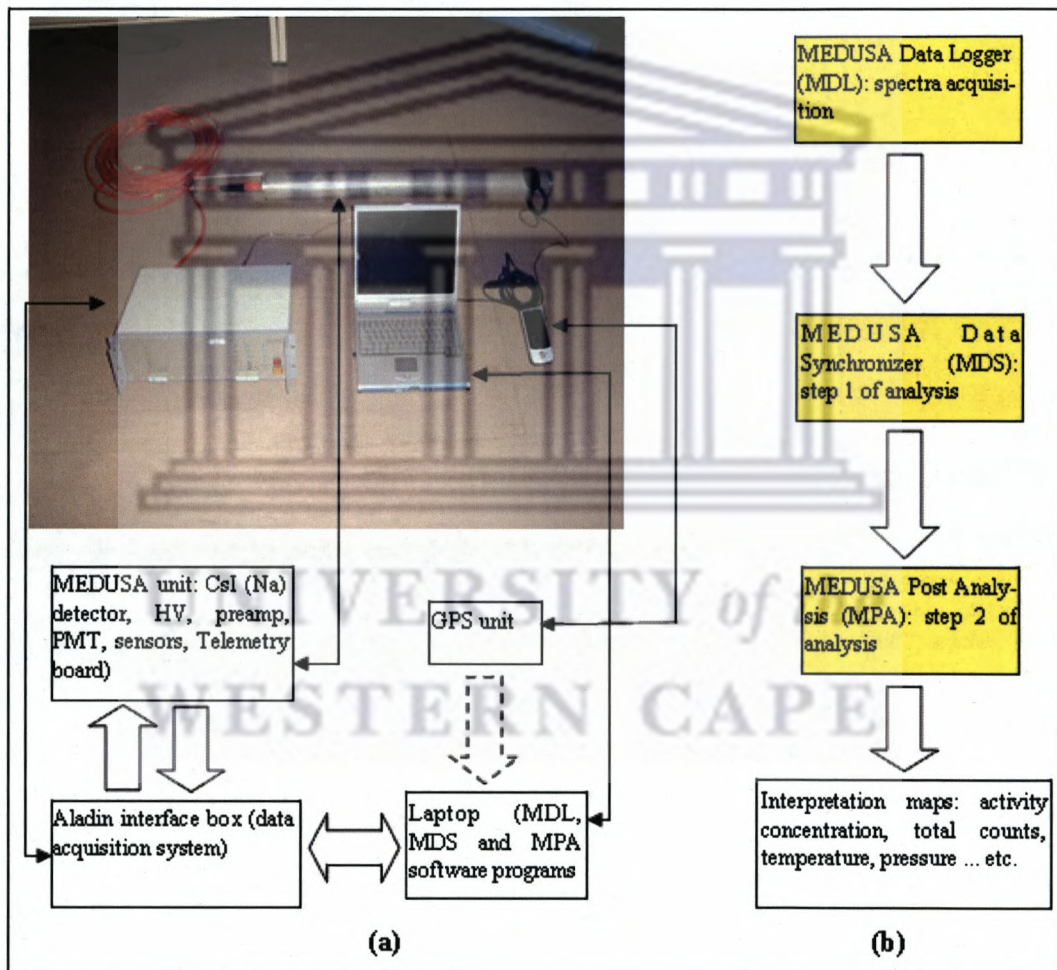


Figure 3-9: MEDUSA set-up: (a) top is a photo of the various components of the system. At the bottom is a flowchart diagram showing the interlinkage between the system's different units (block arrows). The arrows connect the components to their respective names. (b) MEDUSA data acquisition and analysis flowchart diagram.

3.3.2.3 The MEDUSA *in-situ* measurement and analysis procedures

In this study *in-situ* γ -ray spectrometry of radon in-water were carried out using the MEDUSA detector in-the-field in various geometries. The detector was deployed in the Vaal River near Orkney, North West province. The measurements were carried out to investigate the influence of streams entering the river on the radionuclide content in the river water. Measurement in this geometry involved suspending the MEDUSA detector overboard a boat at about one meter below the water surface, dragging the detector close to the riverbank and measuring on the riverbed. Figure 3-10 shows a photo of (a) the detector overboard a boat in the Vaal River and (b) the detector lying down half-covered with water (parallel with the riverbed) near the riverbank. For the suspended overboard-the-boat measurements - latitude, longitude, and altitude information- were recorded by a GPS signal receiver. The procedure used for these measurements will be described further in CHAPTER 5. The MEDUSA detector was also inserted in a water-filled container for measuring the radon concentration in the water. This geometry together with measurement and analysis methodology will be presented in CHAPTER 6.

Gamma-ray spectra were acquired through the MEDUSA data logger (MDL) software, which was installed on a laptop. The MDL also serves as an interface for the GPS data *via* the laptop. During the measurement, the γ -ray spectra were recorded in an MDL file every two seconds (i.e. as count per 2 s) while other information such as pressure, sound, temperature, latitude, longitude and altitude were recorded every second. The sum of the 2 s spectra in each measurement constitutes a log file.

The MEDUSA data analysis involves two processes (Figure 3-9b). The first process called synchronization is accomplished using the MDS software. The MDS creates a one-to-one correspondence between the measured spectrum and the associated auxiliary data (measured every second). The second process is post-analysis and it is achieved by using the MPA software. With the MPA software acquired spectra are analyzed using the full-spectrum analysis (FSA) method, which uses the entire spectrum. The FSA method applies a least-squares fitting procedure to obtain an optimum fit to the measured spectrum based on a number of standard spectra and a measured background spectrum (see intermezzo 3.2). The standard spectra are the response per unit time of a detector for a certain geometry to the γ -rays emitted by a certain radionuclide of concentration one Bq/l [de Meijer, 1998]. The background spectrum is usually

measured in the same geometry and location as the measurements such that no additional sources are present except for the environmental (terrestrial and cosmic) sources. This background is normally assumed to be constant in shape and magnitude over time.

In addition to the ^{238}U decay series, the ^{232}Th decay series and ^{40}K nuclide are also naturally present in soil and water with variable concentrations. Thus, the FSA procedure involves fitting the measured spectrum with three standard spectra, one for ^{40}K and one each for the γ -ray emitters in the ^{232}Th and ^{238}U decay series, plus the measured spectrum of background. For more details on the FSA procedure see intermezzo 3.2 below.

Intermezzo 3.2: FSA procedure

The FSA procedure applied in this study involves fitting the measured spectrum “S” with three standard spectra of ^{40}K (S_K), the γ -ray emitters in the ^{232}Th (S_{Th}) and ^{238}U (S_U) decay series, and a measured background (S_{bg}). As such the measured spectrum (photopeaks and continuum) represents the sum of the standard spectra each multiplied by the concentration of its respective nuclide plus the background spectrum. Hence, for each channel i :

$$S(i) = C_K S_K(i) + C_{Th} S_{Th}(i) + C_U S_U(i) + S_{bg}(i) \quad 3-3$$

C_K , C_{Th} , and C_U represent the activity concentration of ^{40}K , ^{232}Th and ^{238}U , respectively [de Meijer *et al.*, 1997]. The MPA programme deduces the optimum values of C_K , C_{Th} , and C_U by applying the least-squares procedure in which the reduced chi-square is given by [de Meijer *et al.*, 1997; Hendriks *et al.*, 2001]:

$$\chi_R^2 = \frac{1}{N_{\max} - N_{\min} - M} \sum_{i=N_{\min}}^{N_{\max}} \frac{[S(i) - C_K S_K(i) - C_{Th} S_{Th}(i) - C_U S_U(i) - S_{bg}(i)]^2}{\sigma^2 [S(i) - S_{bg}(i)]} \quad 3-4$$

N_{\min} to N_{\max} represents the reliable part of the spectrum where good fitting is obtainable and M is the number of standard spectra, $M = 3$ in this case. Unsuccessful gain-drift corrections or inappropriate peak shapes lead to poor fitting (high χ_R^2). The MEDUSA MPA programme has a feature of extra FSA parameters, A_0 , A_1 and A_2 which are called gain-drift parameters. These parameters could be adjusted manually to off-set the effect of the gain-drift on the fitting, i.e. optimizing χ_R^2 . However, a serious problem of

inappropriate spectrum-fit arose when the measured background is not constant, as discussed in CHAPTER 6.

For the present work the standard spectra were simulated using the Monte Carlo code MCNPX as described in section 3.4 below. Not all detector properties can be taken into account and, therefore, absolute concentration calibration factors are required. These calibration factors take into account some of the detector properties, such as light properties of the detector and the efficiency of the PMT, which are not included in the standard spectra simulated by MCNPX. The calibration factors were obtained by comparing measured ^{40}K activity concentrations to their calculated counterparts. The ^{40}K activity concentration was obtained from dissolving KCl salt in tap water. The MEDUSA calibration procedure for tank and drum geometries is discussed further in CHAPTER 6.

The background used for the analysis of the Vaal River *in-situ* MEDUSA data was measured in 2005 [Newman, 2008] by immersing the MEDUSA detector in water at the Theewaterskloof Dam near Villiersdorp, about 60 km from Cape Town. The background spectrum and more details on the Vaal River measurement procedure will be discussed in CHAPTER 5.

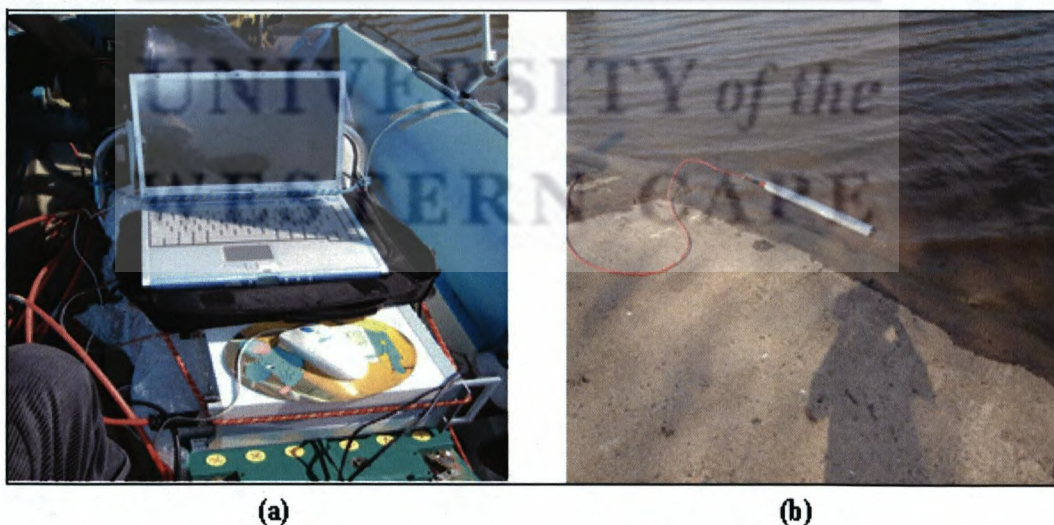


Figure 3-10: Two MEDUSA measuring geometries: (a) A photo of MEDUSA laptop and the armored cable on board a boat while the MEDUSA detector was suspended in the Vaal River (b) A photo of the MEDUSA detector lying down by the river bank where it was dragged manually across shallow water.

3.4 Generation and calibration of standard spectra

To obtain absolute radioactivity concentrations, calibrations of γ -ray spectrometers are often obtained from Monte Carlo simulations e.g. [Helmer *et al.*, 2004; Gutierrez-Villanueva *et al.*, 2008]. The simulations help minimize the number of experimental measurements needed for calibrating in the various geometries. In such simulations, the detector response is calculated for a geometry and matrix similar to the intended measurements. The simulation data are compared to results from measurements.

A general-purpose Monte Carlo N-Particle (MCNP) code is used for neutron, photon, and electron or coupled neutron/photon/electron transport calculations [Briesmeister, 2000]. MNCPIX was introduced in 1994 as an extension of MCNP to include more particles with nearly all energies. MCNP has proven to be a useful tool for the simulation of standard spectra for the flatbed geometry [Maučec *et al.*, 2001] and for the borehole geometry [Hendriks *et al.*, 2002].

The simulations of the present work involve two sets of standard spectra for the MEDUSA measurements. The first set (simulated at the KVI in the Netherlands) includes SSU-472 Sim K (for ^{40}K), SSU-472 Sim Th (for ^{232}Th series) and SSU-472 Sim U (for ^{238}U series). The spectra were simulated for a flat bed geometry (semi-infinite medium) using MNCPIX version 2.4.k run on Intel Pentium 4 processor 2.20 GHz [Newman, 2006]. This set of standard spectra was used for analyzing the Vaal River *in-situ* measurements described in CHAPTER 5. The second set of standard spectra includes spectra of ^{40}K , ^{232}Th series and ^{238}U series simulated for a drum/tank geometry [Maleka, 2007]. The code used to simulate this set was MNCPIX 2.6 b run on an AMD Athlon™ 64 bit processor (1.8 GHz). The settings consist of the MEDUSA CsI(Na) γ -ray detector placed at the centre of a 210 l steel drum filled with water and at a height of 90 cm or 100 cm from the bottom of a plastic tank. This second set of standard spectra is used for analyzing data from measurements described in CHAPTER 6.

In both sets, a total of 804 γ -ray energies [see also Hendriks *et al.*, 2002] associated with the Th and U decay series and ^{40}K together with their decay probabilities were incorporated in the simulation models. For each radionuclide, the relative statistical uncertainties for the major γ -ray lines were monitored not to exceed 10%.

The MNCPIX configuration described for the second set of standard spectra in the paragraph above was also used to simulate a standard spectrum of ^{238}U decay series for

the iTL-HPGe detector in the geometry of a screw-top Marinelli beaker filled to the top with water. Parameters of the iTL-HPGe detector used for the simulations were optimized in a previous study [Damon, 2005]. The simulated $^{238}\text{U}/\text{Rn}$ spectrum was used to validate the HPGe efficiency calibration as discussed in subsection 3.3.1.4.

Figure 3-11 shows an example of spectra simulated with the MCNPX code for the geometry of the MEDUSA detector inserted into a tank. The shape of standard spectra for similar geometries do not change much when changing the volume e.g. from 1000 l (tank) to 210 l (drum). However, the magnitude (vertical axis) may change with volume. The simulated spectrum for the HPGe detector for the measurement geometry of a screw-top Marinelli beaker is presented in Figure 3-12. It can be seen that the shape and magnitude of this later spectrum are different from those of Figure 3-11. The difference in shape is due to the difference in resolution of the two detectors; the MEDUSA CsI scintillation detector has poorer resolution (broad peaks). However, the HPGe detector has a lower γ -ray detection efficiency, partly, because of the smaller volume of the detector and the sample compared to those of the MEDUSA set up.

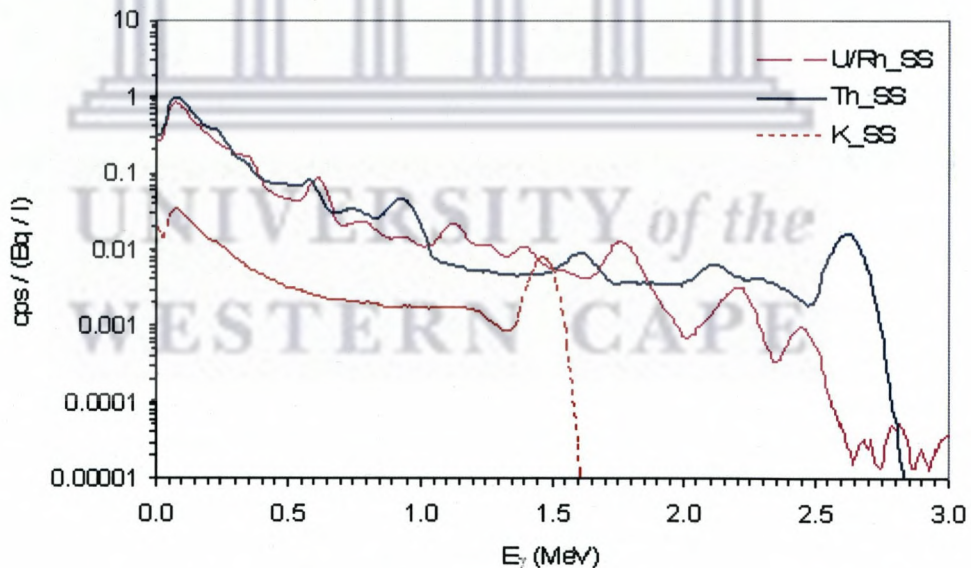


Figure 3-11: Simulated standard spectra of ^{40}K (dotted-line), ^{232}Th -series (solid line) and $^{238}\text{U}/\text{Rn}$ -series (dashed-line). The ordinate represents the MEDUSA detector response to one Bq/l per second of each radionuclide in the tank [Maleka, 2007].

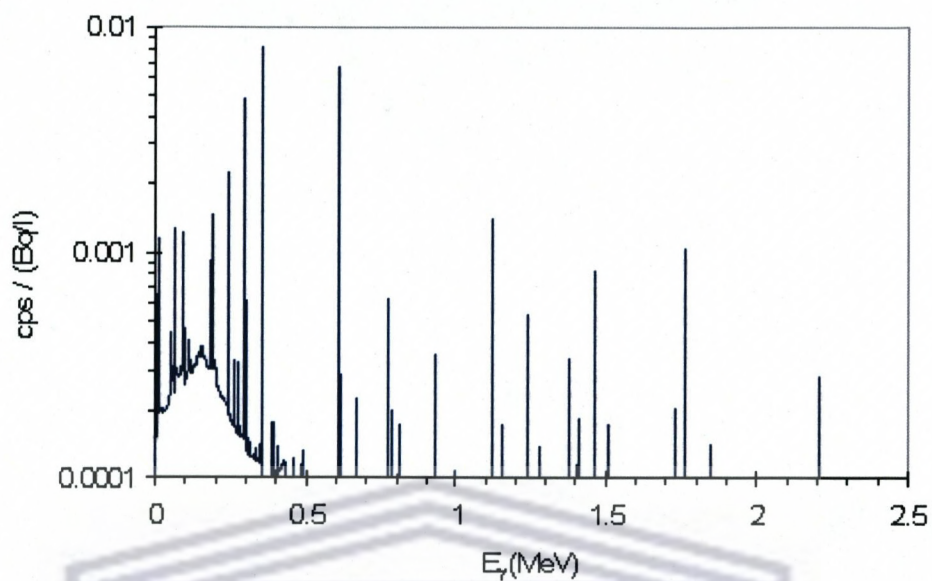


Figure 3-12: A HPGe spectrum of ^{238}U decay series including ^{222}Rn simulated with the MCNPX code in geometry of a screw-top Marinelli beaker filled to the top (volume ~ 1.3 l) with water of concentration 1 Bq/l. The assumption made was that all the nuclides are in secular equilibrium [Maleka, 2007].

UNIVERSITY of the
WESTERN CAPE

CHAPTER 4 RADON MEASUREMENT AT THE ITHEMBA LABS AQUIFER

In this chapter, measurement of radon in water by γ -ray spectrometry using a HPGe detector has been carried out to determine aquifer characteristics. The radon activity concentration is determined by taking the weighted average of the concentrations derived from γ -ray lines associated with ^{214}Pb and ^{214}Bi decay. The role of accurate radon data to representatively sample aquifers was also investigated by studying a semi-cased borehole. A simplified physical model describing the change of radon concentration with the pumping time reproduces the data and predicts the time for representative sampling of the aquifer.

After the introduction in section 4.1, the sampling and analyses procedures are presented in section 4.2. In section 4.3 the site and the iThemba LABS borehole will be described. The γ -ray spectrometry of radon in water using the HPGe detector is discussed in section 4.4. This includes the pumping-test measurements in subsection 4.4.2. Before the conclusion, the model description and the model-parameter determination are discussed in section 4.5.

4.1 Introduction

Radon (^{222}Rn) is a natural tracer for studying hydrological transport processes. It is transported without substantial adsorption in the matrix. As discussed in CHAPTER 1 radon-in-water measurements have been used, among others, to investigate aquifer characteristics and study the mixing between groundwater and surface water.

In a study of aquifer properties, the emphasis is generally on precision and reproducibility rather than accuracy of associated measurements. In view of the uncertainties in the geological and hydrological description of radon-genesis properties of aquifers, an accuracy of 25% (systematic uncertainties) for the method is more than sufficient.

This chapter presents the work carried out to optimize the measurement of radon in water *via* γ -ray spectrometry using a hyper-pure germanium (HPGe) detector as described in CHAPTER 3. The evolution of radon concentration with pumping time at the iThemba LABS aquifer was investigated by carrying out pumping-test measurements at a borehole situated on the iThemba LABS site. The measurements

involve determining total radon and supported radon concentrations. Based on the pumping-test results, a simplified physical model is proposed to reproduce the time evolution of radon concentrations. The model helps to predict the time for representative sampling of the semi-cased borehole provided that pump speed and the borehole dimensions are available. The model parameters were determined using the pumping-test data. The model is discussed in section 4.5.

4.2 Sampling and analyses procedures

Water from the iThemba LABS borehole (described in section 4.3) was pumped from depths of 8.0 m and 28.5 m. Ten pumping tests (PT), PT1 to PT10, were made. For PT1 to PT5, water was pumped using a single stage centrifugal pump, which has the specification: CALPEDA S.pA type CAM80; S/N 457163; L/min: 6.3/31.5. As shown in Figure 4-1a, the pump (SP1) was driven by an electrical motor (SP2) and lifts water through a two ended suction pole (SP3) placed at a depth of 8.0 m. Since the pump did not have speed control, the pump speed for each pump test (PT) was estimated by recording the time required to fill a bucket of 10 litre volume.

For PT6 to PT10 water was brought to the surface by a submersible pump. The specifications of the submersible pump (shown in Figure 4-1b) are: type 4BLOCK 2/13, flow rate up to 150 l/min, head up to 135 m, made by Flowline Technology (PTY) Ltd. The pump (shown in the figure as SMP1) was connected through adapters (SMP2) to a mechanical flow control (SMP3) and flow rate meter (Multi-jet dry-dial water meter manufactured by SENSUS Metering Systems) shown in the figure as SMP4. For PT6 to PT10 the submersible pump (SMP1) was placed vertically down the borehole with the pump bottom-end at a depth of 28.5 m. The pump speed for each PT was determined using the water volume pumped out over short periods. The water volume was taken from the flow-rate meter.

During the first two hours of each PT, samples were collected at short intervals (5 to 15 minutes) because the ^{222}Rn concentration increases rapidly at the start of pumping. The reason is that as pumping continues, more radon-rich groundwater flows from the aquifer into the pumping zone and mixes with the stagnant water. For the remainder of each pumping test samples were collected at convenient intervals (1-7 hours).

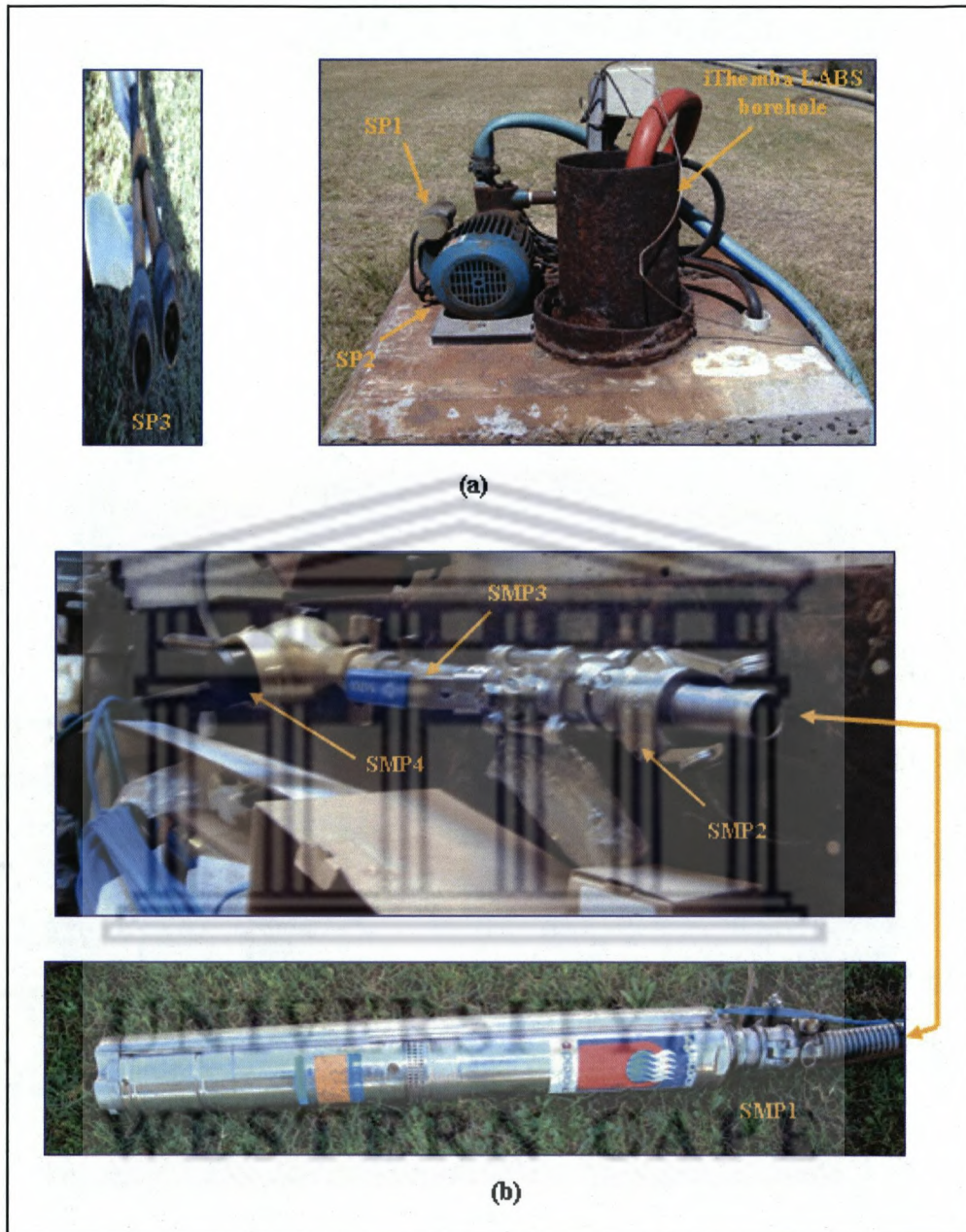


Figure 4-1: Photos of two water pumps beside iThemba LABS borehole showing (a) CALPEDA S.p.A [type CAM80, S/N 457163] single stage centrifugal pump (shown as SP1) driven by electrical motor (SP2) that lifts water through a 2 ended suction pole (SP3). (b) Submersible pump [type 4BLOCK 2/13 manufactured by Flowline Technology (PTY) Ltd] (shown as SMP1) connected through adapters (SMP2) to mechanical flow control (SMP3) and flow rate meter (Multi-jet dry-dial water meter manufactured by SENSUS Metering Systems) shown in the figure as SMP4.

To validate the method of γ -ray spectrometry using the HPGe, subsamples were also measured by α -spectrometry using the radon monitor, Durridge RAD7 (described in CHAPTER 3, subsection 3.2.2) used in grab-sampling mode. Water samples were collected in large volume containers (~ 3 l), split into sub-samples, and decanted into

Marinelli beakers (volume of about 1.3 l) and glass vials (volume of about 0.25 l) for the HPGe and the RAD7 measurements, respectively.

The RAD7 measures radon by counting alpha particles emitted from ^{218}Po and ^{214}Po in equilibrium with ^{222}Rn (see CHAPTER 3).

The γ -ray spectrometry of radon in water was carried out using the HPGe detector (described in CHAPTER 3, subsection 3.3.1) in a counting geometry of a screw-top Marinelli beaker (AEC - Amersham, code NQB2205, volume ~ 1.3 l) filled to the top. Measurements commenced after radioactive equilibrium between radon and its short-lived progeny had been established (3 hours). Each sample was counted for two hours. In addition some water samples from the borehole were sealed for a minimum of three weeks and supported radon (radon in-growth from ^{226}Ra present in the water) was measured using the HPGe detector. For the supported radon, the samples were counted for more than seven hours each.

Since the measured activity concentration is an integral average activity over the measurement time interval (t_0 , $t_0 + \Delta t$), we need to correct to obtain the activity concentration at the beginning of the measurement time interval ($A(t_0)$). The following relation can be derived:

$$A(t_0) = \frac{\lambda A_m \Delta t}{(1 - e^{-\lambda \Delta t})}$$

4-1

where $A(t_0)$ is the radon concentration at t_0 when the measurement commenced, A_m is the average radon concentration, λ is the radon-decay constant and Δt is the counting time.

Radon concentrations were derived from the intensity of six γ -lines emitted by radon progeny: $E_\gamma = 0.295$ and 0.352 MeV from ^{214}Pb , and $E_\gamma = 0.609$, 0.934 , 1.120 and 1.765 MeV from ^{214}Bi . The reported radon concentration is the weighted-average for the concentration of the individual γ -lines.

4.3 iThemba LABS borehole

4.3.1 Site description

The borehole is located at iThemba LABS and has the GPS coordinates: latitude 34.02523° S and longitude 18.7143° E. The iThemba LABS is about 30 km east of Cape Town, Western Cape, South Africa. The top part of Figure 4-2 shows a map of

South Africa with its various provinces and of the main cities including Cape Town. The bottom part of the figure shows the location of the iThemba LABS, where the borehole is situated and the current study was conducted. As can be seen from the figure, the iThemba LABS is situated off the N2 national road connecting Cape Town to Somerset West.

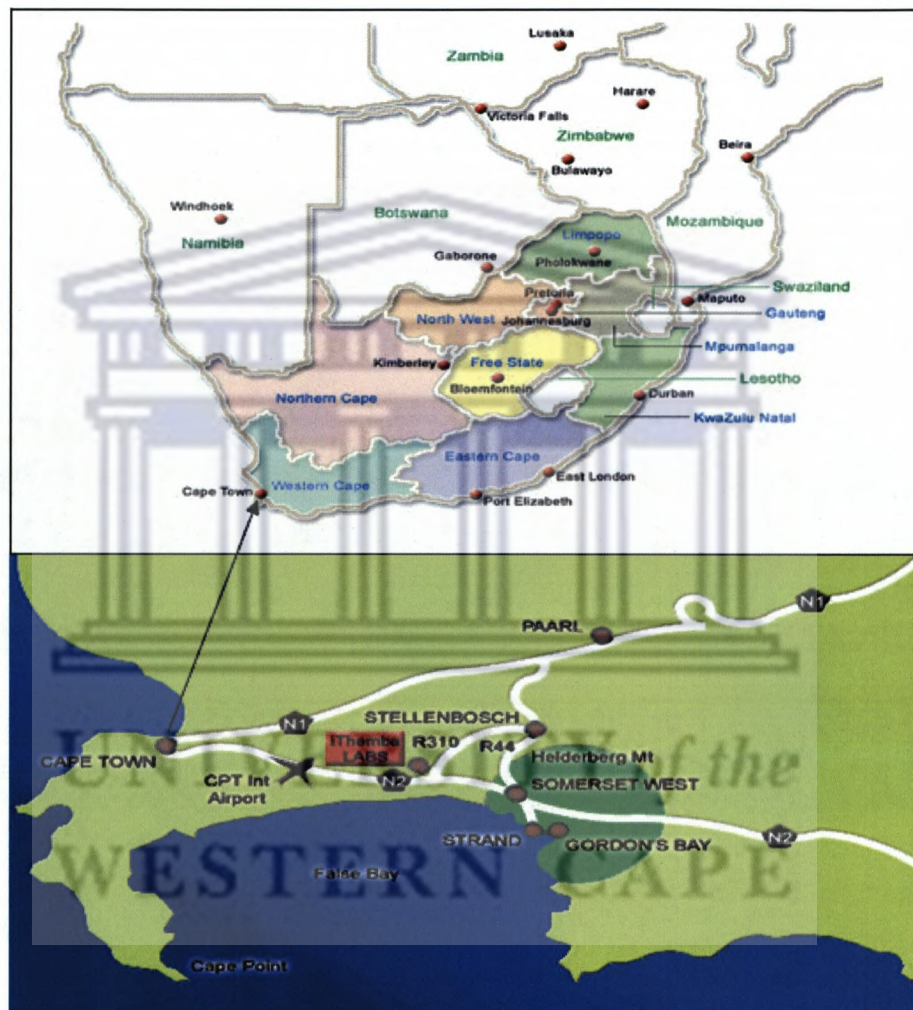


Figure 4-2: A map showing the location of iThemba LABS, where the borehole is situated, in Cape Town, South Africa. The top part is a map of South Africa and its various provinces where some main cities including Cape Town are shown [www.c2a.co.za]. At the bottom is an enlargement of the area around Cape Town showing the iThemba LABS located close to junction of the R310 and the N2 national road. The N2 connects Cape Town with Somerset West [www.tlabs.ac.za].

The iThemba LABS borehole taps the primary unconfined Cape Flats aquifer. This aquifer is fundamentally a coarse sand layer, of relatively low elevation above mean sea level, lying between the Cape Peninsula and the hills of Tygerberg and Stellenbosch.

The bedrock of the Cape Flats aquifer consists of the Cape Granite Suite and sediments belong to the Malmesbury Group [Adelana, 2006; Harris, 1999].

The borehole was drilled through a sand layer of about 30 m depth from the surface and then through a hard rock layer to a depth of about 30 m below the sand layer. The borehole logging documents were missing at the time this study was conducted. Therefore, the above borehole information was investigated as described in subsection 4.3.2 below.

4.3.2 Borehole casing

The depth of the iThemba LABS semi-cased borehole was measured to be about 60 m. In this section we investigated the casing of the borehole using a depth profile of electrical conductivity (EC) and temperature. Although not the optimal choice, the EC method has been used because other methods were not available at the time. Other instruments that can be used to check the borehole casing more reliably are a bubbler, a special instrument for determining the extent of a borehole casing, and a borehole camera whereby a depth profile photo of a borehole can be taken. The last two methods were not available at the time of this study.

The EC was measured on the 11th and 14th of August 2006. The borehole had not been pumped for more than three weeks and the water table was about 1.37 m below the surface. The EC meter was connected to a measuring tape. It reads the EC and temperature automatically while we recorded the depth from a visual reading of the measuring tape. For the top 30 m of the borehole, we took readings every 0.5 m while for the bottom 30 m, the readings were taken every 1 m. The EC of tap water was measured before and after taking the depth profile and found to be 0.4 mS/cm.

Results of EC and temperature versus depth are shown in Figure 4-3 below for the 11th August 2006 measurement. On the 14th August 2006 the data of 11th August 2006 was reproduced. As the figure shows, the EC changes with depth. In the beginning the EC steeply increases with increasing depth for about 12 m then it levels off up to a depth of 45 m. A further small increase in EC is observed at a depth of ~ 45 m.

From available information including the EC and temperature profiles, we infer that the borehole is constructed as follows: the borehole is cased for the first 12 m in a sandy layer; from 12 to 45 m below the surface (sandy layer) the borehole is screened i.e. a portion of the casing that has holes and allow water to move through; and at depth greater than 45 m the borehole is uncased and located in a fractured rock.

Based on this information, the borehole (with casing of inner diameter ~ 16 cm) is described as of volume ~ 1.2 m³, cased with steel up to a depth of 45 m and screened from 15 to 45 m depth, whereafter it is opened through hard rocks to a final depth of ~ 60 m).

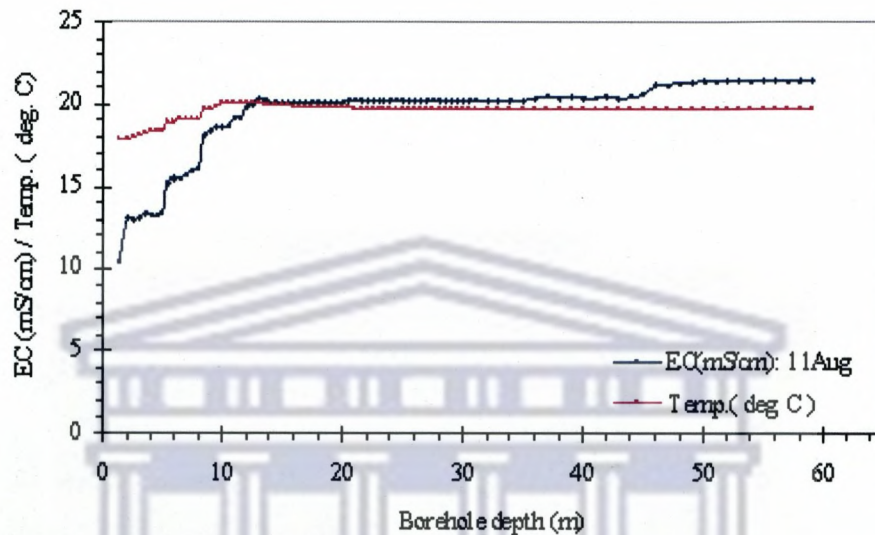


Figure 4-3: Depth profiles of electrical conductivity (EC) and temperature of the iThemba LABS borehole measured on 11 Aug. 2006.

4.4 Gamma ray spectrometry of ²²²Rn using a HPGe detector

4.4.1 Background measurement

For this study, a spectrum of municipal tap water was used for background correction. Figure 4-4 shows three partial spectra: for an empty Marinelli beaker, Marinelli beaker filled with tap water for background correction, and Marinelli beaker filled with a groundwater sample. From the figure, it is clear that the radon related γ -rays dominate the groundwater spectrum. Moreover, there is a no noticeable difference between the spectrum obtained with an empty Marinelli beaker and with one filled with tap water. This implies that the tap water does not contain any significant amount of radon. For this set-up, the minimum detectable activity (MDA) based on the 352 keV γ -line and a counting time of two hours was found to be 0.2 Bq/l (3σ). This value is one to two orders of magnitude lower than the measured values (see subsection 4.4.2.1).

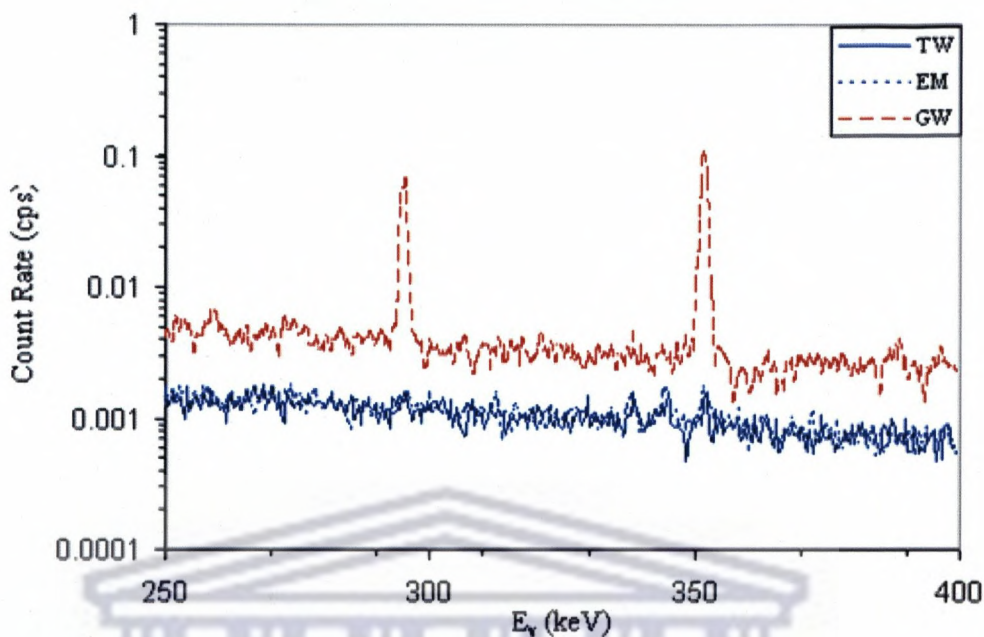


Figure 4-4: A small part (including two radon-related γ -ray peaks, 295 and 352 keV) of three spectra to illustrate that radon in the tap water used for background correction is insignificant. The three spectra were obtained by measuring an empty Marinelli beaker (EM), a beaker filled with tap water (TW) and a beaker filled with groundwater (GW) using the HPGe detector.

4.4.2 Pumping Tests

4.4.2.1 ^{222}Rn measurements

The total radon concentrations for the ten pumping tests together with elapsed pumping time are presented in Table 4-1 and Table 4-2. The water for PT1 to PT5 was brought to the surface using the CALPEDA pump (described in section 4.2) sucking water from a depth of 8.0 m inside the borehole. The results showed that each PT commences with low radon concentration (RnC) and then the RnC increases gradually up to steady higher value (plateau value) of about 30 Bq/l. The low concentrations at the beginning of each PT are most likely due to mixing between water in the cased part of the borehole with a low radon concentration, and groundwater with a certain radon concentration originating from the aquifer. In the cased part of the borehole, the concentration will be low because radon is only supplied by diffusion and disappears by radioactive decay. The RnC becomes steady after all mixed water has been pumped out and the aquifer water is pumped in. The first RnC is not the same for all PTs because the first sample was not a pure grab sample but collected after a few minutes of

pumping. Therefore, the first RnC depends very much on the depth, the pump speed, and the precise duration until the first sample is collected.

From Table 4-1 one notices that the plateau values are almost the same for all tests. The values listed for PT1, PT2 and PT3 are for samples that were measured immediately after collection without waiting for radon to reach equilibrium with ²¹⁴Pb and ²¹⁴Bi. When the last two samples of each of the three PTs were re-measured after secular equilibrium of radon with its short-lived daughters had been established (more than three hours), the radon concentrations were found to be 10 to 20% higher. The results of the repeated measurements are highlighted by the grey color at the end of their respective columns in Table 4-1.

Table 4-1: Date, elapsed pumping time, and total radon concentrations for pumping tests PT1 to PT5. The last two measurements of PT1, PT2 and PT3 were re-measured after radon had reached equilibrium (3h) with its short lived daughters. The ditto results are highlighted with grey color and presented at the end of their respective PTs columns.

PT1(*) ⁵ 12/12/2005		PT2(*) 1/26/2006		PT3(*) 2/16/2006		PT4 3/2/2006		PT5 4/19/2006	
time (h)	Rn (Bq/l)	time (h)	Rn (Bq/l)	time (h)	Rn (Bq/l)	time (h)	Rn (Bq/l)	time (h)	Rn (Bq/l)
0.03	10.4(4)	0.08	8.8(3)	0.08	5.5(2)	0.02	5.0(2)	0.01	2.3(5)** ⁶
1.03	20.3(1.1)	1.08	21.6(7)	2.08	24.9(4)	0.08	11.0(3)	0.10	18.3(4)
2.03	23.2(5)	2.08	21.8(13)	4.08	28.2(5)	0.25	22.4(5)	0.25	22.7(4)
3.03	23.4(6)	3.08	23.5(13)	6.08	27.9(5)	0.33	24.7(5)	0.52	24.5(6)
4.03	24.8(5)	4.08	26.0(13)	8.20	31.1(5)	0.58	26.5(6)	0.75	26.7(6)
5.03	26.5(6)	5.08	26.0(14)	10.17	29.3(5)	1.08	27.0(6)	0.95	26.4(7)
6.03	26.6(6)	6.08	27.6(1.2)	12.08	30.8(5)	1.58	27.4(6)	1.08	27.4(8)
7.03	27.8(6)	7.08	27.8(1.3)	14.08	31.2(5)	2.18	30.8(6)	1.25	28.4(7)
6.03- ditto	30.9(3) ⁷	6.08- ditto	32.6(6)	18.08	27.9(5)	2.67	30.3(6)	1.50	29.2(8)
7.03- ditto	30.3(3)	7.08- ditto	32.9(5)	20.08	27.8(5)	3.75	31.8(7)	1.75	29.7(8)
				22.08	29.9(5)	4.93	32.1(7)	2.00	30.2(9)
				24.08	29.4(5)	8.90	31.8(7)	2.33	31.5(7)
				22.08- ditto	32.0(5)	18.55	31.8(6)	2.67	32.3(8)
				24.08- ditto	33.7(5)	21.60	33.0(6)	3.00	31.7(9)
								3.33	32.2(7)
								10.00	33.2(9)
								20.13	33.7(7)
								24.20	33.8(9)

⁵ (*) means samples were measured after collection without waiting for ²²²Rn to reach equilibrium with its short-lived daughters.

⁶ The measurements marked with ** were excluded in the validation of a model, which will be described in section 4.5.

For PT6 to PT10, water was brought to the surface with the Flowline submersible pump (described in section 4.2) situated at a depth of 28.5 m in the borehole in the part with a screen casing. The results of these PTs are presented in Table 4-2. The radon concentration evolution follows a similar pattern as in Table 4-1 except that the initial concentrations are considerably higher. The higher initial concentration likely reflects the fact that with the screen casing, radon from the sand formation more easily diffuses to the water in the borehole. It can also be noted that, the RnC reached an even higher plateau after pumping time of 24 hours, probably showing a second plateau. The possibility of a second plateau will be discussed further in section 4.5.

Table 4-2: Date, elapsed pumping time and total radon concentrations for pumping tests PT6 to PT10. Measurements marked with ** were not used in the validation of a model that is discussed in section 4.5

PT6 6/28/2006		PT7 8/14/2006		PT8 11/15/2006		PT9 1/9/2007		PT10 3/9/2007	
time (h)	Rn (Bq/l)	time (h)	Rn (Bq/l)	time (h)	Rn (Bq/l)	time (h)	Rn (Bq/l)	time (h)	Rn (Bq/l)
0.03	26.6(4)**	0.02	23.6(6)	0.02	24.4(8)	0.02	25.7(4)**	0.02	22.8(4)**
0.27	24.4(4)**	0.10	25.2(6)	0.08	25.7(5)	0.07	24.4(5)	0.10	23.2(4)
0.52	24.1(4)	0.27	25.7(5)	0.18	25.0(7)	0.13	23.7(4)	0.18	22.8(5)
1.02	24.7(4)	0.52	26.7(5)	0.25	26.7(5)	0.18	24.3(4)	0.27	24.5(5)
1.53	27.1(5)	0.77	28.7(5)	0.42	28.8(4)	0.25	25.3(5)	0.43	26.8(5)
2.18	30.3(5)	1.10	30.9(7)	0.58	30.8(6)	0.42	26.3(6)	0.68	28.7(6)
2.85	30.3(5)	1.52	32.2(6)	0.83	32.5(6)	0.58	27.5(7)	0.93	29.6(7)
5.35	32.5(6)	1.93	34.2(1.2)	1.50	32.9(6)	0.83	29.5(7)	1.43	30.0(6)
11.40	33.2(5)	2.35	33.0(8)	8.25	34.6(8)	1.48	32.5(7)	2.43	33.1(8)
20.38	33.2(5)	2.68	32.9(8)	18.42	32.5(5)	3.83	33.5(8)	3.43	33.6(7)
24.05	32.9(5)	3.05	31.9(8)	22.83	34.1(6)	8.83	32.6(8)	5.98	34.9(9)
		3.35	32.2(9)			17.83	32.1(6)	7.98	33.7(7)
		9.78	33.8(6)			20.83	32.7(5)	9.98	35.4(9)
		24.12	32.7(5)			23.67	36.5(7)	11.02	34.8(7)
						25.83	33.2(6)	11.97	33.8(7)
						28.83	34.0(5)	13.82	34.1(9)
						45.13	36.0(6)	20.08	33.9(7)
						47.08	35.8(5)	20.98	34.6(9)
						52.87	34.0(5)	22.98	33.6(7)
						56.75	37.3(5)	27.07	33.2(7)
						67.13	36.9(7)	29.23	36.6(1.4)
						72.20	37.2(7)	31.17	37.2(9)
								35.00	38.0(1.1)
								39.00	38.4(9)
								42.95	35.4(9)
								45.65	35.3(9)
								47.15	35.8(1.0)
								51.23	37.5(1.2)
								52.48	38.0(1.2)
								54.20	35.1(7)
								58.07	36.3(9)
								66.60	35.4(8)
								67.98	37.2(7)
								70.82	38.6(1.1)

4.4.2.2 Supported radon

In subsection 4.4.2.1, the evolution of radon concentration with pumping time was investigated. In these investigations, the total radon (unsupported plus supported) was considered on the assumption that the supported radon was insignificant. The results of supported radon i.e. radon generated due to ^{226}Ra present in the water, in some of the borehole samples are presented in Table 4-3. One notices that the samples measured in June 2006 (referred to as J06 samples) have slightly lower radon concentration compared to other samples. The J06 samples were collected after flushing the borehole for a short time and have an average total radon concentration of about 17 Bq/l. This indicates that these samples may not be exclusively aquifer water. By contrast, the other samples were collected at the end of PT6 and PT8 after the borehole has been flushed for about 20 hours. One notices that the six concentrations are similar. From the concentrations presented in the table, the weighted average supported radon concentration is 0.82 ± 0.04 Bq/l, about two orders of magnitudes lower than the plateau radon concentrations. The reduced chi-square associated with a fit of the weighted average radon concentration to the concentrations given in Table 4-3 is 4.6. This slightly high chi-square value most likely reflects systematic uncertainties associated with J06 samples.

Table 4-3: Supported radon in groundwater samples from the iThemba LABS borehole. The average measuring time per sample was 10 hours.

Sample code	Date measured	Supported ^{222}Rn (Bq/l)
HPGe-1	19 June 2006	0.78(5)
HPGe-2	20 June 2006	0.68(5)
HPGe-3	21 June 2006	0.64(5)
PT6-9	25 July 2006	0.95(7)
PT6-10	25 July 2006	0.90(6)
PT6-11	26 July 2006	0.89(7)
PT8-10	12 Dec. 2006	0.99(6)
PT8-11	13 Dec. 2006	0.86(5)
PT8-12	14 Dec. 2006	0.91(6)
Weighted average: 0.82 ± 0.04 Bq/l		

4.5 Modelling: time evolution of radon concentration

4.5.1 Model description

Based on the borehole measurements presented in Table 4-1 and Table 4-2, a simplified physical model has been developed to describe the radon concentration as a function of pumping time and pumped volume.

Consider an aquifer with volume V_a , a constant radon concentration $C_a(t) = N_a/V_a = C_a$ and a sampling volume with volume V_0 , where $V_0 \ll V_a$. V_0 is a volume separated from the geological formation by a casing and is connected to V_a as schematically depicted in Figure 4-5b. N_a is the number of radon atoms in V_a . Sampling starts when the dynamic water table (the water level after pumping started as illustrated in Figure 4-5a) begins to stabilize. The radon concentration in V_0 when sampling started is C_0 . The pump sucks water from volume V_0 at speed v_p liters per second. Due to the pumping, water with concentration C_a replaces the water pumped out; see Figure 4-5b for a schematic presentation. In the derivation below, decay of radon is ignored since the refreshing process of the volume V_0 is much faster than the decay process.

The change in the number of radon atoms in the volume V_0 per time interval Δt is given as:

$$\frac{\Delta N}{\Delta t} = \frac{N_{in} - N_{out}}{\Delta t}, \quad 4-2$$

where $N_{in} = C_a * v_p * \Delta t$ and $N_{out} = C(t) * V_{out} = N(t) * v_p * \Delta t / V_0$.

This leads to the equation:

$$\frac{\Delta N}{\Delta t} = C_a v_p - N(t) v_p / V_0. \quad 4-3$$

Dividing by V_0 and allowing Δt to become infinitesimally small yields the equation for the change in radon concentration in V_0 :

$$\frac{dC}{dt} = (C_a - C(t)) \mu \quad 4-4$$

With $\mu = v_p/V_0$ being the refreshing constant. A solution for this equation is:

$$C(t) = (C_a - C_0)(1 - e^{-\mu t}) + C_0 \quad 4-5$$

From the procedure described above, the time at which sampling commences introduces an uncertainty which is reflected in the value of C_0 . Therefore, C_0 may differ from test to test.

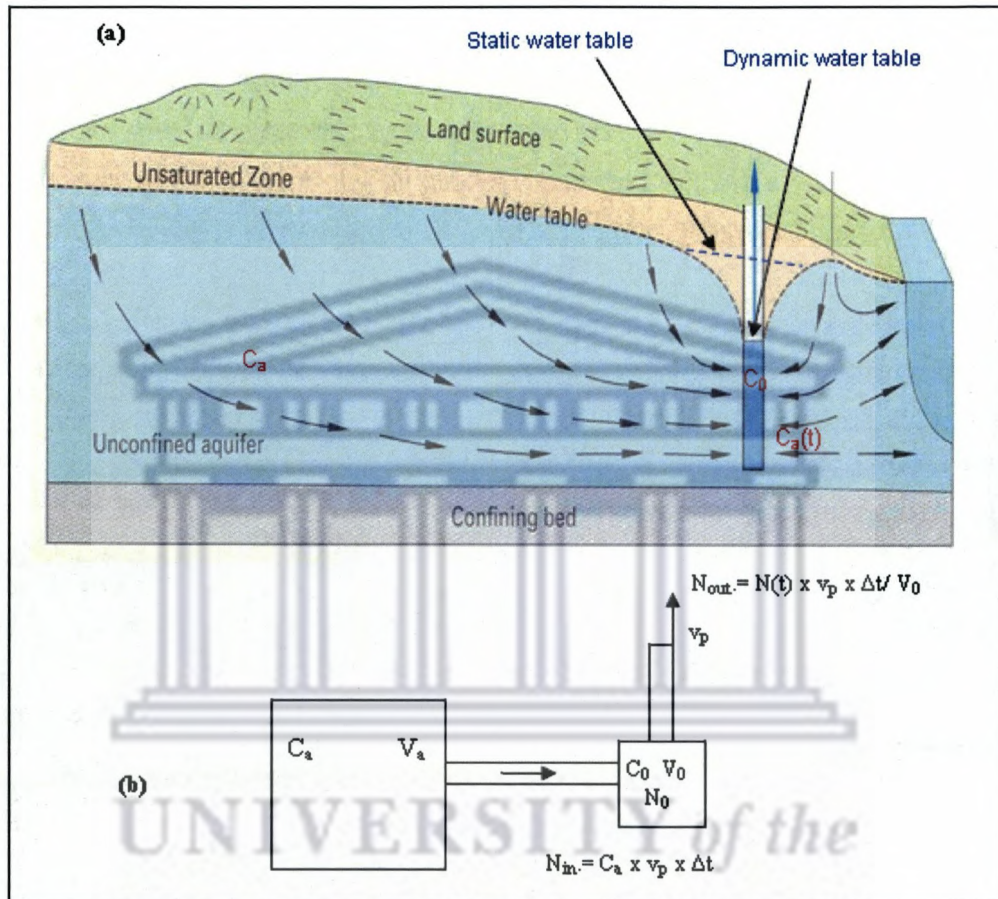


Figure 4-5: Schematic visualization of the physical model. (a) An illustration of a borehole tapping an unconfined aquifer showing the model initial assumptions explained in the text. The plot was adapted from Kelly (2006). (b) Schematic representation of the borehole system and the aquifer to elucidate the mathematical derivation of the model as described in the text.

4.5.2 Model applied to pumping tests

The model parameters for Eq. 4-5 are derived from the ten sets of pumping test data are presented in Table 4-1 and Table 4-2. Two examples are plotted in Figure 4-6 (PT5) and Figure 4-7 (PT10); they correspond to pumping depths of 8.0 m and 28.5 m, respectively. Figure 4-6 and Figure 4-7 demonstrate that the radon concentration initially increases with the water volume pumped out. After pumping out about 4 m³ of water, the radon concentration remains steady until about 100 m³ before the radon concentration increases to a higher plateau (Figure 4-7). This increase to a second

plateau may indicate that water from another reservoir starts to be sampled. This pattern of time evolution of radon concentrations during sampling is consistent with Zereshki (1983) and Freyer *et al.* (1997).

Table 4-4 shows the model (Eq. 4-5) parameters for the ten pumping tests. C_0 , the ^{222}Rn concentration in V_0 when the dynamic water table stabilizes, varies between the various PTs as sampling starts at different pumping times. The weighted average of μ yields a value of $\mu = (1.35 \pm 0.13) \times 10^{-2} \text{ min}^{-1}$ and a reduced chi-squared (χ_v^2) value of 2.4. Since there is an obvious change in the μ value by switching pumping speeds, the χ_v^2 value most likely reflects systematic uncertainties introduced by correlations between μ and C_0 . The weighted average value of C_a is $(33.4 \pm 0.3) \text{ Bq/l}$ with a χ_v^2 value of 3.0. This slightly high value of χ_v^2 most likely represents the fact that C_a is not constant, but changes over time (see Figure 4-7).

The time window between pumping out 4 and 20 m^3 of water appears to be the optimal time for representative sampling for this borehole. The measurement of radon concentration with the pumping time of an unknown aquifer may provide insight into the extent of the initial reservoir and the optimal flushing time before sampling.

It should be noted that, for this pumping model, it is assumed that there is no significant radon in-growth from dissolved ^{226}Ra (supported radon). As discussed in subsection 4.4.2, the weighted average supported radon from measurements of the borehole water was found to be only $0.82 \pm 0.04 \text{ Bq/l}$; almost two orders of magnitudes lower than the plateau radon concentrations.

Table 4-4: Details of pumping tests (PT) and the model parameters extracted by least squares regression. The weighted average of $\mu = (1.35 \pm 0.13) \times 10^{-2} \text{ min}^{-1}$ and of $C_a = (33.4 \pm 0.3) \text{ Bq/l}$ with χ_v^2 values of 3.0 and 2.4, respectively. Uncertainties reported with μ and C_a are external.

Pumping Test	Date conducted	Pumping depth (m)	Pump speed (l/min)	μ $\text{min}^{-1} \cdot 10^{-2}$	C_0 (Bq/l)	C_a (Bq/l)
PT1	12/12/2005	8	14.6 ± 0.4	1.4 ± 0.3	10.3 ± 1.2	29.5 ± 0.9
PT2	1/26/2006	8	14.5 ± 0.5	1.4 ± 0.4	8.5 ± 1.9	31.5 ± 1.9
PT3	2/16/2006	8	13.9 ± 0.8	1.3 ± 0.2	4.0 ± 1.5	32.4 ± 0.8
PT4	3/2/2006	8	15.0 ± 0.8	1.0 ± 0.2	22.3 ± 1.0	32.8 ± 1.2
PT5	4/19/2006	8	14.9 ± 1.2	1.41 ± 0.18	18.5 ± 0.9	33.3 ± 0.5
PT6	6/28/2006	28.5	12.6 ± 1.1	0.9 ± 0.2	20.7 ± 1.7	33.3 ± 0.6
PT7	8/14/2006	28.5	38.5 ± 1.0	2.0 ± 0.4	23.3 ± 0.8	33.2 ± 0.5
PT8	11/15/2006	28.5	59.1 ± 1.2	3.4 ± 0.7	23.4 ± 0.8	33.5 ± 0.5
PT9	1/9/2007	28.5	58.2 ± 1.8	2.2 ± 0.5	21.7 ± 1.2	33.5 ± 0.5
PT10	3/9/2007	28.5	59.8 ± 0.8	1.8 ± 0.3	21.4 ± 1.2	34.1 ± 0.3

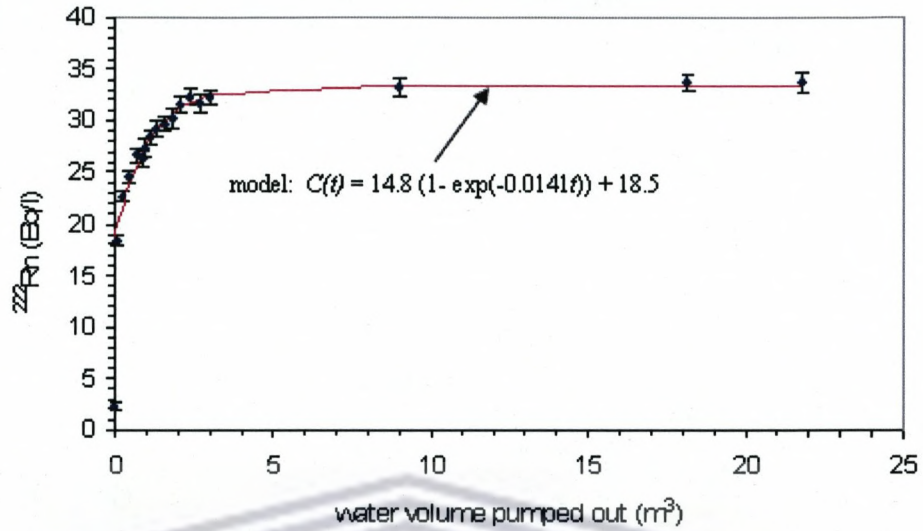


Figure 4-6: ^{222}Rn concentration for test PT5 (~24 hour duration) at a pumping rate of $0.015 \text{ m}^3/\text{min}$. The solid line is the model fit.

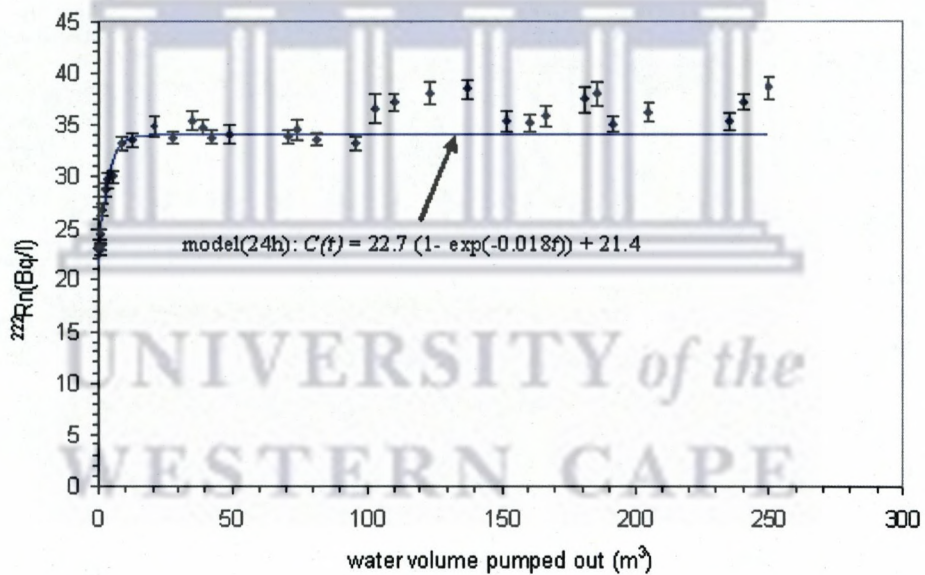


Figure 4-7: ^{222}Rn concentration for test PT10 (72 hour duration) at a pumping rate of $0.060 \text{ m}^3/\text{min}$. The model (solid line) parameters were extracted from the data for the first 24 hour of pumping (corresponding to $V_{out} = 85 \text{ m}^3$) and then extrapolated through the remaining data of the 72 hours.

4.6 Summary and conclusion

In this chapter, a model has been described that uses the time-evolution of radon concentration in borehole water to indicate the pumping time required for sampling an aquifer. Given some knowledge of the pump speed (v_p) and the borehole geometry (V_0), one can use the model to estimate the time for representative sampling from an aquifer

by measuring only C_0 and $C(t)$ at a slightly later time. The model, derived for this particular borehole, needs further testing at other locations and aquifers. The sampling strategy and analysis procedure seems to be robust for such tests.



UNIVERSITY *of the*
WESTERN CAPE

CHAPTER 5 RADON-IN-WATER MEASUREMENTS IN MINING AREAS

This chapter presents the results of radon measurements in water in two mining areas: West Rand Basin near Krugersdorp, and the Vaal River near Orkney. The measurements involve grab sample measurements analyzed by four techniques: α -spectrometry using a RAD7 radon monitor, α -spectrometry using LSC at NECSA, α -spectrometry using LSC at iThemba LABS-Gauteng and γ -ray spectrometry using the HPGe detector at iThemba LABS-Cape Town. In addition, an *in-situ* γ -ray spectrometry measurement of radon in the Vaal River water was carried out using the iThemba LABS MEDUSA system. The sampling and analyses procedures will be discussed in sections 5.3 and 5.4 while the study areas will be described in section 5.2. The results are discussed in section 5.5 and finally the chapter is concluded with a summary and discussion in section 5.6.

5.1 Introduction

In September 2006, the Water Research Commission (WRC) in collaboration with iThemba LABS and the CSIR in South Africa launched a multidisciplinary project (K5/1685) for studying environmental radioactivity and its applications. The project explores the use of radon (^{222}Rn) as a natural tracer in potentially polluted environments. In particular, the focus was on using radon to assist in gauging the impact of gold mining activities on fresh water aquifers in Gauteng and North West provinces.

As already mentioned in CHAPTER 1, radon in water has been measured in South Africa since the 1980s on an irregular basis by various research groups [Vogel *et al.*, 1999; Verhagen, 2003; Bean, 2006; Hobbs, 2008]. However, the full potential of radon as a hydrological tracer has yet to be exploited. This is important since the tracer has potential applications during dispersion studies, particularly in areas adjacent to gold mines, which are quite common in certain parts of South Africa. Measurements of radon in such mining areas may help in identifying mine-derived water mixing with a given water body.

This chapter presents some of the work done within the framework of the WRC radon project. The focus will be on the part of the measurements that were used to

investigate methods of measuring radon in water and aspects of the sampling procedures.

The field measurements of this work covers two areas- study area A: the West Rand Basin (WRB) area and study area B: about 10 km along the Vaal River near Orkney. The samples were measured with the RAD7 in the field and at laboratories of NECSA and iThemba LABS-Gauteng (iTTL-G), both using liquid scintillation counting (LSC) systems. In addition, some samples were collected and sealed in Marinelli beakers and transported by plane to iThemba LABS in Cape Town and measured by means of γ -ray spectrometry using a HPGe detector. These techniques and their general measurement procedures are described in detail in CHAPTER 3 and will be mentioned briefly in section 5.3 together with their specific application.

This chapter also includes *in-situ* γ -ray spectrometry measurements of radon in the water of the Vaal River using the MEDUSA technology described in CHAPTER 3 (subsection 3.3.2).

5.2 Description of sites

In this section the two study areas will be described. The study areas are- A: West Rand Basin near Krugersdorp and B: the Vaal River near Orkney.

5.2.1 Study area A: the West Rand Basin (WRB)

As shown in Figure 5-1, the West Rand Basin (WRB) study area is near the town of Krugersdorp (around Krugersdorp Game reserve) in the North West province, South Africa. The area lies between latitudes 26.06 – 26.13° South and longitudes 27.60 – 27.75° East. It is mainly underlain by two geological formations [Hobbs, 2008]: Witwatersrand Supergroup manifested in quartzite (Government Subgroup) and shale sediments; and the Transvaal Supergroup comprising sediments strata of dolomite, quartzite and shale. The dolomitic strata in the WRB area are also associated with an outlier of Malmani Subgroup dolomite represented by Black Reef Formation quartzite. Moreover, the area is characterized by fracture systems and faults such as the Rietfontein fault. Underground and shallower mining has taken place in the area. For example, the near-surface gold mining in the Black Reef Formation by the West Rand Consolidated Gold Mining Company.

In terms of hydrogeology, the area is characterized by springs, acid mine drainage (due to underground mine workings), streams such as the Riet Spruit and Tweelapie Spruit, and deep boreholes that tap the Karst dolomitic aquifer.

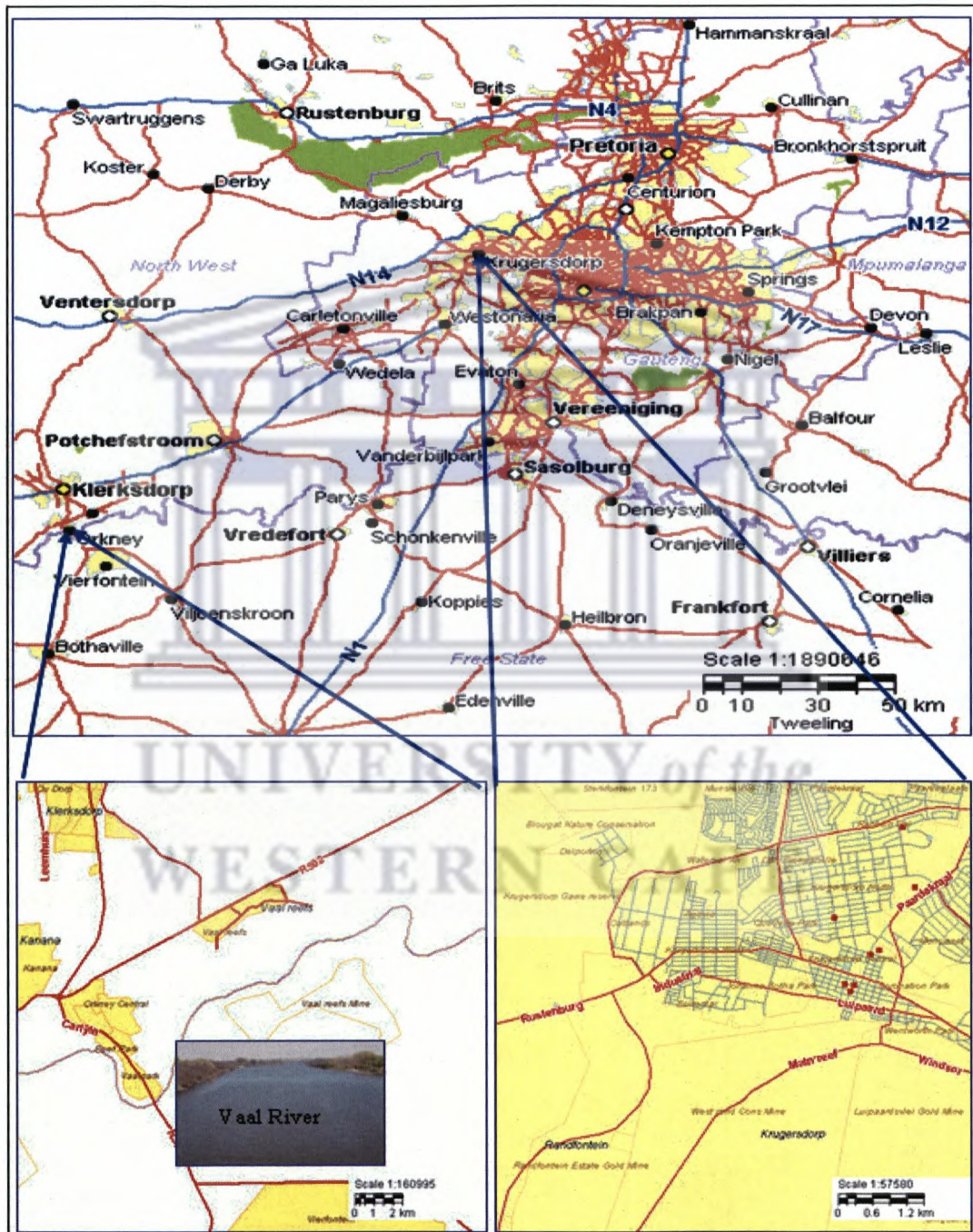


Figure 5-1: A map showing the two study areas. The top map shows the Krugersdorp and Orkney towns with Pretoria (Capital of South Africa) also shown on the Map. At the bottom, detailed maps of the study areas; bottom-right: Study area A where most of the samples were collected in the mining area around the Krugersdorp Game reserve; bottom-left: Study area B near Orkney with a photo of the Vaal River. Maps were adapted from <http://www.c2a.co.za/> cited 22 Nov. 2008.

5.2.2 Study area B: the Vaal River

The Vaal River, the largest tributary of the Orange River, is about 1120 km long and has its source at Drakensberg Mountains in Mpumalanga province, South Africa. The river passes on the border between Mpumalanga, Gauteng, North West, and Free State provinces and it forms one of the main sources of water for industrial and agriculture activities mainly in the Gauteng and the Free State provinces [www1]. Orkney is a mining town that lies on the banks of the Vaal River and it hosts the largest gold mine in South Africa: The Vaal Reef Gold Mine. The study area B (left hand side map at the bottom of Figure 5-1) covers about 10 km of the Vaal River near Orkney within the property of the Anglo-Gold Ashanti Mining Company. The area lies between latitudes 26.8927 – 27.0575° South and longitudes 26.6501 – 26.8346° East. The study area is part of the Middle Vaal Area, which has mixed geology with a large dolomitic intrusion underlain by igneous and metamorphic rocks. In terms of geohydrology, dolomitic aquifers occur in the area with fractured rock aquifers underlying most of the area [www2].

5.3 Sampling procedures

5.3.1 Grab samples

Several groundwater and surface water samples were collected for determining the concentration of ^{222}Rn and some of its progenitors. The sources of groundwater samples include deep boreholes, mine water due to underground mine workings known as mine acid drainage, artesian boreholes, springs, shallow boreholes and surface water. Due to varying circumstances and accessibility of the various sample sources, sampling was conducted according to a protocol based on: 1. get as close as possible to the target source, 2. taking representative samples and 3. minimize radon loss during sampling. To follow such a protocol, almost each source was sampled in a unique way. The details of the sampling are presented in Table 5-1. The table summarizes the sample source code, its description; the GPS coordinates of the sampling position, and the sampling procedures.

Several difficulties were experienced during the sampling. In the mine-water sources, difficulties were experienced at station # 22, 23 and 59. The problems were mainly the inaccessibility of the sample sources to collect all subsamples simultaneously. In these positions we were also not sure whether we were close enough

or far from the groundwater issue source. For spring samples we experienced time delay (about 2 minutes) between subsamples.

Table 5-1: Details of grab samples collected from mining areas. The table presents the sample source code, source given name (N/A means not applicable), description of source and area code, GPS coordinates of sampling position and sampling procedure.

Sample source code	Given name	Description and area code (A or B)	GPS coordinates (°)		Sampling Procedure
			Latitude (S)	Longitude (E)	
# 03	J. van Niekerk borehole	Deep borehole in a farm (A)	26.0898	27.6940	Flushed, then containers filled directly from hose pipe
# 05	A. Crawford borehole	Borehole in a farm (A)	26.0965	27.7018	Sampled similar to #3
# 10	#8 Shaft	Mine water (A)	26.1354	27.7201	Sucked water through a pipe into a bucket then immersed measuring containers
# 11	B. van Vuuren borehole	A borehole in a farm (A)	26.1038	27.7001	Using small hose inserted into a big borehole hose pipe
# 20	Lodge Spring	Deep groundwater (dolomite) (A)	26.0904	27.7163	Using a big bottle to fill measuring containers
# 22	Black Reef Incline	Mine water (A)	26.1152	27.7231	Using a bailer
# 23	#18 Winze	Mine water (A)	26.1151	27.7249	Using a bucket connected to a rope then containers filled from the bucket
# 26	Artesian borehole	Artesian in vicinity of mines (A)	26.1123	27.7228	Measuring containers filled directly
# 30	Spring 2 Cemetery	Deep groundwater (dolomite) (A)	26.0981	27.7189	Container immersed below surface
# 34	Krugersdorp Brick Works borehole	Borehole running continuously (A)	26.0633	27.6967	A bucket filled then measuring containers immersed in the bucket
# 37	Poplar Spring	Deep groundwater (A)	26.0909	27.7201	Immersing containers
# 49	Valley borehole	A farm borehole (A)	26.1219	27.6875	Flushed then containers filled directly from the borehole hose pipe
# 50	Valley Spring	Spring's dam ⁸ (A)	26.1241	27.6833	containers immersed under surface of a running stream
# 55	Aviary Spring	Deep groundwater	26.0775	27.7009	Immersing containers
# 57	P. Schutte borehole	Deep borehole (A)	26.0476	27.7123	Sampled similar to #3
# 59	#17 Winze	Mine water (overflowing) (A)	26.1215	27.7214	measuring container filled directly ⁹
# 62	Scavenger borehole	Shallow borehole (A)	26.1142	27.7226	a bailer was used
# 63	Spring 1 Cemetery	Deep ground water (A)	26.0981	27.7196	Sampled similar to #30

⁸ The spring issue point was not accessible. Samples were collected from a stream running out of the spring dam.

⁹ Water overflows from underneath a cover of a shaft. There was a hole in the middle of the cover but water has also pushed through the edges of the cover. Samples were taken from the hole.

Table 5-1 continued.

V-TW-20	N/A	Surface/stream (B)	Not available	Not available	A bottle was used to fill containers
V-TW-22	N/A	Surface/Sump	26.9659	26.7347	Similar to V-TW-020
V-TW-26	N/A	Spring at bottom of slipway (B)	26.9677	26.7308	Containers immersed under water surface
V-TW-28	N/A	Further from slipway (B)	26.9676	26.7307	Bottle attached to a rope spanned across slipway
V-TW-29	N/A	Surface/sump	26.9659	26.7347	Similar to V-TW-020
V2-TW-04	N/A	Surface/wet reeds (B)	26.9634	26.7403	Containers immersed directly
V2-TW-07	N/A	Surface water from a dam (B)	26.9477	26.7610	Containers filled using a bailer
V2-TW-08	N/A	Surface/sump (B)	26.96577	26.7346	Containers filled by a glass beaker
V2-TW-14	N/A	Shallow borehole Water (B)	Not available	Not available	Water collected by Nitrogen bailer then decanted into containers
V2-TW-22					
V2-TW-23					

The difficulties with sampling streams, which were shallow in most cases, were that subsamples for NECSA, iTL-G, RAD7 and HPGe were not taken from one mother sample. Sometimes, we had to collect water from two nearby positions to add up to one subsample as in the case of the 1.3 liter Marinelli beaker for the HPGe measurement. For the NECSA samples, no serious problem of sampling was encountered since the required 7 ml of water are usually syringed from one of the other subsamples. The sample was prepared by dispensing the 7 ml water through a 0.45 mm filter into a vial containing 13 ml of Ultima Gold LLT scintillation liquid and shaking the vial thoroughly to mix the liquid. The RAD7 samples were not problematic as the vial of volume 250 ml was relatively small and was easily filled. For the LSC (iT_L_G), radon was concentrated by adding 30 ml Ultima Gold LLT scintillation liquid to one liter water sample. Then, after shaking the mixture for about five minutes, 20 ml of radon concentrated liquid (aliquot) was recovered and sealed in the LS counting vial. More details on sample preparation for the various techniques are presented in CHAPTER 3.

We would like to point out that since the aim of the current study was to check and compare the sensitivity of the various techniques for measuring radon in mine areas; only samples of radon concentrations above MDA are presented.

5.3.2 *In-situ measurement*

In-situ γ -ray spectrometry was carried out in the Vaal River using the iThemba LABS MEDUSA system, which was described in CHAPTER 3, subsection 3.3.2.3. The

aim of the *in-situ* measurements was to test the sensitivity of the MEDUSA system for measuring radon in the river water.

The *in-situ* measurements comprise two sets of MEDUSA data acquired during a field trip to the Vaal River. The first set of data (see Table 5-2) were measured on the 5th Sept. 2006 and acquired by deploying the MEDUSA detector from overboard a boat moving along the river. For these measurements, the detector was suspended in the water at estimated depths not less than one meter below the surface and two meters above the riverbed. Attention is drawn to the fact that during these measurements, some spectra were acquired while the detector was held stationary. The suspended detector was expected to see mainly γ -rays originating from nuclides in water.

The second data set was acquired with the detector dragged on the river bed (RB) moving towards the bank and back (see Table 5-2). In this geometry, the detected γ -rays would be dominated by γ -ray emitted from nuclides within the riverbed matrix. The spectra details together with their corresponding detector's geometry and mode of measurement are presented in Table 5-2.

The MEDUSA software MDL (MEDUSA Data Logger) recorded counts every two seconds and, for the current study, an average of four minutes acquisition time makes up one spectrum. The measurement procedure for the MEDUSA system is described in more detail in CHAPTER 3.

Table 5-2: Summary of the *in-situ* γ -ray spectrometry measurements showing the MEDUSA measurement ID¹⁰, time of measurement, the detector measuring geometry, and the mode of measurement.

spectrum ID	Measurement		Geometry	Mode
	begin	end		
vr050906.m01 to vr050906.m14	10h28	16h07	suspended	moving
vr050906.m20	16h48	16h52	dragged	moving

5.4 Analysis procedures

The Durridge RAD7 radon monitor, described in CHAPTER 3 (subsection 3.2.2), measures radon in water by stripping off radon-rich air from the water sample, drying the air and recording the spectra of alpha particles emitted from ²¹⁸Po and ²¹⁴Po in

¹⁰ The ID reflects the area of measurement, date of measurement and the extension describes the spectrum number e.g. vr050906.m15 reads: Vaal River, measured on 05.09.2006 and spectrum no. 15.

equilibrium with ^{222}Rn . This procedure is also described in CHAPTER 3, subsection 3.2.2.2.

In the laboratories of NECSA, the vials were counted twice: the first time after more than three hours from time of sampling to achieve radioactive equilibrium between radon and its daughters and the second time after three weeks to correct for supported radon. At the iThemba LABS-Gauteng (iTTL-G), the vials were counted for 50 minutes each after radon reached equilibrium with ^{218}Po and ^{214}Po (3 hrs) using the liquid scintillation (LSC). One notices that supported radon is not corrected for in this procedure. For the non-destructive γ -ray spectrometry, the Marinelli beakers were transported by plane to iThemba LABS in Cape Town and measured on the HPGe detector. The transport of samples causes a delay of two or three days before the HPGe measurements commenced. This has, in addition to statistical uncertainties, a consequence of some systematic effects being introduced due to possible radon loss caused by the shaking of samples during transport and radon build-up due to supported radon.

All the techniques and their measurement procedures are described in detail in CHAPTER 3. Table 5-3 summarizes the measurement mode, the sample size, and the minimum detectable activity (MDA) of the various techniques listed.

Table 5-3: Measurement mode, sample size, measuring time and the minimum detectable activity (MDA) for the various techniques used in this study to measure radon in water.

Technique	Measurement Mode	Sample size (ml)	Measuring time	MDA
RAD7	In-field	250	30 minutes	0.4 Bq/l
HPGe	Laboratory	1300	2 hrs	0.2 Bq/l
LSC (NECSA)	Laboratory	7	3 hrs	0.095 to 6.6 Bq/l ¹¹
LSC (iTTL-G)	Laboratory	1000 ¹²	50 minutes	0.9 CPM ¹³

The *in-situ* gamma-ray spectra were analyzed using the MEDUSA Data Synchronizer (MDS) and MEDUSA Post Analysis (MPA) software packages. The MPA involves using the full spectrum analysis (FSA) method (described in CHAPTER 3, subsection 3.3.2.3). As discussed in CHAPTER 3 (section 3.4), the FSA method

¹¹ Depending on radon concentration because of correction for supported radon.

¹² The radon in the 1000 ml water sample was concentrated by adding 30 ml Ultima Gold LLT scintillation liquid from which an average amount of 20 ml radon concentrated liquid (aliquot) can be extracted at the end.

¹³ This is the minimum counts per minute, which corresponds to the MDA of the iTTL-G LSC if it is calibrated for efficiency.

applies three standard spectra of ^{40}K , ^{232}Th series and ^{238}U series, simulated using the MCNPX code in the geometry of a flat bed, and the Theewaterskloof (Twk) background spectrum.

The results from the application of the MEDUSA software did not give good results for the radon activity in the Vaal river water due to the interference of the γ -rays originating from the soil of the river bottom and river banks. The measured spectra were then studied in order to try to extract relevant information on the Rn levels in the water.

5.5 Results

This section presents results of uranium, supported radon and total radon concentrations. The total radon results obtained by the RAD7, the HPGe and the LSC (NECSA) and the LSC (iTTL-G) will be compared. In addition, results of the *in-situ* γ -ray spectrometry using the iThemba LABS MEDUSA system will be discussed.

5.5.1 Uranium and supported radon results

Table 5-4 presents the concentrations of ^{238}U , ^{235}U , ^{234}U and supported ^{222}Rn in samples collected from the WRB area. At the NECSA laboratories, the samples were prepared by filtration of suspended solids (procedure WIN-121) and measured with alpha spectrometry (procedure WIN-145) [Kotze *et al.*, 2008]. Excluding ^{235}U , the results show noticeable concentrations of these radionuclides, to less extent supported ^{222}Rn , in samples #22, #23, #26, #59 and #62 (mainly from the mine acid drainage). By contrast, the concentrations of the nuclides, except ^{234}U , are very low in samples #20, #30, #37, and #63 (mainly from the springs). It can be noted that the supported ^{222}Rn is generally insignificant except for sample #59, which has a concentration of 1.380 ± 0.020 Bq/l. The ratios between the various nuclides calculated from their respective activities are also presented in Table 5-4. The $^{235}\text{U}/^{238}\text{U}$ ratios of all samples are statistically consistent with the natural abundance ratio of $^{235}\text{U}/^{238}\text{U}$: 0.046. This might indicate the integrity of the measuring technique applied to these samples. On the other hand, the $^{234}\text{U}/^{238}\text{U}$ ratios of all but the spring samples are slightly above unity, which indicate the natural occurrence of the ^{238}U series in a closed system. Often high $^{234}\text{U}/^{238}\text{U}$ ratios in groundwater are related to the presence of ^{234}U in excess of ^{238}U . One of the mechanisms responsible for the extra ^{234}U is the recoiling of the relatively short-lived nucleus ^{234}Th after α -decay of ^{238}U . The very high activity ratios of $^{234}\text{U}/^{238}\text{U}$ associated

with spring samples of this study, which indicates disequilibria in the ^{238}U series, are characteristic of the dolomitic aquifer in the area. Kronfeld *et al.* (1994) investigated the extreme $^{234}\text{U}/^{238}\text{U}$ disequilibria in this aquifer and attributed the high $^{234}\text{U}/^{238}\text{U}$ activity ratio to an ion exchange mechanism in which α -recoil preferentially ejects ^{234}Th into the water when ^{238}U , present in thin layers on rock surfaces, decay. Eventually, ^{234}Th decays to ^{234}U , which remains in groundwater.

Table 5-4: Activity concentrations of ^{238}U , ^{234}U and ^{226}Ra for 10 samples collected together with the radon samples in Table 5-5 from the WRB area. The samples were prepared (by the procedure of filtration of suspended solids) and measured (using alpha spectrometry) by the laboratories at NECSA [Kotze *et al.*, 2008]. The table also shows the activity ratios calculated from these concentrations.

Station #	^{235}U (Bq/l)	^{238}U (Bq/l)	^{234}U (Bq/l)	supported ^{222}Rn (Bq/l)	$^{235}\text{U}/^{238}\text{U}$ ratio	$^{234}\text{U}/^{238}\text{U}$ ratio
# 20	0.0009(3)	0.019(6)	0.569(11)	0.025(3)	0.05(2)	30(9)
# 22	0.073(3)	1.59(7)	1.93(8)	0.68(3)	0.046(3)	1.21(7)
# 23	0.084(4)	1.82(9)	2.09(10)	0.82(3)	0.046(3)	1.15(8)
# 26	0.11(3)	2.47(12)	3.20(14)	0.122(7)	0.044(11)	1.30(8)
# 30	0.0005(2)	0.012(4)	0.196(6)	0.0031(12)	0.05(2)	16(5)
# 37	0.0003(2)	0.006(4)	0.018(6)	0.019(3)	0.05(4)	3(2)
# 55	0.0013(3)	0.027(7)	0.038(8)	0.0029(14)	0.046(17)	1.4(5)
# 59	0.080(18)	1.75(8)	1.94(9)	1.380(20)	0.046(11)	1.11(7)
# 62	0.091(16)	1.87(7)	2.22(8)	0.462(12)	0.049(9)	1.19(6)
# 63	0.0007(2)	0.014(5)	0.026(7)	0.011(5)	0.05(2)	1.9(8)

5.5.2 Total radon results

Table 5-5 presents the total radon concentrations measured by the HPGe, the RAD7 and the LSC (NECSA) techniques for the WRB area. It was observed that the uncertainties associated with the RAD7 are relatively large compared to the other techniques. This could be attributed to the counting statistics caused by the low efficiency of the RAD7 (see CHAPTER 3, intermezzo 3.1). One also notices from Table 5-5 that the results of the three techniques are comparable within statistical uncertainties in most of the samples. However, in some of the samples e.g. stations #20, #26, # 37, # 59 and # 63, relatively big discrepancies are noted particularly between NECSA results and the results of the remaining techniques. Generally, the RAD7 and the HPGe results agree except sample # 59. One obvious reason for these discrepancies is the probable systematic effects due to variations during sampling as discussed in subsection 5.3.1. However, it was noted that some of the samples that are associated with large discrepancies in total radon measurements also have high disequilibria ratios in the NECSA measurement of $^{234}\text{U}/^{238}\text{U}$ e.g. #20, #30, and # 37.

Table 5-5: Total radon concentration of samples from study area A measured using the RAD7, the HPGe, and the LSC (NECSA). The “-” means sample was not measured with the respective technique. The first column is the sample source code.

Station #	HPGe (Bq/l)	RAD7 (Bq/l)	LSC(NECSA) (Bq/l)
# 03	-	14.2±1.4	-
# 05	-	66±3	-
# 10	-	16±3	-
# 11	-	21.3±0.7	-
# 20	58.1±0.7	65±4	39.5±0.5
# 22	-	29±3	21.1±0.4
# 22	30.4±0.6	29±3	-
# 23	-	11.6±2.2	16.2±0.4
# 23	15.3±0.4	14.1±1.6	-
# 26	-	46±3	26.8±0.7
# 26	40.1±0.8	47.8±1.5	-
# 30	54.0±1.0	54±3	42.9±0.5
# 34	-	11.0±1.7	-
# 37	18.6±0.5	21±4	14.1±0.3
# 49	-	37±4	-
# 50	-	1.5±0.4	-
# 55	-	3.5±0.5	2.23±0.13
# 57	-	12.0±0.6	-
# 59	-	16.6±0.9	-
# 59	26.3±0.6	14±5	19.1±0.4
# 62	-	40.9±2.0	43.5±0.6
# 63	-	69±3	53.3±0.6

Results of total radon in the samples from study area B (the Vaal River) are presented in Table 5-6. The RAD7, the HPGe and the LSC (NECSA) results are presented in Bq/l while the LSC (iTL-G) gives un-calibrated measurements in counts per minute (CPM). The correlation between the various techniques is presented in Figure 5-2. One notices that there is reasonable agreement (within statistical uncertainties) between the various techniques.

Firstly, consider the RAD7 and the LSC iTL-G results. Several samples were measured using both techniques but only three were found to have radon concentration above the MDA of the RAD7 and thus presented in Table 5-6. The two techniques show good correlation as the least squares fit shows a reduced chi-square value of 1.8. From the fit, the slope was found to be 9.4 ± 0.2 CPM/(Bq/l). The reciprocal of this slope: 0.106 ± 0.002 (Bq/l)/CPM thus represents a conversion factor for counts per minute to Bq/l for the results from the iTL-G LSC.

Also shown in Figure 5-2 are the correlations between the results from the RAD7 and the other three techniques fitted with least-squares minimization procedure (solid lines). The correlation between the RAD7 and the HPGe results was determined with a

weighted fit yielding a slope of 0.90 ± 0.04 (Bq/l) / (Bq/l) and a reduced chi-square value of 2.7. This slightly high value of chi-square reflects systematic effects, most likely due to sampling procedure. This is supported by the discrepancy noticed between the RAD7 and the HPGe results for radon of sample #59. The correlation between the RAD7 and the LSC (NECSA) results yields a least-squares fit slope of 0.80 ± 0.07 (Bq/l)/(Bq/l) and a reduced chi-square value of 7. This high chi-square value reflects systematic effects possibly due to discrepancies in almost 50% of the data points. It must be noted that these points are mainly spring samples. One obvious reason for these discrepancies was the sampling procedure discussed in subsection 5.3.1. However, the discrepancies in 50% of the data may suggest more than one source of systematic effect. The current data were not enough to investigate whether water samples with extreme U-series disequilibria are associated with some systematic uncertainties when radon is measured by alpha spectrometry.

Table 5-6: Radon concentrations of samples from study area B measured using the RAD7, the HPGe, the LSC (iTL-G) and the LSC (NECSA). The reported results represent total radon concentration except for the NECSA results, which represent the unsupported radon concentration.

Sample field code	RAD7 (Bq/l)	HPGe (Bq/l)	iTL-G (CPM)	NECSA (Bq/l)
V-TW-020	-	-	2.8 ± 0.8	3.6 ± 0.6
V-TW-022	5.3 ± 0.7	-	51 ± 2	-
V-TW-026	16.6 ± 1.4	-	154 ± 4	-
V-TW-028	0.8 ± 0.3	-	5.5 ± 0.9	-
V-TW-029	5.5 ± 0.4	5.3 ± 0.3	-	-
V2-TW-04	7.1 ± 2.2	-	-	6.0 ± 1.4
V2-TW-04	6.7 ± 0.6	-	-	5.7 ± 1.2
V2-TW-07	1.2 ± 0.6	-	-	1.1 ± 0.6
V2-TW-08	5.0 ± 0.7	-	-	4.4 ± 0.9
V2-TW-14	1.2 ± 0.7	-	-	1.8 ± 0.7
V2- TW -22	-	2.4 ± 0.3	-	1.8 ± 0.7
V2- TW -23	-	1.0 ± 0.2	-	1.4 ± 0.7

In view of these results, the iTL_G based LSC method seems to be more suitable for measuring low concentrations of radon in water. This could be related to sample preparation described in subsection 5.3.1. However, the iTL-G is a laboratory-based technique and results can only be received after the field trip has been completed.

The concentrated radon samples could also be measured with γ -ray spectrometry using a HPGe detector [Shizuma *et al.*, 1998]. However, the LSC method (iTL-G) has the advantage of measuring many samples automatically whereas the HPGe technique is manual and sample throughput is much slower.

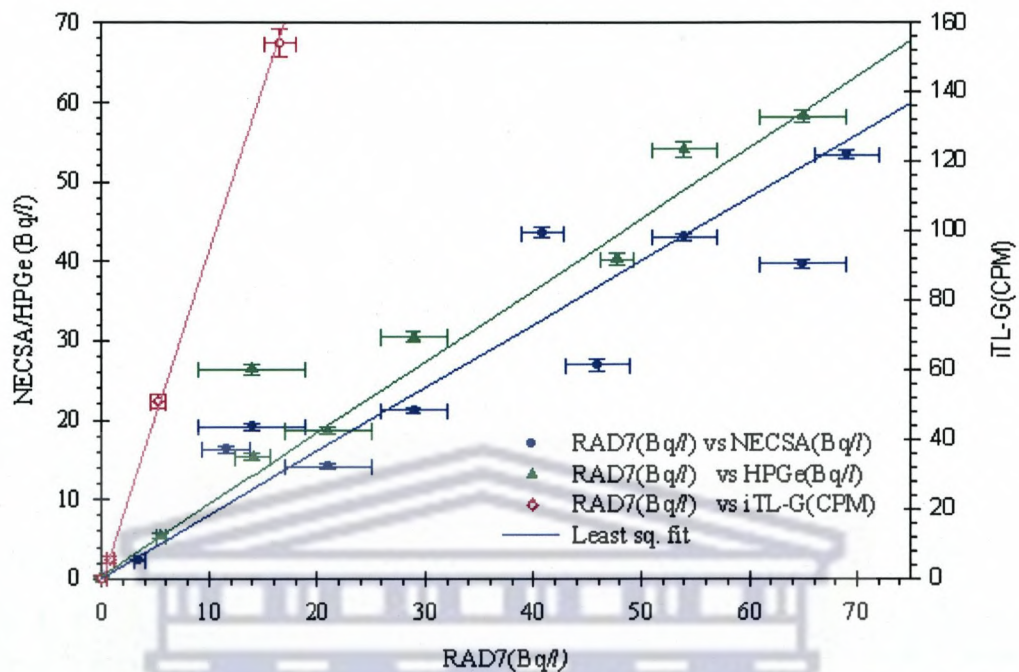


Figure 5-2: Correlation between the various techniques applied to measure radon in water samples collected from the WRB and the Vaal River mining areas. The iTL-G results (CPM) are plotted on the right y-axis. The left y-axis represents radon concentration (Bq/l) obtained by either the NECSA LSC or the HPGe detector. The solid lines represent a weighted fit by means of least-squares minimization procedures.

5.5.3 *In-situ* MEDUSA results

When the MEDUSA detector was suspended under water, at least 1m away from both the water surface and the riverbed, it was expected to be predominantly exposed to γ -rays originating from radionuclides in water. In this geometry, the detector is reasonably shielded from radiation emitted from riverbed and riverbanks. However, since the riverbed was not flat, the measurement depths might vary. Unfortunately, the depth was not monitored during these measurements. Therefore, we first investigated the nature of the measurements by analyzing the distribution of total counts as shown in Figure 5-3. As described in section 5.4, the MEDUSA detector recorded counts every two seconds (cp2s) and thus total count rate (TC-rate) here refers to total counts per two seconds. The top plot of Figure 5-3 shows spatial (latitude and longitude positions) change of total counts in the energy range 0.6 – 2.8 MeV along the track of a moving boat. One notices that the total counts are generally low with a maximum of 15 counts as can be read from the color code on the right-hand side of the plot. Even within these low counts one observes few relative hot spots (red color) which could possibly reflect

either that the detector was close to the river bed or it could correspond to measurements near inlets of streams potentially enhanced in radionuclides.

The middle part of Figure 5-3 shows the TC-rate distribution. The figure shows in addition to the dominant part with TC-rate < 20 cp2s, a broad, low intensity range with $20 < \text{TC-rate} < 100$ cp2s. To investigate the origin of the count rates, four graphs of data were selected. The first subgroup contains spectra measured in the shallow part of the river. This subgroup is presented in the bottom plot of Figure 5-3. The second subgroup, shown in the top plot of Figure 5-4, contains spectra measured in the deep part of the river. The third subgroup was measured while the detector was held stationary in deep water. The TC-rate distribution of this latter subgroup is presented in the middle plot of Figure 5-4. It can be seen that the TC-rate distribution of these three subgroups looks similar with a maximum TC-rate around 20 cp2s. The fourth subgroup was measured with the detector stationary near the river bank opposite to inlets of streams. The TC-rate distribution is presented in the bottom plot of Figure 5-4. This latter plot shows that this subgroup partly has TC-rate of more than 20 cp2s. Two further spectra were obtained: one for the various subgroups with TC-rate less than 20 cp2s and the second was for the fourth subgroup with TC-rate above 20 cp2s. These spectra are plotted in Figure 5-5 together with a background radiation spectrum measured at the Theewaterskloof dam. This background spectrum was mainly due to cosmic radiation and terrestrial radiation from materials of the detector and its associated accessories. It is noticed that the spectrum of TC-rate less than 20 cp2s and the background spectrum have similar shapes (horizontally) but differ slightly in magnitude (vertically) towards the lower energy part, as Figure 5-5 shows. This difference in magnitude at low energy is likely due to absorption of the soft energy part of the cosmic background radiation by the 1m water layer. The Theewaterskloof dam is almost at sea level whereas the average altitude at the Vaal River area is about 1200 m above sea level. Thus one would have expected the background cosmic radiation to be higher at the Vaal river area. The fact that the deep Vaal River spectrum is similar to background, or less than the background spectrum at low energies, implies that the radon in the river water is below the sensitivity of the detector. In fact, grab sample measurements with the various techniques discussed in subsection 5.5.2 show that the radon concentration in the deep river water is below the MDAs of these techniques.

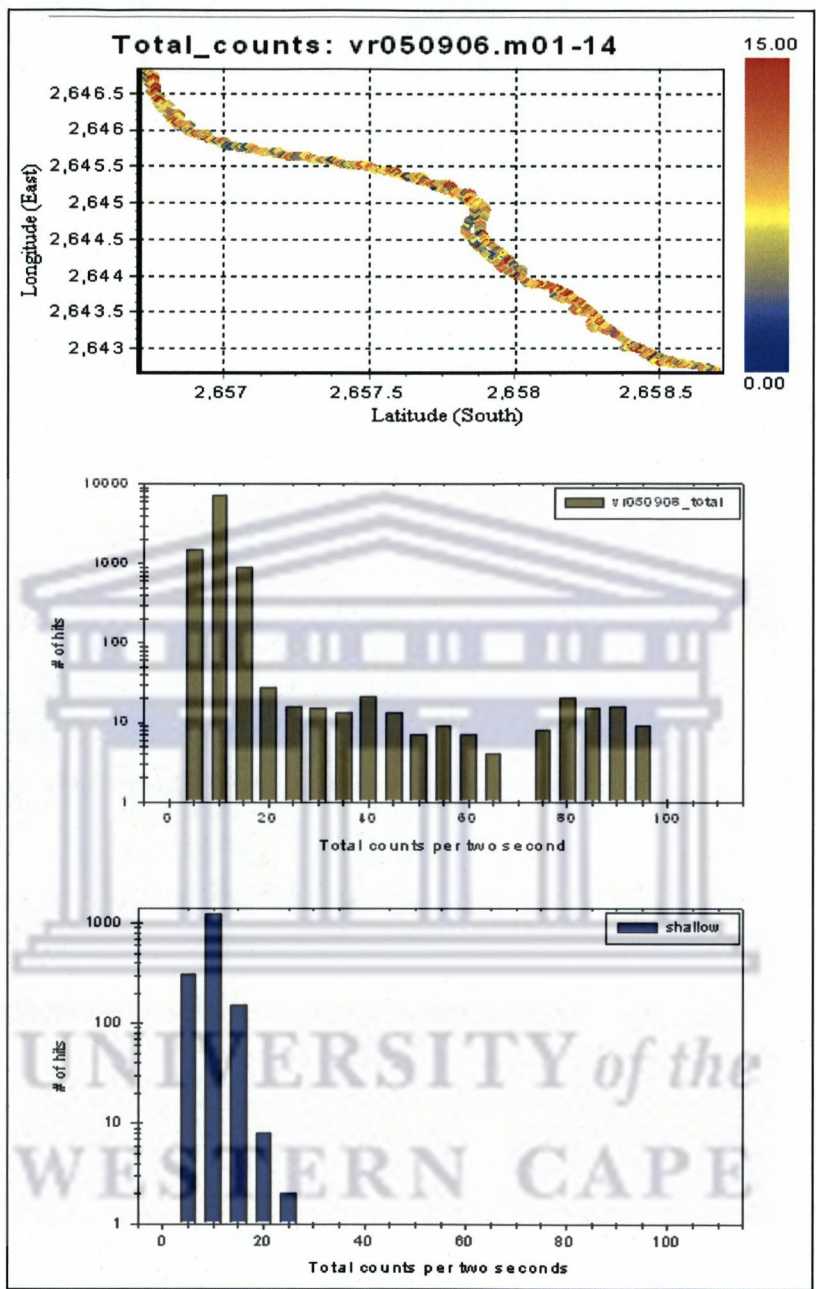


Figure 5-3: *In-situ* MEDUSA measurements along the Vaal river with the detector suspended. The top plot shows the spatial change of total counts along the track of the boat pulling the detector in the river. The latitudes and longitudes shown in the plot are in the format x,xyy.y where xx and yy are degrees and minutes, respectively. The middle plot shows the distribution of total counts per 2 second (referred to as TC-rate) for the whole range of the measured data. The bottom plot shows the TC-rate distribution at shallow parts of the river.

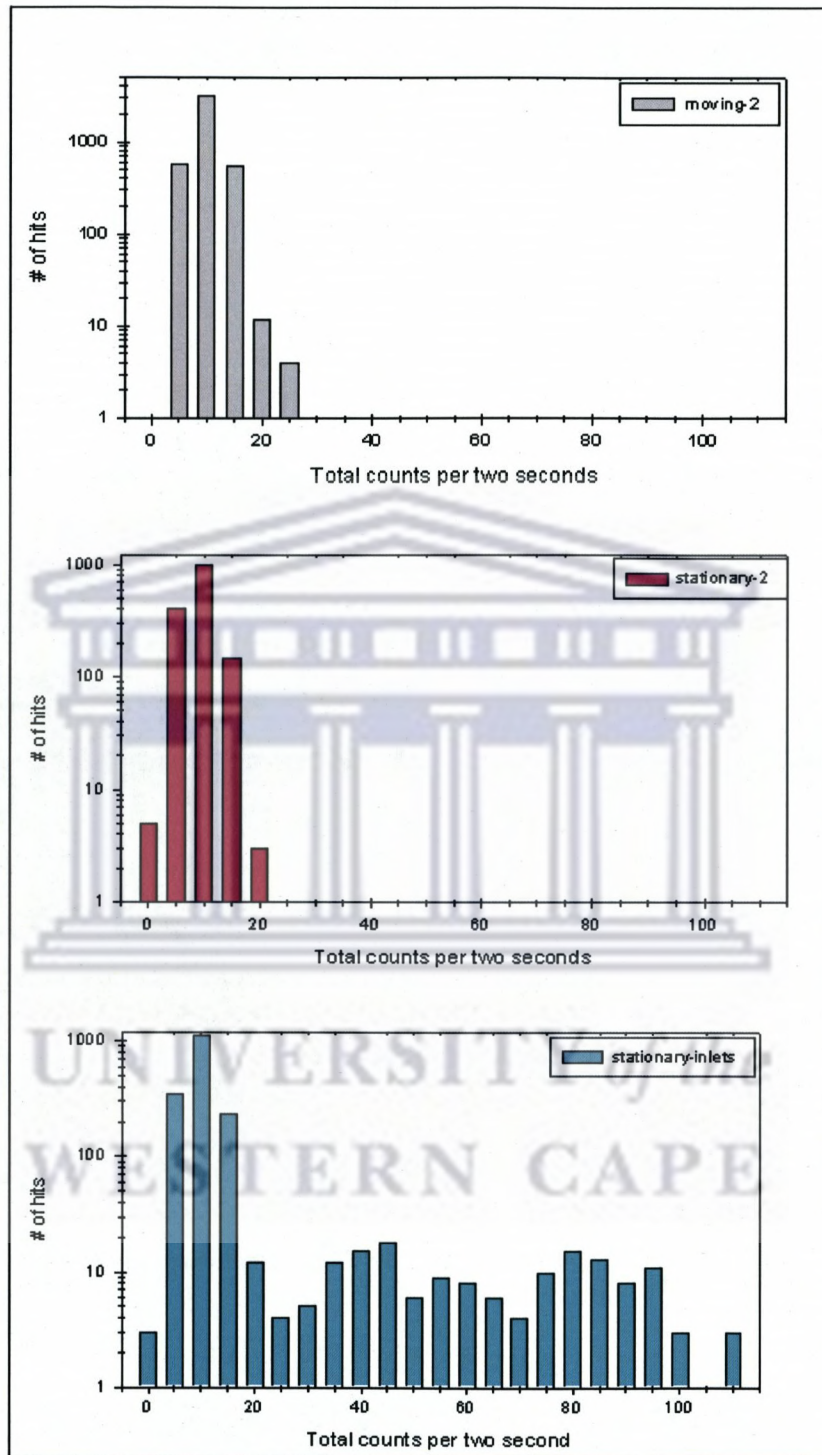


Figure 5-4: *In-situ* MEDUSA measurements along the Vaal river with the detector suspended in the water. The top plot shows the distribution of total counts per 2 second (referred to as TC-rate) while the boat was moving. The middle plot shows the TC-rate distribution in deep water for stationary measurements. The bottom plot shows the TC-rate distribution for stationary measurements where streams are entering the river.

The spectrum measured near inlets (with TC-rate > 20 cp2s) shows clear peaks above the background spectrum as presented in Figure 5-5. Examples of the peaks are

1.46 MeV (^{40}K), 1.76 and 2.2 MeV associated with ^{214}Bi (^{238}U -decay series) and 2.61 MeV (^{232}Th -decay series). These pronounced peaks are likely to be dominated by activity from the bottom due to the shallow depth and enhanced by activity from river banks.

If we assume that the peaks 1.76 and 2.2 MeV in the spectrum of Figure 5-5 were due to radon in water, the concentration of this radon can be estimated by determining the net count rate in the energy range $1.6 < E_\gamma < 2.4$ MeV. The net count rate was determined after subtracting cosmic radiation and thorium contributions to the set energy region. This procedure of analysis is called the hybrid approach and is described in detail in CHAPTER 6 (section 6.3). The net count rates after subtracting the Theewaterskloof background in the same energy range were determined to be 0.96 ± 0.19 cps for spectrum `stat_inlets>20 TC` (Figure 5-5). Dividing by the content of a simulated and calibrated standard spectrum of U/Rn: 0.180 ± 0.005 cps/Bq l^{-1} ; the corresponding radon concentration was estimated to be 3.4 ± 1.2 Bq/l for the spectrum `stat_inlets>20 TC` in Figure 5-5. Please note that the standard spectra used in these estimations were simulated for the geometry of the MEDUSA-tank (see CHAPTER 6). The quoted uncertainty is 1σ statistical uncertainty and appears to be high most likely due to the very short measuring time (about five minutes).

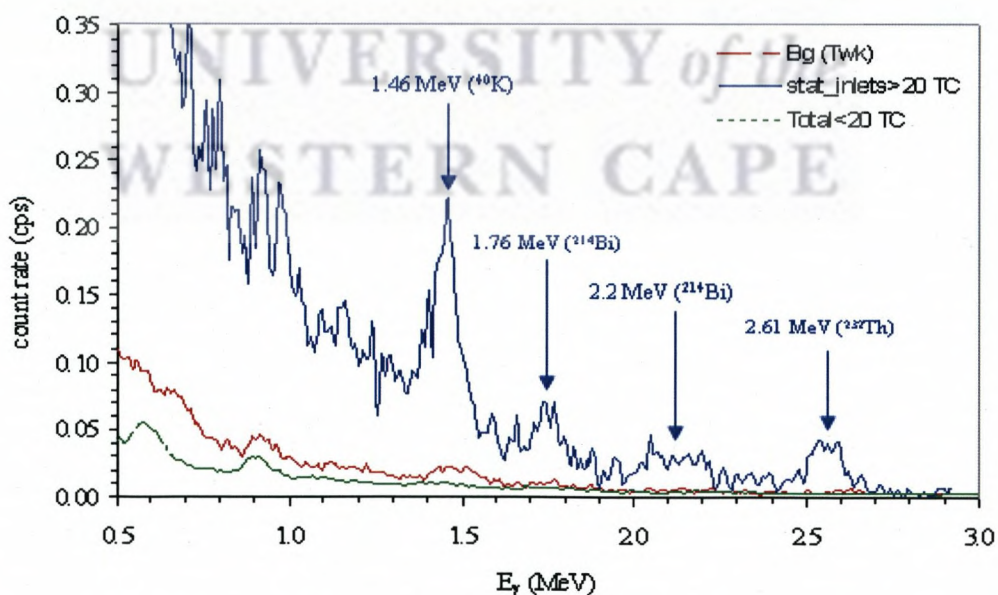


Figure 5-5: Spectra measured using the MEDUSA detector. The blue solid line represents a portion of a spectrum (with total count (TC-rate) > 20) of stationary measurements in the vicinity of inlets in the Vaal River. The red dashed-line is a background spectrum (cosmic radiation) measured (near surface) in the Theewaterskloof dam. The green dotted-line is a spectrum (with TC-rate < 20) measured while the detector was suspended in the Vaal River water.

The minimum detectable activity for the MEDUSA detector for measuring radon *in-situ* was also estimated from analyzing the Theewaterskloof background spectrum in a similar way as discussed in the above paragraph, and by using the MDA relation given by Eq. 2-8 and the five minutes measuring time of the *in-situ* spectra. The background count rate in the energy range $1.6 < E_\gamma < 2.4$ MeV was determined to be 0.513 cps in a measuring time of 4549 seconds. This calculation leads to an MDA value of 0.8 Bq/l. This latter value is about a quarter of the radon concentration estimated from the spectra in Figure 5-5.

Measurements with the detector close to the riverbed do not yield radon concentration in the water but reflect bottom activity. An example of these measurements is the vr050906.m20 measured with the detector dragged on the riverbed. A comparison between the riverbed spectrum and the Theewaterskloof background spectrum is presented in Figure 5-6. The figure shows clearly that the riverbed activity is considerably higher than background. In terms of spectral shape, some peaks such as the 2.61 MeV (from Th-decay series), towards the end of the high energy part of the spectrum, becomes more pronounced possibly due to radiation emitted from the riverbed.

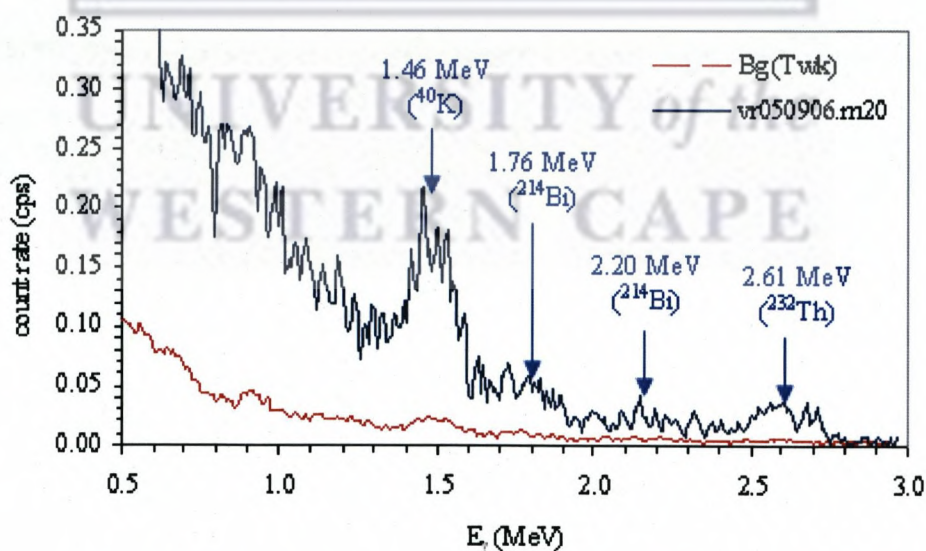


Figure 5-6: Two spectra measured with the MEDUSA system. The blue solid-line represents measurement data file vr050906.m20 in the Vaal River with the detector dragged on the riverbed whereas the red dashed-line is the Theewaterskloof (Twk) background spectrum.

Similar to the discussion of the U/Rn peaks in Figure 5-5 above, the equivalent radon concentration extracted from data file vr050906.m20 (Figure 5-6) was estimated

to be 2.9 ± 1.2 Bq/l. Again this concentration is a factor of 3.6 higher than the MDA and the high uncertainty is most likely due the short measurement time (five minutes).

The dragged detector measurement was also analysed further with the MEDUSA software packages. Spatial distribution of relative activity concentration of the nuclides K, Th-decay series and U-decay series, respectively, was plotted as shown in Figure 5-7 (a), (b) and (c). It must be borne in mind that the simulated standard spectra were not calibrated for this geometry (flat bed) and therefore these concentrations are not absolute.

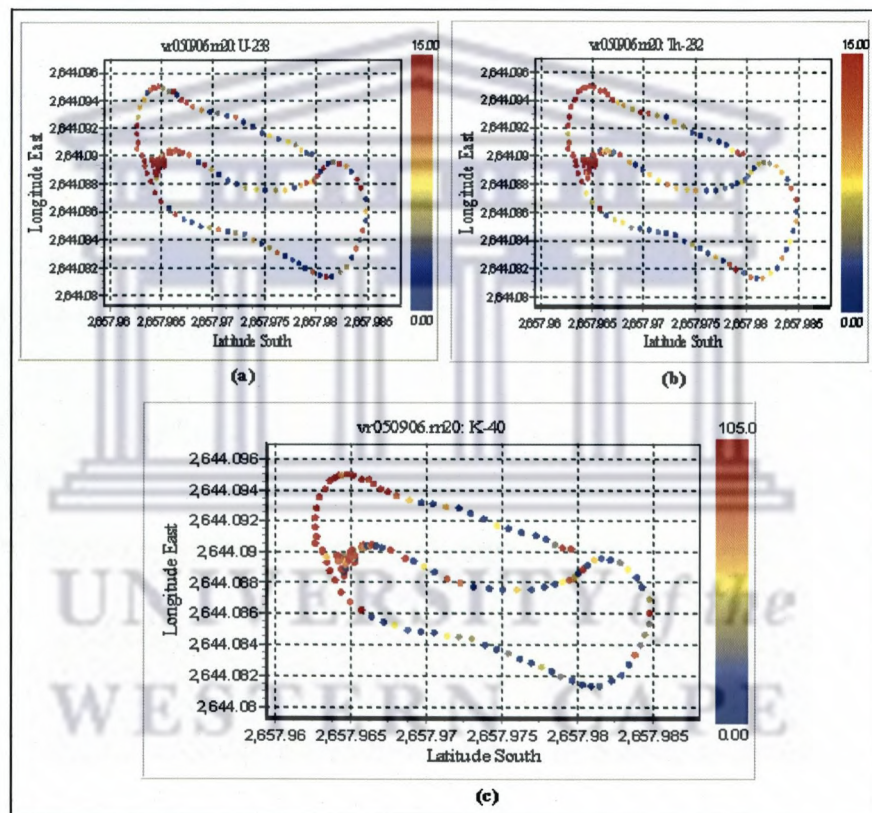


Figure 5-7: The response of the MEDUSA detector dragged on the riverbed while the boat was moving (data file vr050906.m20). The three plots show the spatial distribution of activity concentration of nuclides (a) of the U-decay series, (b) of the Th-decay series, and (c) of the ^{40}K . The color code on the right hand side of each plot represents the gradual change of concentration along the measurement pathway for the respective nuclides. Note these activity concentrations are not absolute. The latitude and longitude coordinates have the same format as explained in Figure 5-3.

The color code on the right hand side of each plot of Figure 5-7 represents the respective nuclide concentration at a particular position, with red being the highest relative concentration. Notice that the three nuclides have almost similar pattern of hot spots (relative high concentration marked with red color) with a cluster of hot spots

around latitude and longitude (2,657.99; 2,644.09). Since there is no preferential trend in favor of the U-decay series, these activities are most likely due to γ -rays emitted from the riverbed. In fact, the number attached to the color code (showing maximum relative concentration) is dominated by K being 105 Bq/l while the Th and U shared a value of 15 Bq/l.

5.6 Summary, discussion and conclusion

Five techniques have been applied to measure radon in water in two mining areas: the West Rand Basin (WRB) near Krugersdorp and the Vaal River near Orkney. The techniques are: three alpha spectrometry techniques using the RAD7 in the field, and two liquid scintillation counters situated at NECSA and at iThemba LABS-Gauteng laboratories; two γ -ray spectrometry techniques using the laboratory-based HPGe detector based at iThemba LABS – Cape Town and the iThemba LABS MEDUSA detector *in-situ* in the Vaal River.

The MDA of the RAD7 and the LSC (NECSA) were relatively high compared to the other techniques. Most of the surface water samples have radon concentrations below these limits and were therefore not included in the comparison of the techniques. The measurements of supported radon and U concentration showed that the supported radon is insignificant for this set of samples. The $^{234}\text{U}/^{238}\text{U}$ ratio was found to be slightly above unity, except for spring samples from the WRB area. This is an indication that the U-series radionuclides exist in equilibrium in a closed hydrological system. The $^{234}\text{U}/^{238}\text{U}$ values of 16 and 30 in spring samples prove disequilibrium to be present in the ^{238}U series in the dolomitic aquifer, which is believed to be the source of these spring waters. This is generally in agreement with previous studies by Kronfeld *et al.* (1994).

The total radon results show that there is a good correlation between the RAD7 and the LSC (iTL-G) with chi-square value of 1.8. The RAD7 and the HPGe also show good correlation with a chi-square value 2.7 and slope 0.90 ± 0.04 (Bq/l)/(Bq/l). The slightly higher chi-square associated with the correlation suggests that some of the measurements might be associated with systematic uncertainties most likely associated with sampling. The LSC (NECSA) and the RAD7 have a reasonable correlation with slope of 0.80 ± 0.07 (Bq/l)/(Bq/l) and reduced chi-square value of 7. This value most likely indicates that the NECSA measured total radon concentrations are also prone to some systematic effects, which could partly be due to the sampling procedure.

However, it was noted that almost 50% of the data (mainly from WRB spring sample) were outliers. This might suggest the presence of more than one source of systematic effect. The present data set was not suitable to investigate whether water samples of extreme U-series disequilibria will be another source of systematic uncertainties when radon is measured by alpha spectrometry. It is suggested that further measurements need to be undertaken to investigate the possibility of systematic effects associated with alpha spectrometry of radon in water samples with extreme $^{234}\text{U}/^{238}\text{U}$ disequilibria.

In view of the presented results, it seems that the LSC (iTL-G) is more suitable for measuring water samples of low radon concentration. However, since this technique is laboratory based, the RAD7, which is less sensitive and can be used in the field, might be more useful in planning a sampling strategy in the field. The HPGe has the advantage of low MDA but it is also based at a laboratory (iThemba LABS-Cape Town), which is very far from the mining areas. This makes it impractical except for selected inter-comparison measurements.

The *in-situ* MEDUSA spectrometry technique was found to be insensitive to the levels of radon present in the highly diluted Vaal River water.

In conclusion, the RAD7 with its disadvantage of large uncertainties (due to collection efficiency), is more useful in measuring radon-in-water in the field. The *in-situ* MEDUSA measurements were not successful in picking up variation in radon concentration so as to identify possible inlet of mining water into the Vaal River.

In order to make use of the capabilities of the MEDUSA technology, we propose inserting the MEDUSA detector in a large volume container to measure radon in water in the field. The proposed set-up is expected to provide reasonable shielding of the detector from the terrestrial background radiation and encloses the water sample tightly for radon to be in secular equilibrium. The proposed set-up will be described in CHAPTER 6.

CHAPTER 6 IN-FIELD RADON MEASUREMENT IN WATER: A NOVEL APPROACH

A method is proposed for measuring radon in the field based on γ -ray spectrometry using a MEDUSA γ -ray detector inserted in a large volume container. This chapter presents a description of the method including a new approach of analyzing the γ -ray spectra measured using a MEDUSA detector. The chapter commences with an introduction followed by a description of the set-up and the analysis approach (sections 6.2 and 6.3). Measurements of water spiked with KCl for calibrating the detection efficiency of the set-up are discussed in sections 6.5. This is followed by measurements of ^{222}Rn in the field using a MEDUSA detector and comparing the results to their counterparts obtained by sealing subsamples in Marinelli beakers measured in the laboratory on a HPGe detector (section 6.4). Further investigation of background radiation and its various components, within the context of the proposed method, will be presented and the results will be discussed (sections 6.6 and 6.7). The chapter is concluded by a summary and conclusion (section 6.8).

6.1 Introduction

Many field-based measurements of γ -ray emitting radionuclides have been carried out using semi-conductor detectors (e.g. HPGe) and scintillation detectors such as NaI(Tl), CsI(Na), and BGO as described in CHAPTER 3. As outlined there, two approaches of analysis are frequently applied: “windows” centered on an individual radionuclide’s photopeak(s) of interest and full-spectrum analysis (FSA), which utilizes the entire spectrum. Although the FSA has clear advantages, the method depends on how well the standard spectra represent reality, and the assumption that the background is constant in time. In this work, we experienced that for the standard spectra, the fit to the peaks in the spectrum is sensitive to assumed Gaussian broadening of the peaks. This sensitivity is important in particular because in the chi-square approach of the fitting of the standard spectra to the data, the optimal value is determined mainly by the fit to the continuum.

In this chapter, we investigate the assumptions for the FSA by implementing a method that combines the advantages of both the FSA and the Windows method, the so-called hybrid approach. This approach will be described in section 6.3 and provides an

analysis of the γ -spectrum using wide, nuclide dominated windows and standard spectra for estimating continuum contributions.

The focus of this chapter will be on determining radon concentrations in groundwater in the field after grab sampling “a *quasi in-situ*” method. The study is aimed at exploring the possibility of using a MEDUSA γ -ray detection system [de Meijer *et al.*, 1996] and a container to measure radon-in-water in the field. In this study, two sizes of container were used in the investigation: a steel drum and a plastic tank of nominal volumes 210 liter and 1000 liter, respectively. Various quantities of KCl dissolved in tap water were employed to calibrate the efficiency of the detector in the two geometries. These measurements were also used to investigate the nature of the high energy part of the spectrum, considered here as “background”.

6.2 Experimental set-ups

Figure 6-1a shows the iThemba LABS MEDUSA detector (described in CHAPTER 3, subsection 3.3.2.2) mounted on top of a steel drum of dimension ~ 87 cm and ~ 57 cm for the height and diameter, respectively, at measuring position P1. P1 is a position close to the iThemba LABS building and to a pipe carrying low concentrations of radioactivity from radionuclide production facilities to the holding dams. The volume of the drum was measured using a bucket (volume ~ 10 l) to be 215 ± 5 litres. A hole to accommodate the MEDUSA detector was drilled in the middle of the drum’s upper lid. A support was designed to keep the MEDUSA detector upright when lowered into the drum. The support also has two O-rings to maintain tight sealing during measurement to avoid radon exchange with the outdoor air. The support is fitted on the MEDUSA detector in such a way that the centre of the MEDUSA CsI crystal coincides with the centre of the drum.

Figure 6-1b shows a plastic tank, which has the dimensions of about 110 cm diameter and 122 cm height (excluding the tank neck) at measuring position P2. P2 lies in the middle of a field (more than 20 meters away from the main building and the release pipe). The volume calculated from these dimensions is 1160 liter. The MEDUSA detector was mounted in a similar way to that of the drum except that the detector was positioned at a height of one meter from the bottom of the tank. The volume of the tank was also measured using buckets of tap water to be 1170 ± 10 liters.

Due to the uneven top of the tank, it was technically challenging to mount the detector tightly on top of the tank.

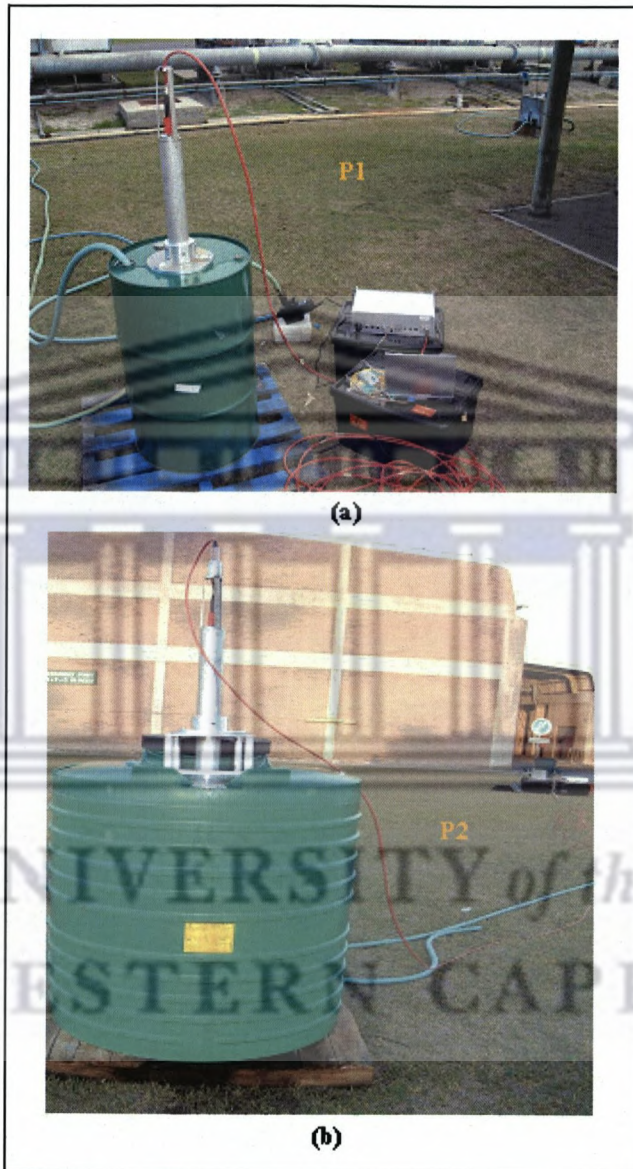


Figure 6-1 A photo of the iThemba LABS MEDUSA detector mounted on (a) a 210-litre steel drum beside a borehole at iThemba LABS at position P1. The MEDUSA accessories and a water pump can also be seen beside the drum; (b) a 1000-liter plastic tank at position P2.

6.3 Spectral analysis using the hybrid approach

Gamma-ray spectra in this study were analyzed by setting several energy gates (intervals) in the range of 1.3 to 3.0 MeV. This range covers the γ -rays emitted by the natural radionuclides of ^{40}K and those belonging to the decay series of Th and U. The

possible contribution of “minor” radionuclides to a certain gate for a “major” nucleus was estimated from standard spectra of the minor nuclei (K, Th and/or U/Rn). For the description of standard spectra, see CHAPTER 3, section 3.4.

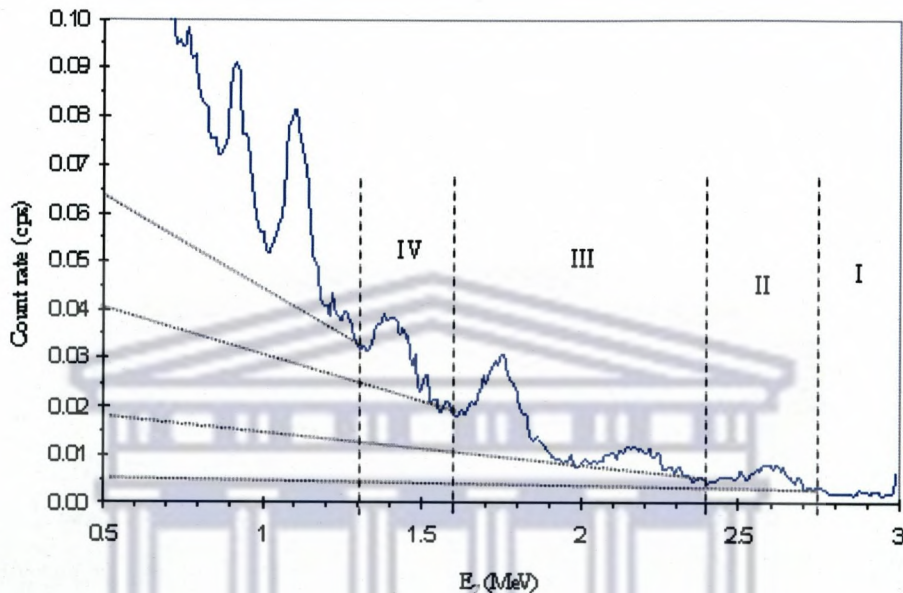


Figure 6-2: A MEDUSA measured γ -ray spectrum illustrating the four energy intervals of the hybrid analysis approach explained in the text. Starting from high energy, the intervals are: *I* (2.75 -3.0 MeV) the flat part of background cosmic; *II* (2.4 – 2.75 MeV) called Th and it contains mainly ^{208}Tl peak plus background; *III* (1.6 – 2.4 MeV) called U/Rn and contains mainly three ^{214}Bi peaks plus background; *IV* (1.3 – 1.6 MeV) called K and it contains mainly ^{40}K peak plus background. The horizontal dotted-lines schematically represent the continuum part related to the various energy intervals.

Since our main interest is in determining the radon (radon or Rn for short in this thesis refers to ^{222}Rn unless otherwise stated) concentration, the spectrum analysis is divided into two parts. The first part of the spectrum is the low-energy part of the spectrum containing the contribution of the ^{40}K . The second part, which is the relevant part for this work, is the high energy part not influenced by K: energy interval 1.6 - 3.0 MeV. Figure 6-2 shows a measured spectrum with a MEDUSA detector system and the four energy intervals: *I*, *II*, *III* and *IV*. The cosmic ray contribution will extend from the highest to the lowest channel. Above the highest terrestrial γ -ray (2.6 MeV; Th-series) we assume the background to be arising from cosmic rays only. The corresponding interval is set to $2.75 < E_{\gamma} < 3.0$ MeV (interval *I*). Interval *II* ($2.4 < E_{\gamma} < 2.75$ MeV) is considered to contain a major contribution of thorium (Th) in addition to cosmic rays. This Th is also present in the soil beneath and around the water container. The energy interval *III* ($1.6 < E_{\gamma} < 2.4$ MeV) contains, in addition to the contribution of the cosmic

rays and Th, the γ -rays of the U-series mainly at $E_\gamma = 1.73, 1.76$ MeV and at $E_\gamma = 2.2$ MeV. The interval is indicated as U/Rn. This U/Rn interval is sometimes split into two subintervals: III_a (containing the two peaks at $E_\gamma = 1.73$ and 1.76 MeV) and III_b (containing the peak at $E_\gamma = 2.2$ MeV).

We would like to point out that the nomenclature is somewhat ambiguous; on the one hand, the γ -ray spectrum of U contains a few weak γ -rays (mainly at low energies: <0.2 MeV) identical to the γ -ray spectrum of Rn and hence hard to discern. On the other hand, we would like to make a distinction between U and its decay products (including Rn) more or less in secular equilibrium present in the soil and Rn and its decay products present either in air or in samples of groundwater, not in secular equilibrium with U. Due to differences of their matrix, the U and Rn spectra may differ somewhat in shape due to differences in absorption. These effects are mainly expected at lower energy where multiple Compton scattering will contribute. In cases where we talk about energies of γ -rays, we will note them as U/Rn; if we refer to the U and its decay products in the soil we indicate them as U; radon in the air or water is referred to as Rn.

A cosmic ray spectrum (shown in Figure 6-3) was measured for 76 minutes on 21 Nov. 2002, using the MEDUSA system, near the surface of Theewaterskloof (Twk) Dam, which is a large, deep dam situated near Villiersdorp about 60 km from iThemba LABS, Cape Town. This spectrum (to be used as background) contains a minor contribution of Th and K activities present in the detector, its associated electronics and housing.

The analysis starts from the high energy side. The cosmic ray spectrum (referred to as cosmics) is assumed to have the shape of the Theewaterskloof spectrum, but it may differ in magnitude by a factor f_c , following from a comparison of the count rate (CR) of interval I in the actual spectrum, n_I , and that of the Theewaterskloof (Twk) spectrum, n_I^{Twk} :

$$f_c = \frac{n_I}{n_I^{Twk}}.$$

6-1

Next the CR of interval II , n_{II} , consists of the contribution of the cosmics and decay of Th in addition to minor contribution of U/Rn. The U/Rn is corrected for by multiplying the CR per Bq/l of the U/Rn standard spectrum in the interval, $n_{II}^{U/Rn-SS}$, by the quantity $C_{U/Rn}f$, which is discussed in Eq. 6-6. Hence, subtracting cosmics in the interval II by

using the Theewaterskloof spectrum CR in interval II, $n_{II}^{T_{wk}}$, multiplied by f_c yields the Th contribution:

$$n_{II}^{net}(Th) = n_{II} - f_c n_{II}^{T_{wk}} - f C_{U/Rn} n_{II}^{U/Rn_SS}. \quad 6-2$$

where $C_{U/Rn}$ is the effective U/Rn concentration and f is the detector calibration factor. This f factor, discussed in section 6.4 below, accounts for some of the detector properties, such as light-collection properties of the detector and the efficiency of the PMT, which are not included in the standard spectra simulated by MCNPX (see CHAPTER 3, section 3.4).

The effective Th concentration, C_{Th} , is obtained by dividing the net CR of Th in interval II, $n_{II}^{net}(Th)$, by the CR per Bq/l of the simulated standard spectrum of Th (Th_SS) in interval II multiplied by the detector calibration factor, f :

$$C_{Th} = \frac{n_{II}^{net}(Th)}{f n_{II}^{Th_SS}}. \quad 6-3$$

The uncertainty in f and f_c follows from the propagation of the statistical uncertainties. Systematic uncertainties arising from various assumptions have been ignored thus far. It should be pointed out that for intervals II, III and IV the following holds:

$$C_{Th} f = \frac{n_{II}^{net}(Th)}{n_{II}^{Th_SS}} = \frac{n_{III}^{net}(Th)}{n_{III}^{Th_SS}} = \frac{n_{IV}^{net}(Th)}{n_{IV}^{Th_SS}}. \quad 6-4$$

The net CR of U/Rn in interval III is obtained by subtracting the cosmics contribution using the f_c factor and the Th contribution:

$$n_{III}^{net}(U/Rn) = n_{III} - f_c n_{III}^{T_{wk}} - C_{Th} f n_{III}^{Th_SS}. \quad 6-5$$

The interval IV contains a correction for the U/Rn contributions in addition to the contributions of cosmics and Th. An effective U/Rn concentration, $C_{U/Rn}$ is calculated in a similar way to C_{Th} using the net CR in interval III, n_{III}^{net} , and the CR per Bq/l in interval III of a simulated standard spectrum of U/Rn (U/Rn_SS), which is given by the product of n_{III}^{U/Rn_SS} and the f -factor. *Mutatis mutandis* Eq. 6-4 may be written as:

$$C_{U/Rn} f = \frac{n_{III}^{net}(U/Rn)}{n_{III}^{U/Rn-SS}} = \frac{n_{II}^{net}(U/Rn)}{n_{II}^{U/Rn-SS}} = \frac{n_{IV}^{net}(U/Rn)}{n_{IV}^{U/Rn-SS}}.$$

6-6

Please note that Eq. 6-6 contains a term for interval *II* which may be used for corrections of minor contributions of U/Rn in interval *II*.

Then, the net CR of ^{40}K in the interval *IV* is given by:

$$n_{IV}^{net}(^{40}\text{K}) = n_{IV} - f_c n_{IV}^{twk} - f C_{Th} n_{IV}^{Th-SS} - C_{U/Rn} f n_{IV}^{U/Rn-SS}.$$

6-7

Finally, an effective potassium (^{40}K) concentration, C_K , can be obtained using the net CR of ^{40}K in interval *IV*, $n_{IV}^{net}(K)$, and the CR per Bq/l of the standard spectrum of K (K_{SS}) in interval *IV* normalized by the *f*-factor:

$$C_K f = \frac{n_{IV}^{net}(K)}{n_{IV}^{K-SS}}.$$

6-8

The detector calibration factor, *f*, can be determined using Eq. 6-8 by measuring for a well-defined K concentration, C_k , as discussed in section 6.4 below.

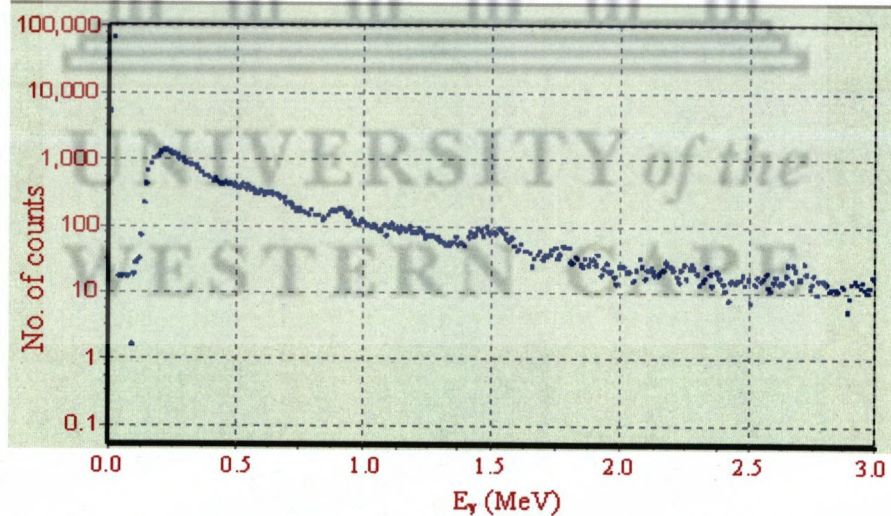


Figure 6-3: A cosmic-ray spectrum measured on 21 Nov. 2002 using the MEDUSA detector lowered below the water-surface of Theewaterskloof (Twk) dam, which is situated near Villiersdorp about 60 km from iThemba LABS. The activity on the y-axis is the number of counts obtained in 76 minutes. The small peaks seen in the spectrum are minor contributions of Th and K present in the detector, its associated electronics, and housing.

6.4 The KCl measurements

In this section, the detector efficiency will be established for the drum and the tank geometries. The drum and the tank were filled with tap water and the efficiency was determined by measuring the detector response after dissolving various quantities of KCl. Then, the measured ^{40}K count rates were compared to the ^{40}K count rates based on the KCl concentration in the vessel. Initially, the measurements were carried out at position P1 (see section 6.2). After it was noticed that the background CR at P1 varied significantly with time (as discussed in section 6.6), it was decided to move the set-up to position P2. Only measurements at P2 will be presented in this section.

6.4.1 The MEDUSA-drum KCl measurements

The ^{40}K calibration measurements were carried out by dissolving potassium chloride (KCl) salt of masses 1 kg, 2 kg, 4 kg and 6 kg in the drum filled with the tap water and then measuring the detector response for half an hour each. The KCl salt was first mixed in a bucket and then mixed further inside the drum using a stick. For each measurement, two subsamples were collected in Marinelli beakers and measured on the HPGe detector. Table 6-1 shows nominal KCl masses, the calculated ^{40}K concentrations (see intermezzo 6.1) and those concentrations obtained by measuring the sub-samples using the HPGe detector. One can see fairly good agreement between the ^{40}K activity concentrations measured by the HPGe detector with their calculated counterparts.

For the measurements with the MEDUSA detector, Table 6-2 presents the measurement description with nominal added masses of KCl, the gross and net CR (cps) in the energy interval 0.4 – 1.6 MeV, the effective contribution factor of cosmics, and the effective Th and U/Rn concentrations C_{Th} and $C_{\text{U/Rn}}$, respectively. We would like to point out that in this part of KCl measurements analysis; the energy range 0.4 – 1.6 MeV was used instead of interval IV so as to improve the statistics. The net CR in Table 6-2 is the CR corrected for “cosmics”, Th and U/Rn background contributions. The cosmics in this interval was $n_{\text{IV}}^{\text{Twk}} = 4.89(3)$ cps, whereas the CR per Bq/l for the standard spectra were as follows: $n_{\text{IV}}^{\text{Th-SS}} = 1.46(3)$ cps/(Bq/l), $n_{\text{IV}}^{\text{U/Rn-SS}} = 1.23(3)$ cps/(Bq/l) and $n_{\text{IV}}^{\text{K-SS}} = 0.265(6)$ cps/(Bq/l). The Th and U/Rn corrections involve the MEDUSA-drum efficiency calibration factor, f_{drum} . This requires an iterative procedure. The actual values are based on the value $f_{\text{drum}} = 0.455 \pm 0.019$ as derived below.

Table 6-1: The ^{40}K -activity concentrations for various quantities of KCl (containing 1.133% impurities) dissolved in the drum filled with tap water (volume $\sim 215 \pm 5$ l) measured in samples and calculated from the mass and the volume.

Nominal KCl mass (kg)	HPGe derived ^{40}K Conc. (Bq/l)	^{40}K Calculated Conc. (Bq/l)
1	80 ± 3	75.5 ± 1.9
2	147 ± 7	150 ± 2
4	291 ± 12	300 ± 4
6	428 ± 16	450 ± 6

Table 6-2: The MEDUSA-drum gross and net count rate in the interval (0.4 – 1.6 MeV) for the added KCl masses and tap water only (TW). The last three columns present the cosmic contribution factor and the Th and U/Rn effective concentrations.

Description	Gross count rate (cps)	net count rate (cps)	f_c	C_{Th} (Bq/l)	$C_{\text{U/Rn}}$ (Bq/l)
16-05-2007: 0 kg (TW)	20.92(4)	6.4(9)	0.84(6)	4.1(3)	3.8(6)
14-06-2007: 0 kg (TW)	15.02(6)	4.0(8)	0.88(8)	2.4(2)	2.7(5)
11-07-2007: 0 kg (TW)	15.09(3)	3.9(7)	0.91(6)	2.5(2)	2.6(4)
14-06-2007: 1 kg	24.01(8)	13.0(8)	0.81(7)	2.6(2)	2.6(5)
16-05-2007: 2kg	38.69(15)	23.6(1.1)	0.69(9)	4.2(4)	4.6(7)
16-05-2007: 4kg	56.24(18)	41.3(1.2)	1.00(11)	4.0(4)	3.5(7)
16-05-2007: 6 kg	74.3(2)	59.1(1.2)	0.88(10)	3.9(4)	4.3(7)

Figure 6-4 represents the ^{40}K net CR as a function of the amount of KCl added to the drum. The solid line in Figure 6-4 represents the best fit to the data obtained with a least squares analysis, with a reduced chi-square value of 0.4. The slope of the fitted line corresponds to the mean CR per mass ($n_{IV}^{net}(K) = 9.14 \pm 0.18$ cps/kg) and the intercept (4.5 ± 0.4 cps) is the ^{40}K CR in water without KCl salt added (background ^{40}K). The intercept agrees well with the weighted average of the tap-water (TW) spectra being 4.5 ± 0.4 cps. The radioactivity of one kg of KCl amounts to $(1.625 \pm 0.018) \times 10^4$ Bq (see intermezzo 6.1). For volume of the drum, 215 ± 5 l, this leads to a concentration of $C_K = 75.5 \pm 1.9$ Bq/l kg^{-1} . So, a slope value of 9.14 ± 0.18 cps/kg KCl corresponds to: $n_{IV}^{net}(K) / C_K = 0.121 \pm 0.006$ cps/(Bq/l). The expected value from the standard spectrum for this interval: $n_{IV}^{K-SS} = 0.265(6)$ cps/(Bq/l) leads to, using Eq. 6-8, an efficiency calibration factor of $f_{drum} = 0.455 \pm 0.019$.

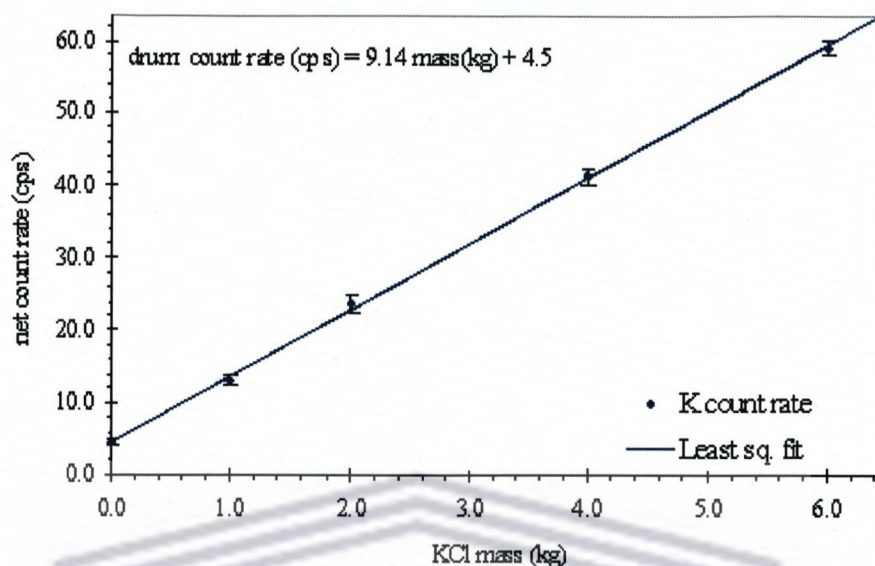


Figure 6-4: ^{40}K count rate (CR) in the interval 0.4 – 1.6 MeV (measured using the MEDUSA-drum set-up) versus the added KCl. The solid line represents the least squares fit with reduced chi-square value of 0.4. The slope of the fitted line represents the weighted average CR per mass (cps/kg) and the intercept is the background CR of ^{40}K .

Intermezzo 6.1: Relation between mass and activity for KCl.

- 1 kg KCl corresponds to $13.4136 \text{ mol} \left(\frac{1000 \text{ g}}{74.551 \text{ g} \cdot \text{mol}^{-1}} \right)$ of KCl.
- 13.4 mol KCl is equivalent to about 8.08×10^{24} atoms of KCl and therefore 8.08×10^{24} atoms of K.
- The above number of K atoms contains $0.0117 \pm 0.0001 \%$ atoms of ^{40}K [Lide, 1997]. This implies that $8.08 \times 10^{24} \times 1.17 \times 10^{-4} = 9.45 \times 10^{20}$ atoms of ^{40}K .
- The KCl used for this work¹⁴ was packed in containers of 500 g KCl and has impurities of: 0.1% Bromide (Br), 1.0 % loss on drying, 0.03 % Sulphate (SO_4), 0.001% heavy metals (such as Pb) and 0.002% iron (Fe). This amounts to total impurities of 1.133%. This means that each 1 kg KCl contains 11.33 g impurities. By assuming 0.005 g precision on the impurities mass i.e. $11.330 \pm 0.005 \text{ g}$, we get a relative uncertainty of **0.04%**.
- We weighed 5 masses of KCl of 5 kg each on a scale of precision 0.0002 kg. The average was found to be $5.0479 \pm 0.0109 \text{ kg}$. This gives a relative uncertainty of **0.22%**.

¹⁴ The KCl was purchased from: Merck Chemicals (PTY) LTD. UNIVAR® potassium chloride. Saarchem, 259 Davidson Rd, Wadeville, Gauteng, South Africa.

- $Activity = \lambda \cdot N = \frac{\ln 2}{T_{1/2}} \cdot N$. For the above number of ^{40}K nuclei, the activity was calculated to be $(1.625 \pm 0.018) \times 10^4$ Bq, with $T_{1/2} (^{40}\text{K}) = (1.277 \pm 0.008) \times 10^9$ years [Firestone, 1998].
- The volume of the water in the tank = 1170 ± 10 l and is equivalent to about 1.17×10^3 kg of water.
- Thus adding 1kg KCl to the tank, the concentration increased by $\left(\frac{1.6 \times 10^4 \text{ Bq}}{1.2 \times 10^3 \text{ l}_{\text{H}_2\text{O}}}\right) = 13.91 \pm 0.19$ Bq ^{40}K per $\text{l}_{\text{H}_2\text{O}}$.

6.4.2 The MEDUSA-tank KCl measurements

KCl salt, in 500 g batches, was weighed (scale precision was 0.2 g) and each of 10 batches (5 kg) was first dissolved in a bucket and then mixed further in the tank, filled with tap water, using a long stick. This was repeated five times (up to a final mass of 25 kg). For the subsequent KCl batches, the water was taken from the KCl solution in the tank. In addition, for each measurement (5 kg batches), two subsamples were taken in Marinelli beakers and measured on the HPGe detector. The two subsamples were taken: one from the top of the tank (directly through the upper opening) and the other from a valve at the bottom of the tank. Table 6-3 presents the weighed KCl masses, the measured and calculated activity concentration of ^{40}K for each filling. The good agreement between the calculated and the measured ^{40}K activity concentrations indicates that there are no significant systematic uncertainties introduced by the process of mixing the KCl or of taking sub-samples for the HPGe measurements.

Table 6-4 presents the MEDUSA measurement description with added masses of KCl, the gross and net CR (cps) in the energy interval 0.4 – 1.6 MeV, the effective contribution factor of cosmics, and the effective Th and U/Rn concentrations C_{Th} and $C_{\text{U/Rn}}$, respectively. It can be seen from Table 6-4 that the cosmics and Th contributions are rather constant but U fluctuates quite a bit, most likely due to background radon in air. This background effect will be discussed in section 6.6.

The CR per Bq/l in the energy interval 0.4 – 1.6 MeV for the standard spectra were as follows: $n_{\text{IV}}^{\text{Th-SS}} = 1.541(15)$ cps/(Bq/l), $n_{\text{IV}}^{\text{U/Rn-SS}} = 1.312(14)$ cps/(Bq/l) and $n_{\text{IV}}^{\text{K-SS}} = 0.243(6)$ cps/(Bq/l). In a similar way as described in subsection 6.4.1, the Th and U/Rn

corrections involve the efficiency calibration factor, f_{tank} obtained by an iterative procedure based on the value $f_{tank} = 0.551 \pm 0.018$ as derived below.

Table 6-3: KCl salt (containing 1.133% impurities) weighed (precision of scale was 0.2 g) and dissolved in the tank filled with tap water; the corresponding radioactivity concentrations of ^{40}K in the solution, which was measured with the HPGe detector, and the ^{40}K activity concentration calculated based on the KCl masses and the volume.

KCl mass (kg)	HPGe derived ^{40}K Conc. (Bq/l)	Calculated ^{40}K Conc. (Bq/l)
5.051	68 ± 4	69.6 ± 1.0
10.108	140 ± 7	139.2 ± 1.9
15.167	216 ± 9	209 ± 3
20.205	271 ± 10	278 ± 4
25.24	342 ± 12	348 ± 5

Table 6-4: The MEDUSA-tank gross and net CR in the energy interval (0.4 – 1.6 MeV) for five KCl spectra and two tap-water (TW) spectra. The effective contribution factor of cosmics, f_c , and the effective concentrations C_{Th} and $C_{U/Rn}$ are presented in the last three columns.

Description	Gross count rate (cps)	net count rate (cps)	f_c	C_{Th} (Bq/l)	$C_{U/Rn}$ (Bq/l)
TW_2h: 0 kg (KCl)	9.52(4)	0.3(6)	0.90(7)	0.73(11)	2.8(3)
TW_5h: 0 kg (KCl)	9.30(2)	0.8(5)	0.90(6)	0.77(09)	2.2(3)
5.051 kg(KCl)	17.34(5)	10.5(6)	1.00(7)	0.65(11)	0.7(3)
10.108 kg(KCl)	26.91(6)	19.9(6)	0.96(7)	0.72(11)	0.9(3)
15.167 kg(KCl)	36.37(7)	29.2(5)	0.89(7)	0.85(11)	1.1(3)
20.205 kg(KCl)	45.55(8)	38.6(6)	0.92(7)	0.77(11)	0.9(3)
25.24 kg(KCl)	55.01(9)	47.6(5)	0.90(7)	0.85(11)	1.3(3)

Similar to the drum, the measured ^{40}K net CRs are plotted as a function of the amount of KCl added to the tank (Figure 6-5). The solid line in Figure 6-5 represents the best fit to the data obtained with a least squares analysis, with $\chi^2_R = 0.3$. The slope of the fitted line corresponds to the mean CR per mass ($n_{IV}^{net}(K) = 1.87 \pm 0.02$ cps/kg) and the intercept (0.8 ± 0.3 cps) is the ^{40}K CR in water without KCl salt added (background ^{40}K). The intercept agrees well with the weighted average of the TW-spectra being 0.6 ± 0.4 cps. Moreover, one notices that this average background CR, 0.6 ± 0.4 cps, is an order of magnitude less than the average background CR (4.5 ± 0.5 cps) of the drum. This significant shielding of background is most likely due to the bigger volume of the tank as compared to the drum.

As for the drum, the radioactivity of one kg of KCl (1.625 ± 0.018) $\times 10^4$ Bq and the volume of the tank (1170 ± 10 l) leads to a KCl activity concentration of 13.91 ± 0.19 Bq/l (see intermezzo 6.1). So, a slope value of 1.87 ± 0.02 cps/kg KCl corresponds to $n_{IV}^{net}(K) / C_K = 0.134 \pm 0.006$ cps/(Bq/l). The expected value from the standard spectrum

for this interval: $n_{IV}^{K-SS} = 0.234(6)$ cps/(Bq/l) leads to, again by using Eq. 6-8, an efficiency calibration factor of $f_{tank} = 0.551 \pm 0.018$.

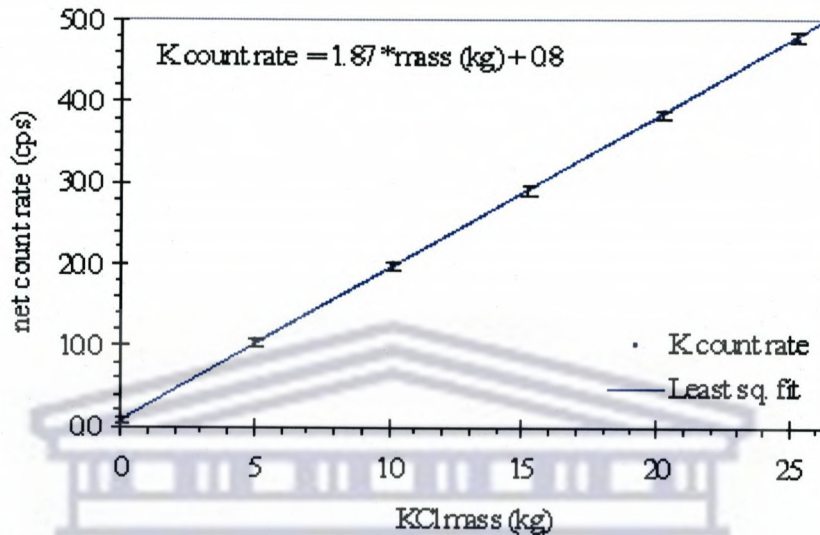


Figure 6-5: The relation between the net CR of ^{40}K in the interval 0.4 – 1.6 MeV and the added KCl. The solid line represents the least squares fit with reduced chi-square value of 0.3. The slope represents the mean cps/kg and the intercept is the background ^{40}K count rate (cps).

6.5 The ^{222}Rn measurements

For the radon measurements, the drum and the tank were filled with water from the borehole at iThemba LABS (see CHAPTER 4, section 4.3). This water has a time-dependent radon concentration as found out from the analysis on the HPGe detector. For the drum, the various radon in-water concentrations were obtained by mixing borehole water (rich in radon ~ 30 Bq/l) with tap water (no radon). However, this procedure of mixing did not work with the tank most likely due to the big volume of the tank and the density difference between the high salinity and the relatively high temperature of the borehole water as compared to that of the tap water. Instead, the tank was filled with borehole water only and the concentrations were measured everyday as the radon decays.

This section presents the results of in-field concentration measurements of radon in-water by introducing a MEDUSA detector into either a drum or a tank. This task will be achieved by establishing correlation between the count rate extracted from MEDUSA measurements and the corresponding radon concentration of measurements carried out in the laboratory using the HPGe detector and Marinelli beakers. The HPGe method for

measuring radon in-water has been optimized in a previous study (see CHAPTER 4) and therefore will be used as a reference method.

6.5.1 The MEDUSA-drum ^{222}Rn measurements

Table 6-5 presents the gross and net CRs of the U/Rn (in interval III) for four borehole-water spectra and two tap-water spectra. The cosmics in this interval was $n_{III}^{Twk} = 0.513(11)$ cps while the CR per Bq/l for the standard spectra were as follows: $n_{III}^{Th-SS} = 0.156(9)$ cps/(Bq/l) and $n_{III}^{U/Rn-SS} = 0.132(9)$ cps/(Bq/l). In column 3 of the table, the net CRs were obtained by subtracting the cosmics and Th contributions as described in section 6.3. The effective Th contribution, C_{Th} , was obtained using the weighted average $n_{II}^{net}(Th)$ of the two tap-water spectra and determined to be 2.42 ± 0.19 (Bq/l). The reason for taking the Th contribution from the tap-water measurements is because in the borehole water spectra, interval II is expected to be significantly influenced by contribution from U/Rn. The net CRs of the borehole-water measurements were corrected further in column 4 for radon decay since the time of sampling. One can see that in Table 6-5 the net CR for the two tap-water measurement agreed within uncertainties despite the one month difference between their times of measurement.

The decay corrected net CRs (column 4 of Table 6-5), were converted to radon concentrations using the normalized standard spectrum value: $n_{III}^{U/Rn-SS} = 0.132(9)$ cps/(Bq/l). Next these radon concentrations were plotted against their counterparts measured with the HPGe as shown in Figure 6-6. From the least squares best fit (solid line) of the data, the intercept and slope were found to be 2.3 ± 0.3 Bq/l and 0.86 ± 0.03 (Bq/l)/(Bq/l), respectively. The reduced chi-square value of the fit is 0.6. The intercept value 2.3 ± 0.3 Bq/l presumably represents the radon concentration in the tap water as measured by the MEDUSA detector. However, since the radon concentration in this tap water was measured using the HPGe detector to be 0.30 ± 0.10 Bq/l, the MEDUSA value 2.3 ± 0.3 Bq/l is most likely due to γ -rays originating from U/Rn in air and in soil surrounding the measurement location.

Table 6-5: Gross CR in interval III (U/Rn) for the various spectra measured in the drum. In column 3, the net CR was obtained by subtracting the cosmic and Th contributions. The CR was corrected further in column 4 for radon decay. The effective contribution factor of cosmic is presented in column 5.

Description	Gross count rate (cps)	Net count rate (cps)	Decay corr. Net count rate (cps)	f_c
14-6-2007:m6-7	3.95(3)	3.10(7)	3.17(8)	0.92(8)
19-6-2007:m7-8	2.24(2)	1.43(6)	1.46(7)	0.85(8)
20-6-2007:m6-7	3.18(3)	2.33(6)	2.39(8)	0.91(8)
20-6-2007:m13-14	4.35(3)	3.48(7)	3.56(8)	0.96(8)
14-6-2007: TW	1.175(18)	0.35(6)	Wt. av. of TW spectra: 0.35(4)	0.88(8)
11-7-2007: TW	1.192(10)	0.35(5)		0.91(6)

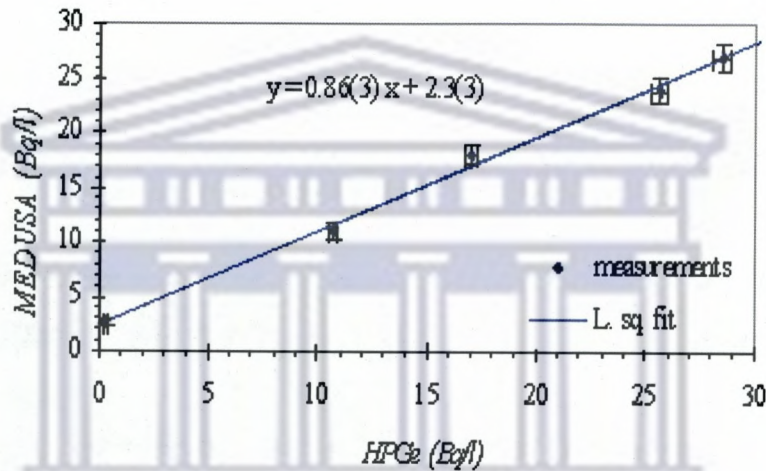


Figure 6-6: The MEDUSA-drum field measurement of U/Rn (interval III) in borehole water, of various radon concentrations, and tap water, versus the radon concentrations determined by the HPGe detector in the lab. The solid line represents the least squares fit of the data with reduced chi-square value of 0.6. The slope of the fitted line represents correspondence between the MEDUSA and the HPGe Rn concentration whereas the intercept is the U/Rn background.

The minimum detectable activity (MDA) of the MEDUSA detector in the geometry of the 210-liter drum was estimated from the CR in the U/Rn interval (III) of the Theewaterskloof background spectrum: 0.513 cps, which was measured for a time $T_{Twk} = 1.3$ hrs. Rewriting Eq. 2-8 after replacing the f_d factor with the relevant MEDUSA parameters, gives:

$$MDA(Bq/l) = \frac{2.7 + 3.3\sqrt{T_m n_{III}^{T_{Twk}} (1 + T_m / T_{Twk})}}{T_m n_{III}^{U/Rn-SS}}, \quad 6-9$$

where T_m is the measurement time. For $T_m = 0.5$ hour and substituting the values of all factors in Eq. 6-9, the MDA was estimated to be 0.6 Bq/l for the MEDUSA-drum geometry. In principle, the statistical uncertainty leading to the MDA can be further reduced by a longer measuring time of the “background” spectrum.

6.5.2 The MEDUSA-tank ^{222}Rn measurements

The MEDUSA measurements and the HPGe samples were synchronized to reference measurement times. One MEDUSA measurement and one HPGe sample were taken per day for 13 days. The MEDUSA detector was not removed from the tank throughout the period of measurements. The tank radon measurements were analyzed in a similar way to those of the drum. Table 6-6 shows the spectrum ID, date/time of the start of the measurement, the gross and net CR of interval III (U/Rn) for the 13 MEDUSA measured γ -ray spectra of borehole water (of various radon concentrations) and for two spectra of tap-water. The net CR represents the CR after subtracting the cosmics and Th contribution using the f_c factor (presented in column 4) and $C_{\text{Th}} = 0.50 \pm 0.05$ Bq/l determined using the weighted average CR, $n_{\text{II}}^{\text{net}}(\text{Th})$, of the two tap-water measurements. The cosmics remains the same as in the drum analysis: $n_{\text{III}}^{\text{Twk}} = 0.513(11)$ cps whereas the CR per Bq/l for the standard spectra were as follows: $n_{\text{III}}^{\text{Th-SS}} = 0.195(5)$ cps/(Bq/l) and $n_{\text{III}}^{\text{U/Rn-SS}} = 0.153(5)$ cps/(Bq/l). The 5th column of Table 6-6 presents net CR after correction for radon decay and subtracting the supported radon. The radon radioactive decay correction includes decay during measurements and that between reference measurement time and the time that the measurement started. The decay during measurement was corrected using Eq. 4-1. The supported radon was corrected for by using the equilibrium radon in-growth value: $C_{\text{eq}}^{\text{Rn}} = 0.82 \pm 0.04$ Bq/l for the iThemba LABS borehole as described in CHAPTER 4 (subsection 4.4.2.2). For the MEDUSA measurements, this latter value was converted to count rate using the U/Rn_SS value: $n_{\text{III}}^{\text{U/Rn-SS}} = 0.153 \pm 0.006$ cps/(Bq/l). The conversion leads to $C_{\text{eq}}^{\text{Rn}} = 0.125 \pm 0.007$ cps for the MEDUSA measurements. To account for the radon build-up of the supported radon in the borehole water after elapsed time (t_e), the build-up relation: $C_{\text{sup}}^{\text{Rn}} = C_{\text{eq}}^{\text{Rn}} (1 - e^{-\lambda t_e})$ was utilized to obtain the supported radon corresponding to each measurement where λ is the radon decay constant.

Table 6-6: Spectra ID, date/time measurement started and the corresponding gross and net CR in the energy interval III (U/Rn) for the MEDUSA-tank geometry. The net CR was corrected by subtracting the cosmics and Th contributions. In column 4, the net CR was corrected further for the radon radioactive decay and then subtracting supported Rn¹⁵. The effective contribution factor from cosmics is presented in column 5 whereas the Th effective contribution, C_{Th} , for all measurements was determined using the weighted average CR, n_{II}^{net} , of the tap-water measurements and found to be 0.50 ± 0.05 Bq/l.

spectrum ID	Date/time of measurement	Gross CR (cps)	Net CR (cps)	Net CR corr. for Rn decay and supp. Rn (cps)	f_c
tank-Rn-m4-6	13/09/08 21:02	6.22(2)	5.59(5)	5.79(5)	1.02(7)
tank-Rn-m25-27	14/09/08 18:02	5.14(2)	4.56(4)	4.63(4)	0.93(6)
tank-Rn-m49-51	15/09/08 18:02	4.29(2)	3.71(4)	3.75(4)	0.93(6)
tank-Rn-m73-75	16/09/08 18:02	3.580(18)	3.00(4)	3.01(4)	0.93(6)
Rn-decay-m1-3	17/09/08 18:32	3.031(17)	2.47(4)	2.46(4)	0.90(6)
Rn-decay-m25-27	18/09/08 18:32	2.539(15)	2.00(4)	1.97(4)	0.85(6)
Rn-decay-m7-9	19/09/08 18:02	2.244(14)	1.70(4)	1.64(4)	0.87(6)
Rn-decay-m31-33	20/09/08 18:02	1.935(13)	1.41(4)	1.36(4)	0.83(6)
Rn-decay-m55-57	21/09/08 18:02	1.696(13)	1.15(4)	1.08(4)	0.87(6)
Rn-decay-m75-77	22/09/08 14:02	1.473(12)	0.94(4)	0.85(4)	0.84(6)
Rn-decay-m1-4	23/09/08 09:44	1.352(10)	0.80(3)	0.72(4)	0.88(6)
Rn-decay-m1-4	24/09/08 09:24	1.173(9)	0.68(3)	0.58(3)	0.78(5)
Rn-decay-2_m1-4	25/09/08 11:48	1.059(9)	0.54(3)	0.44(3)	0.82(5)
TW-10cm-m1-6	11/09/08 11:02	0.563(6)	0.06(3)	Wt. av. of TW. = 0.09±0.02	0.80(5)
TW-10cm_2-m1-8	12/09/08 22:55	0.650(5)	0.13(3)		0.83(5)

The radon corrected CR measured by the MEDUSA detector in the tank for the 13 borehole-water measurements and their corresponding unsupported radon concentrations measured using the HPGe detector were plotted against the time elapsed since the time that the tank was sealed. Figure 6-7 shows the HPGe and the MEDUSA data fitted with an exponential decay model: $y(t) = a + C_0 e^{-\lambda t}$ represented by solid and dashed lines. The values of 'a' were estimated to be -0.01 ± 0.18 cps and -1.6 ± 1.0 Bq/l for the MEDUSA and the HPGe measurements, respectively. These latter values are not statistically different from zero. From the exponential fit, the effective decay constants were found to be 0.0072 ± 0.0005 and 0.0089 ± 0.0002 h⁻¹ for the HPGe and the MEDUSA measurements, respectively. It can be seen that the HPGe effective decay constant agreed within uncertainties with the known value of the radon decay constant, 0.0076 h⁻¹, whereas the MEDUSA measured radon decays faster by about 17%. The faster decay of radon could be attributed to radon loss in the tank during the MEDUSA measurements. The radon loss is supported by our physical inspection of the MEDUSA

¹⁵ The radon radioactive decay correction includes decay during measurements and that between reference measurement time and the time that the measurement started. Supported radon was corrected by using the relation: $C_{sup}^{Rn} = C_{eq}^{Rn} (1 - e^{-\lambda t_e})$ as explained in the text.

mounting on the tank, which is less radon-tight as compared to the drum. Consequently, the radon present in tank water effectively decays away faster. Moreover, one notices that in Figure 6-7, the two decay curves associated with the HPGe and the MEDUSA measurements converge as radon concentration decreases with time. This convergence may be attributed to the fact that there is less radon-loss from the tank as the radon concentration in the water approaches the equilibrium determined by the Oswald partition coefficient described in CHAPTER 2 (subsection 2.6.2).

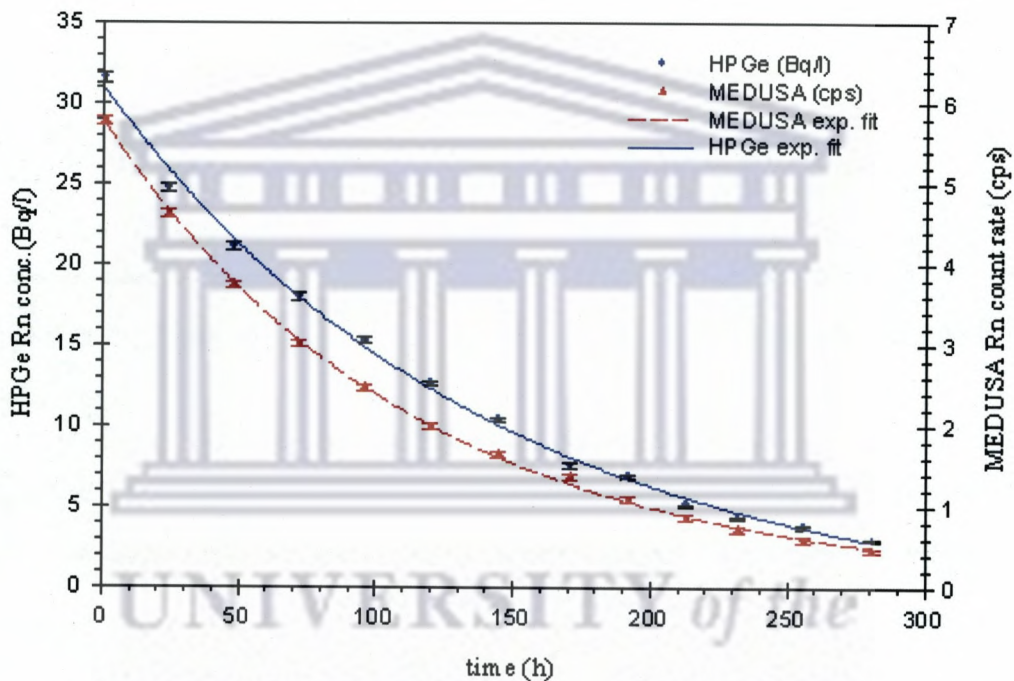


Figure 6-7: Radon-in-water concentration (Bq/l) and count rate (cps) measured by the HPGe detector (left y-axis) and the MEDUSA-tank set-up (right y-axis), respectively, versus the elapsed decay time. From an exponential decay fit (model: $y = a + C_0 e^{-\lambda t}$), the effective decay constant derived by the HPGe measurements was found to be $0.0072 \pm 0.0005 \text{ h}^{-1}$ while that of the MEDUSA was found to be $0.0089 \pm 0.0002 \text{ h}^{-1}$.

The MEDUSA unsupported radon concentration was obtained by dividing the corrected net CR by $n_{III}^{U/Rn-SS} = 0.153(5) \text{ cps}/(\text{Bq/l})$. Next, the obtained MEDUSA radon concentrations were plotted against their corresponding unsupported radon concentrations (Bq/l) measured using the HPGe detector as shown in Figure 6-8. From the least square fit (solid line of Figure 6-8), the slope was found to be $1.10 \pm 0.03 \text{ (Bq/l)/(Bq/l)}$, the intercept = $-0.01 \pm 0.18 \text{ (Bq/l)}$, and the reduced chi-square value of the fit was 2.3. This slightly higher value of chi-square may reflect some systematic effects, as can also be seen from Figure 6-7, most likely due to elevated Rn in air (whose

associated γ -rays reach the detector from the top, which will be discussed in section 6.7) that significantly contribute to measurements of the MEDUSA-tank. In addition, it can be seen from Figure 6-8 that the intercept is not statistically different from zero. Unlike the high value of the intercept (2.3 ± 0.3 Bq/l) in the case of the drum, the zero intercept may imply that most of the U/Rn γ -rays originating from the soil were better shielded by the tank-water surrounding the detector (see also the Table 6-13 and its discussion in section 6.7).

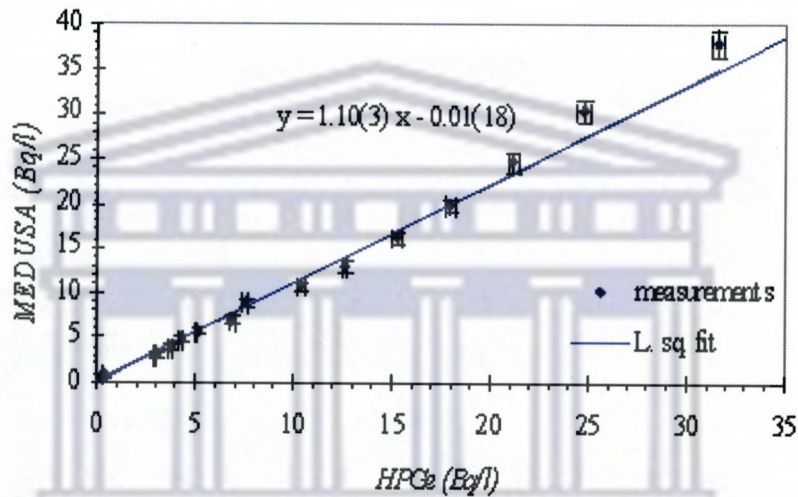


Figure 6-8: MEDUSA-tank derived-U/Rn concentration of borehole water, of various radon concentrations, and tap water (measured in the field) versus the radon concentrations determined by the HPGe detector in the lab. The solid line represents the least squares fit of reduced chi-square value 2.3.

The MDA of the MEDUSA detector in the geometry of the 1000-liter tank was estimated in a similar way to that of the drum using the $n_{III}^{T_{wk}} = 0.513(11)$ cps and utilizing Eq. 6-9 where for the tank $n_{III}^{U/Rn-SS} = 0.153(5)$ cps/(Bq/l). Thus, the MDA was estimated to be 0.4 Bq/l for a measurement time of half an hour.

In comparison of the two geometries (the MEDUSA-drum and MEDUSA-tank), the drum has the advantage of being lighter in weight and easier to move for the field measurements and that the MEDUSA detector can be mounted on the drum in a more radon-tight way. These advantages may offset the disadvantage that the MDA of the drum is higher (by about 33%) than that of the tank. The MEDUSA-tank geometry has the advantage of relatively low MDA, 0.4 Bq/l, which makes the set-up more suitable for measuring water of low radon concentration in the field. However, the disadvantage will be the impracticality of transporting the present tank during field measurements.

Another concern in the case of the drum is the effect of local background radon as noticed from the intercept associated with the drum measurements.

6.6 Background investigations

One of the major challenges for field measurements is the shielding of the background γ -ray radiation. The main sources of these γ -rays are the cosmic rays and the γ -rays emitted from terrestrial radionuclides such as U, Th and K. The terrestrial radionuclides are present in the soil underneath and around the detector and in the buildings in the vicinity of the measurements location. Several measurements to investigate the background effect were carried out with the MEDUSA detector inserted into both the drum and the tank. The analyses of the background investigations were confined to the high-energy part of the spectrum: the energy interval 1.6 to 3.0 MeV. In the KCl measurements, the part of the spectrum above 1.6 MeV is merely background. Therefore, for the background investigations the KCl and the tap-water measurements will be considered.

In this section, the results of background investigation measurements using the MEDUSA detector introduced into the drum and into the tank will be discussed. The measurements were analyzed using the hybrid approach described in section 6.3.

6.6.1 The MEDUSA-drum background measurements

Table 6-7 shows the CR in each of the energy intervals described in section 6.3 for the four KCl spectra described in subsection 6.4.1; three spectra of tap-water that were measured on 16 May, 14 June and 11 July 2007; simulated and calibrated standard spectrum of thorium (Th_SS); spectrum of an empty drum, and the Theewaterskloof cosmic ray spectrum. From this Table one notices that the CRs are independent of KCl; count rate of interval *I* is independent of the time of measurement; count rate of intervals *II* and *III* depend on location while the CR of measurements at P1 (three KCl plus one tap-water spectra) are higher than those at P2 (two tap-water spectra and a KCl spectrum); count rates for all intervals are much lower than for the empty-drum.

These observations are supported by the acceptable values (between 0.7 and 2.7) of the reduced chi-square associated with the weighted averages CR for the four measurements at P1, $\chi_R^2(\text{of } 4)$, and the very high values (above 69), except interval *I*, for the seven measurements at P1 and P2 ($\chi_R^2(\text{of } 7)$). The CR of interval *I* (cosmic rays)

in the seven spectra is almost constant with a weighted average of 0.0595 ± 0.0012 cps and χ_r^2 (of 7) of 1.7. The difference between the CR for the empty drum and the other water-filled drum measurements is due to the fact that water shields the detector from the surrounding radiation. The reduction is a factor of less than two for interval I, but ranges between two and three for the other intervals.

Table 6-7: MEDUSA-drum measured CR in the energy interval $1.6 < E_\gamma < 3.0$ MeV, subdivided over a number of intervals. The Table presents the CR in these intervals for seven spectra (four of KCl salt dissolved in tap water and three spectra of tap-water), a spectrum of an empty drum, the Twk cosmic ray spectrum and the Th standard spectrum. Also presented are the weighted averages CR and the associated chi-square values for the four spectra measured at P1 and for all seven spectra measured at P1 and P2.

Intervals in MeV description	1.6-1.85 III _a (cps)	1.85-2.4 III _b (cps)	2.4-2.75 II (cps)	2.75 -3.0 I (cps)	1.6 -3.0 Total (cps)
16-05-2007: TW; P1	0.685(7) ¹⁶	0.862(8)	0.547(7)	0.058(2)	2.15(13)
16-05-2007: 2kg KCl; P1	0.72(2)	0.89(2)	0.543(18)	0.048(5)	2.20(4)
16-05-2007: 4kg KCl; P1	0.71(2)	0.89(2)	0.571(18)	0.069(6)	2.24(4)
16-05-2007: 6 kg KCl; P1	0.70(2)	0.92(2)	0.540(17)	0.061(6)	2.22(4)
14-06-2007: TW; P2	0.517(12)	0.657(14)	0.379(10)	0.060(4)	1.61(2)
14-06-2007: 1 kg KCl; P2	0.537(12)	0.630(13)	0.395(11)	0.056(4)	1.62(2)
11-07-2007: TW; P2	0.532(6)	0.660(7)	0.394(5)	0.063(2)	1.649(11)
Wt. Av. (of 4)	0.692(6)	0.873(7)	0.548(6)	0.058(2)	2.172(11)
χ_r^2 (of 4)	1.1	2.3	0.7	2.4	2.7
Wt. Av. (of 7)	0.596(4)	0.742(4)	0.453(3)	0.0595(12)	1.852(7)
χ_r^2 (of 7)	69	101	83	1.7	239
24-05-2007: Empty drum	1.86(5)	2.00(5)	1.52(4)	0.095(10)	5.47(8)
21-11-2002: Cosmics (Twk)	0.234(7)	0.280(8)	0.145(6)	0.069(4)	0.728(13)
Th_SS	0.055(6)	0.102(8)	0.107(8)	0.0003(4)	0.264(12)

In Table 6-8, the CR of the intervals are corrected by subtracting the cosmics contribution from the seven spectra and from the empty drum spectrum. From a comparison of the data listed in Table 6-8, one notices that the values at P1 are about 1.5 times higher than at P2 for all energy intervals. The high chi-square values associated with the weighted averages CR of the seven spectra is most likely due to this difference in background CR at the two locations.

¹⁶ Values in brackets are 1σ statistical uncertainties.

Table 6-8: Cosmics corrected CR, of the MEDUSA-drum measurements, in the various energy intervals listed in Table 6-7 and the corresponding weighted averages CR and the associated chi-square values.

Intervals in MeV description	1.6-1.85 III _a (cps)	1.85-2.4 III _b (cps)	2.4-2.75 II (cps)	1.6 -3.0 Total (cps)
16-05-2007: TW; P1	0.49(2)	0.63(2)	0.425(12)	1.54(4)
16-05-2007: 2kg KCl; P1	0.56(3)	0.69(3)	0.44(2)	1.69(7)
16-05-2007: 4kg KCl; P1	0.47(3)	0.61(4)	0.43(2)	1.51(9)
16-05-2007: 6 kg KCl; P1	0.49(3)	0.67(4)	0.41(2)	1.58(8)
14-06-2007: TW; P2	0.31(2)	0.41(3)	0.25(2)	0.98(6)
14-06-2007: 1 kg KCl; P2	0.35(2)	0.40(3)	0.28(2)	1.03(6)
11-07-2007: TW; P2	0.32(2)	0.41(2)	0.262(12)	0.99(5)
Wt. Av. (of 4)	0.499(12)	0.643(14)	0.426(9)	1.57(3)
χ^2 (of 4)	1.7	1.5	0.3	1.3
Wt. Av. (of 7)	0.408(8)	0.520(10)	0.338(6)	1.28(2)
χ^2 (of 7)	19.3	25.5	31.6	28.3
24-05-2007: Empty drum	1.54(6)	1.61(7)	1.32(5)	4.47(15)

A further correction was made to the CR in the radon intervals by subtracting the thorium contribution. The results of the latter corrections are presented in Table 6-9. Table 6-9 also shows the CR in the intervals III_a, III_b, and III for the simulated and calibrated standard spectrum of U/Rn (U/Rn_{SS}), which corresponds to one Bq/l radon in water. After subtracting the thorium contribution (Table 6-9), there is hardly any variation in the terrestrial background (U/Rn) over one day (May measurements). The Th also shows no changes in the same period. However, the ratio between the terrestrial radiation CR at the locations P1 and P2 remains about 1.5. From the values of the U/Rn standard spectrum (Table 6-9), this change in CR for the U/Rn intervals corresponds to a maximum change of 2.0 Bq/l Rn in the water if this change is due to radon dissolved in the water in the drum. This change is also reflected in the slightly higher values of χ^2 (of 7) for the Rn intervals. It can also be noted from the data in Table 6-9 that the CR of interval III equals the sum of its subintervals III_a and III_b, and that the CR of the total interval (1.6 – 3.0 MeV) is approximately equal the CR in the various regions. Hence, the subintervals of III can be combined. Moreover, the noticeable drop of the χ^2 (of 7) values after subtracting the Th contribution suggests that the effect of the background Th (with its strong peak 2.6 MeV) dominates the small changes of background Rn (interval III) at the two locations, P1 and P2.

Table 6-9: The cosmics corrected CR measured with the MEDUSA-drum in Table 6-8, are corrected for thorium contribution. The correction was applied to the water-filled as well as to the empty drum spectra. Also presented are the weighted averages of CR and their associated chi-square values for the various intervals.

Intervals in MeV description	1.6-1.85 III _a (cps)	1.85-2.4 III _b (cps)	1.6-2.4 III (cps)	1.6-3.0 Total (cps)
16-05-2007: Tap-water; P1	0.27(3)	0.22(5)	0.49(7)	0.49(10)
16-05-2007: 2kg KCl; P1	0.33(4)	0.27(6)	0.60(9)	0.60(13)
16-05-2007: 4kg KCl; P1	0.26(4)	0.20(6)	0.46(9)	0.46(14)
16-05-2007: 6 kg KCl; P1	0.28(4)	0.28(6)	0.56(9)	0.56(13)
14-06-2007: Tap-water; P2	0.18(3)	0.17(4)	0.36(6)	0.36(9)
14-06-2007: 1 kg KCl; P2	0.21(3)	0.14(4)	0.35(6)	0.34(9)
11-07-2007: Tap-water; P2	0.19(2)	0.16(3)	0.34(5)	0.34(8)
Wt. Av. (of 4)	0.284(19)	0.24(3)	0.53(4)	0.53(6)
χ^2_R (of 4)	0.6	0.4	0.6	0.3
Wt. Av. (of 7)	0.227(12)	0.190(17)	0.42(3)	0.42(4)
χ^2_R (of 7)	2.7	1.3	2.2	1.0
U/Rn_SS	0.092(7)	0.038(5)	0.132(9)	0.135(9)
24-05-2007 Empty drum	0.86(11)	0.36(15)	1.2(2)	1.2(3)

6.6.2 The MEDUSA-tank background measurements

Table 6-10 shows the CR in the various energy intervals for the five KCl spectra described in subsection 6.4.2; two spectra of tap-water (TW): TW_2h and TW_5h measured for two and five hours, respectively; a simulated standard spectrum of Th (Th_SS); spectrum of empty tank measured on 21 Aug. 2008. Also shown in the table are the weighted average CR of each interval for the five KCl spectra (Wt.Av.(5)) and Wt.Av.(7) for the five KCl plus the two tap-water spectra and the corresponding reduced chi-square values (χ^2_R (of 5) and χ^2_R (of 7)). A comparison between the spectrum for the empty tank and the other water-filled tank spectra shows that there is a reduction factor of less than 1.5 for interval I, but this factor ranges between three and five for the other intervals. This value for interval I is the same as for the drum. For the terrestrial radionuclides, the reduction in the tank-measured CR is twice that in the drum-measured CR. This shows that, in comparison with the drum, the detector shielding improves by a factor of two. The CR in the cosmics interval for the seven spectra is almost constant with a weighted average CR of 0.0633 ± 0.0010 cps and χ^2_R (of 7) of 1.0. Contrary to the cosmics, the CR of the terrestrial background in intervals III_a, III_b and the total interval for the two tap-water spectra are higher than their counterparts in the five KCl spectra, except for the Th interval, $2.40 < E_\gamma < 2.75$ MeV.

Table 6-10: MEDUSA-tank derived-CR in the energy interval $1.6 < E_\gamma < 3.0$ MeV subdivided over a number of intervals. The Table presents the CR in these intervals for: seven spectra (five of KCl salt dissolved in tap water and two spectra of tap-water), a spectrum of an empty tank, a simulated standard spectrum of Th (Th_SS) and the Twk cosmic ray spectrum. Also presented are the weighted averages CR and the associated chi-square values for the five KCl spectra and for the seven spectra (KCl plus the two tap-water spectra).

Intervals in MeV description	1.6-1.85 III _a (cps)	1.85-2.4 III _b (cps)	2.4-2.75 II (cps)	2.75 -3.0 I (cps)	1.6 -3.0 Total (cps)
23-04-2008: TW_5h	0.435(5)	0.460(5)	0.220(3)	0.062(2)	1.177(8)
24-04-2008: TW_2h	0.484(9)	0.485(9)	0.216(6)	0.062(3)	1.246(14)
24-04-2008: 5kg	0.307(7)	0.415(8)	0.221(6)	0.069(3)	1.012(12)
24-04-2008: 10 kg	0.318(7)	0.421(8)	0.225(6)	0.066(3)	1.030(12)
25-04-2008: 15 kg	0.340(7)	0.417(8)	0.229(6)	0.062(3)	1.047(12)
25-04-2008: 20 kg	0.333(7)	0.400(7)	0.225(6)	0.064(3)	1.021(12)
25-04-2008: 25 kg	0.363(7)	0.423(8)	0.230(6)	0.062(3)	1.078(12)
Wt. Av. (of 5)	0.331(3)	0.415(3)	0.226(3)	0.0644(13)	1.037(5)
χ^2 (of 5)	9.8	1.5	0.4	1.1	4.6
Wt. Av. (of 7)	0.371(2)	0.435(3)	0.223(2)	0.0633(10)	1.096(4)
χ^2 (of 7)	93	17	0.8	1.0	60
21-08-2008: Empty tank	1.33(4)	1.45(4)	1.01(3)	0.086(10)	3.87(7)
Twk spectrum	0.234(7)	0.280(8)	0.145(6)	0.069(4)	0.728(13)
Th_SS	0.052(3)	0.093(4)	0.101(4)	0.0004(2)	0.246(6)

In Table 6-11, the CR of the intervals were corrected by subtracting the contribution of cosmics from the seven spectra and from the empty tank spectrum. It is noted that the reduced chi-square values for the intervals III_a and III_b: 15.6 and 2.9, respectively, are smaller compared to those before correction for cosmics. The reduced chi-square value: 0.4 associated with the weighted average CR of interval II (0.223 ± 0.002 cps) indicates that there is no significant change in the CR for the various spectra. A further correction was made to the CR in the radon intervals by subtracting the thorium contribution. The results of the latter correction are presented in Table 6-12. Table 6-12 also shows the CR of a simulated and calibrated standard spectrum of U/Rn. The reduced $\chi^2(7)$ -values associated with the weighted average CR are 13.5, 2.2, 6.7 and 3.2 for the intervals III_a, III_b, III and the total interval, respectively. These high values after all the corrections could indicate that the CR in these intervals is not constant for the various background spectra. A possible qualitative explanation for the variability in terrestrial radiation may be the change in soil water content during the KCl measurements. Increasing soil moisture content will reduce the apparent activity concentrations [de Groot *et al.*, 2008] and will hamper the radon exhalation. Changes in radon (^{222}Rn) exhalation are indicated by the changes in the two energy intervals around the U/Rn peaks. The weighted averages of the CR in the interval III_a for the five KCl spectra has reduced χ^2 -values of 9.8 (Table 6-10), 2.8 (Table 6-11) and 1.8 (Table 6-12) and indicates that even over a

period of half a day the count rate in this interval may change by about 15%. From the value for this interval in the calibrated U/Rn standard spectrum: 0.085 ± 0.003 cps/(Bq/l), this change corresponds to about 0.7 Bq/l. A comparable change is observed in the interval III_b. The comparison with the two tap-water concentrations indicates a change of about 2.5 Bq/l. The calculated change in background radon, 2.5 Bq/l, is for the time being an estimate for the systematic uncertainty made by the assumption that the terrestrial background is a constant over a period of a few days. The systematic decrease of χ^2 -values from Table 6-10 to Table 6-12 is probably caused by the cosmic and thorium correction made to the interval's CR. We would like to point out that this background radon effect is most likely due to γ -rays associated with radon daughters (in air) and probably come from the direction of the top of tank since the detector is not shielded enough from this top direction, only ~ 20 cm depth of water. Further discussion on the geometry effect will be presented in section 6.7.

Contrary to the apparent temporal change of content in the radon intervals, the CR of the thorium interval seems to be constant over the same period of measurements. This is expected since the Th-soil radioactivity is not expected to vary significantly with time.

Table 6-11: The cosmic corrected CR in the subintervals for the measured spectra of Table 6-10 and the corresponding weighted averages CR and their associated reduced chi-square values.

Intervals in MeV description	1.6-1.85 III _a (cps)	1.85-2.4 III _b (cps)	2.4-2.75 II (cps)	1.6 -3.0 Total (cps)
23-04-2008: TW_5h	0.23(2)	0.21(2)	0.090(10)	0.53(4)
24-04-2008: TW_2h	0.27(2)	0.23(2)	0.086(13)	0.59(5)
24-04-2008: 5kg	0.073(19)	0.13(2)	0.075(13)	0.28(6)
24-04-2008: 10 kg	0.093(2)	0.15(2)	0.085(13)	0.33(5)
25-04-2008: 15 kg	0.13(2)	0.17(2)	0.099(12)	0.40(5)
25-04-2008: 20 kg	0.12(2)	0.14(2)	0.090(12)	0.35(5)
25-04-2008: 25 kg	0.15(2)	0.17(2)	0.099(12)	0.43(5)
Wt. Av. (of 5)	0.115(8)	0.154(10)	0.090(6)	0.36(2)
χ_R^2 (of 5)	2.8	0.6	0.6	1.1
Wt. Av. (of 7)	0.157(7)	0.175(8)	0.090(5)	0.423(19)
χ_R^2 (of 7)	15.6	2.9	0.4	4.6
21-08-2008: Empty tank	1.03(5)	1.10(6)	0.83(4)	2.96(13)

Table 6-12: The cosmics corrected CRs of Table 6-11 are corrected further for thorium contribution. Also presented are the weighted averages of the corrected CR and their associated reduced chi-square values.

Intervals in MeV description	1.6-1.85 III _a (cps)	1.85-2.4 III _b (cps)	1.6-2.4 III (cps)	1.6-3.0 Total (cps)
23-04-2008: TW_5h	0.180(17)	0.13(2)	0.31(4)	0.31(5)
24-04-2008: TW_2h	0.23(2)	0.15(3)	0.39(4)	0.38(6)
24-04-2008: 5kg	0.03(2)	0.07(3)	0.10(4)	0.10(6)
24-04-2008: 10 kg	0.05(2)	0.07(3)	0.12(4)	0.12(6)
25-04-2008: 15 kg	0.081(19)	0.08(2)	0.16(4)	0.16(6)
25-04-2008: 20 kg	0.07(2)	0.06(2)	0.13(4)	0.13(6)
25-04-2008: 25 kg	0.10(2)	0.08(2)	0.18(4)	0.18(6)
Wt. Av. (of 5)	0.069(9)	0.071(11)	0.14(3)	0.14(3)
χ^2_r (of 5)	1.8	0.1	0.6	0.3
Wt. Av. (of 7)	0.111(7)	0.093(9)	0.205(16)	0.20(2)
χ^2_r (of 7)	13.5	2.2	6.7	3.2
U/Rn_SS	0.085(3)	0.034(2)	0.119(4)	0.123(4)
21-08-2008: Empty tank	0.61(6)	0.34(8)	0.95(13)	0.94(19)

The temporal changes of background radon were investigated further by carrying out day and night continuous measurements (for about 24 hours) and, after being stopped for some time because of rain, for further six hours. These measurements were divided into two hour duration sub-measurements and analyzed using a similar approach as described above. The CR in intervals I (cosmic), II (thorium) and III (U/Rn) are plotted in Figure 6-9.

The diurnal variations occur only in the U/Rn interval and not in the Th and cosmic intervals as clearly observable in Figure 6-9. The U/Rn count rate reaches a minimum value at time of about 15:00 to 17:00 in the afternoon and increases systematically to its maximum value at about 03:00 to 05:00 in the morning. No meteorological parameters have been monitored but it was noticed that the wind started blowing (gale force north-westerly) from about 23:00 on the 14-07-2008.

These diurnal variations have similar patterns to what has been reported before e.g. Sesana *et al.*, 2006. The most plausible explanation for these variations is that we observe a variation in the U/Rn CR due to variation in Rn concentration in the air surrounding the tank where γ -rays reached the detector mainly from the top. The fact that the CR of Th remains unchanged makes it plausible that there is no change in the γ -radiation intensity coming from the soil. Diurnal radon variations in outdoor air is generally explained by the fact that in the evenings the temperature drops causing a thinner mixing layer for the exhaled radon as the air near the surface is not heated anymore and starts to cool by radiating heat to space. Thus, the radon builds up in the air layer close to the surface. When the temperature increases around sunrise, the air

starts rising causing a thicker mixing layer and hence more dilution. Consequently, the radon concentration in the ambient air drops.

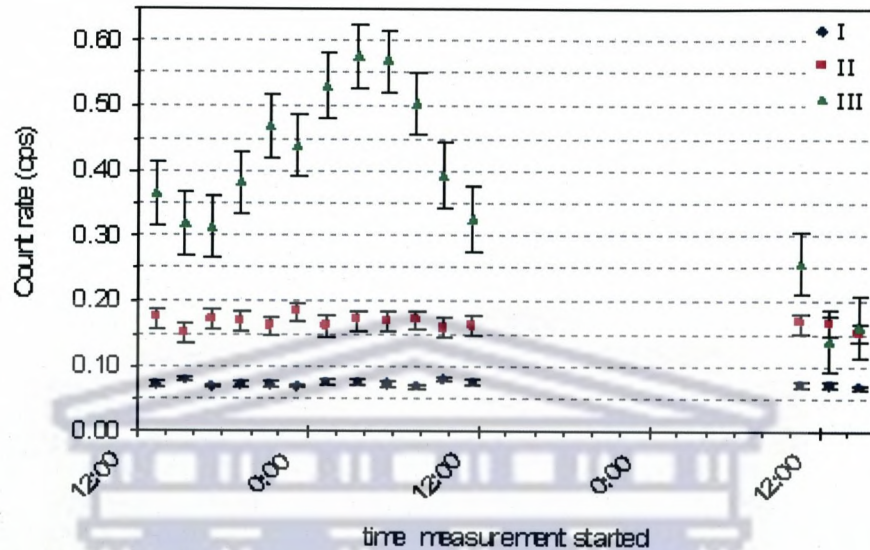


Figure 6-9: Variations of count rate for U/Rn (interval III), thorium (interval II) and cosmic rays (interval I) measured with the MEDUSA detector inside the tank filled with tap water. Measurements took place in the period of 14 to 16 July 2008. The horizontal axis represents the local time starting on 14 July 2008 at 13h16 and ending on 16 July 2008 at 12h20.

After it rained, the U/Rn CR values even drop further; no CR change is observed in the Th and cosmic intervals. During these measurements there was hardly any wind that could have caused vertical mixing. This drop therefore is likely due to a combined effect of radon washed out by the rain and a reduction in exhalation of radon by the wet soil top layer.

To conclude the section, the background radiation was not found to be constant. Cosmic rays and terrestrial thorium γ -rays were found to be fairly constant over a few days' measurements. Radon exhalation made variations in the CR for U γ -ray lines of about 15% over half a day and 60% over several days, most likely due to changes in radon concentrations in the surrounding air. While the thorium and cosmic rays did not vary significantly after rain, the radon CR decreased dramatically. This effect is likely due to a combination of wash out of airborne radon and a temporary reduction of radon exhalation from the soil.

6.7 Geometry effect

In the previous section, it was shown that the background radon varies substantially with time on a scale of hours and depends on the weather conditions. In addition to the radon in air, there are background γ -rays (emitted from terrestrial radionuclides such as U, Th and K present in the soil underneath and around the detector and in the buildings in the vicinity) that could reach the detector.

This section presents the results of investigating the optimum position for placing the detector in the tank for minimizing the background contribution to *quasi in-situ* measurements of radon in water using the MEDUSA-tank geometry. This task is achieved by inserting the detector in the tank full of water and determines the detector's response at various heights from the bottom of the tank.

The assumption made was that the background γ -rays are mainly from the sides and directly from underneath the tank. When filling the tank with water, the minimum distances traversed by the γ -rays to the detector are 51.5 cm (horizontally from the sides) and the detector height above the bottom of the tank (minimum vertical distance that depends on where the detector is positioned).

A first estimation of the shielding factors for the K, U/Rn and Th were made using the distances of 51.5 cm (from the sides) and a height of 100 cm (from the bottom of the tank) and the mass attenuation coefficients, $\mu\rho$ ($\text{cm}^2 \text{g}^{-1}$), of water as presented in CHAPTER 2 (Table 2-2). The mass attenuation coefficients that correspond to K, U/Rn (average energy 2.0 MeV) and Th in their respective intervals were calculated (using the interpolation) and presented in column 3 of Table 6-13. The shielding factors for horizontal and vertical γ -rays were then estimated as shown in Table 6-13 (column 4 and 5, respectively). For these estimations, the water density was assumed to be 1.0 g cm^{-3} ; no build up effects have been included. According to the geometry used for this study, the horizontal distance will remain unchanged when filling the tank. Table 6-13 also shows the estimated percent γ -rays reaching the detector horizontally and vertically, calculated as the reciprocal of the shielding factors. Although, the percentage of γ -rays reaching the detector is much higher for the sideways entering γ -rays, the ratio of the actual contribution will depend on the effective activities seen from the bottom and the side.

Table 6-13: Mass attenuation coefficients for various γ -ray energies and the corresponding shielding factors, estimated based on the interpolated attenuation coefficients for the intervals specified and water surrounding the detector in the tank, for horizontal and vertical γ -rays emitted from K, U/Rn and Th. The last two columns represent the percent γ -rays reaching the detector¹⁷.

Radionuclide	E_γ (MeV)	Interp. μ_p ($\text{cm}^2 \text{g}^{-1}$)	horizontal shielding factor	vertical shielding factor	% γ -rays reaching detector (sides)	% γ -rays reaching detector (bottom)
K	1.46	0.0576	19	318	5.1	0.3
U/Rn	2.0 (av.)	0.0492	13	137	7.9	0.7
Th	2.6	0.0430	9	74	10.9	1.4

To investigate the optimum position of the detector, the tank was filled with tap water and the detector was placed at several heights from the bottom of the tank. At each height, a spectrum was accumulated for at least five hours and analyzed with the hybrid approach. The shielding factors were obtained by dividing the CR when the tank was empty by the CR when the tank was filled with water at the various heights of the detector.

Table 6-14 presents the shielding factors calculated from the CRs in the various energy intervals. The shielding factor for the cosmic rays (interval I) increases with lowering the detector, which is expected, since the cosmic rays mainly come from the top. The Th and K γ -rays are mainly emitted from soil underneath and around the tank and the building in the vicinity. By lowering the detector, the horizontal γ -rays dominate as the height of the detector is greater than the radius. This is clear from the constant shielding factors of the Th and K with weighted averages of 11.5 ± 0.5 and 70 ± 40 (associated with $\chi_R^2 = 0.4$ and 0.05), respectively, which are consistent within uncertainties with the estimated values (Table 6-13) for the horizontal shielding. The high uncertainties are possibly due to interdependences of the corrections, which were ignored during the manipulation of the low background count rates. It appears that the γ -rays from K are almost totally shielded possibly because it has a relatively low energy in the spectrum and most likely emitted predominantly from the soil underneath the tank. The very low value of chi-square associated with the weighted average shielding factor of K is due to the very high statistical uncertainties. Similar to the Th, there is no significant improvement in the shielding factors for the U/Rn when changing the detector position. Thus, the current measurements could not show any preferable position for placing the detector to effectively shield γ -rays emitted by terrestrial radionuclides and radon in air. This is contrary to what is expected from the calculations

¹⁷ The γ -rays reaching the detector were calculated as the reciprocal of the shielding factors.

in Table 6-13 and the discussion of Table 2-2 in which a monoenergetic pencil beam was assumed. The values in these tables suggest that the detector has to be lowered by at least 50 cm so as to reduce γ -rays coming from the top by more than 90%.

Table 6-14: Shielding factors calculated by dividing the CR (cps) of each interval when the tank was empty by those when the tank was filled with water for the various distances (heights) of the centre of the detector from the bottom of the tank. Intervals *II* and *IV* were corrected for U/Rn contribution.

Height (cm)	1.3-1.6 MeV (IV)	1.6-2.4 MeV (III)	2.4-2.75 MeV (II)	2.75 -3.0 MeV (I)
100	200(400)	6.4(1.7)	10.1(1.3)	1.44(5)
95	200(400)	6.6(1.6)	10.6(1.2)	1.59(6)
90	200(600)	12(6)	12.7(1.8)	1.60(6)
85	400(2000)	9(3)	12.0(1.6)	1.67(7)
80	100(200)	10(4)	12.0(1.4)	1.81(7)
70	60(50)	6.8(1.4)	11.5(1.2)	1.94(7)
90 (ditto)	-3000(200000)	6.9(1.9)	12.7(1.9)	1.51(6)
85 (ditto)	200(500)	4.9(9)	12.4(1.7)	1.65(7)
Wt. av.	70(40)	6.2(6)	11.5(5)	1.63(2)
Red. chi-square	0.05	0.8	0.4	6.6

6.8 Summary, discussion and conclusion

A new method of measuring radon in the field using γ -ray spectrometry was presented in this chapter. The method is based on a MEDUSA detector inserted in a steel drum or in a plastic tank of volumes 210 and 1000 liters, respectively. As such, the radon in-water is measured in the field after grab sampling. This is, therefore, a *quasi in-situ* approach. The spectra were analyzed using a hybrid approach that combines the advantages of both FSA and the Windows methods. The approach, which was described in section 6.3, provided an analysis procedure of the γ -spectrum using wide, nuclide dominated windows and standard spectra for estimating continuum contributions. This was achieved by setting four energy intervals on the high energy part of the MEDUSA measured γ -ray spectrum: 1.6 – 3.0 MeV. Such settings help reduce the Compton multi-scatter contribution, mainly present at the low energy part of the spectrum.

The detection efficiency was calibrated using KCl salt dissolved in both the drum and the tank which were filled with tap water. The calibration factor was deduced from comparing the MEDUSA detector response with the calculated (include simulation) activity concentration of the ^{40}K (see Eq. 6-8). The calibration factors were thus determined to be 0.455 ± 0.019 and 0.551 ± 0.018 for the drum and the tank geometries, respectively.

The new method was used for measuring radon in borehole water in-the-field and the results were compared to their counterparts measured in the laboratory using a HPGe detector and screw-top Marinelli beakers. The MEDUSA measured γ -spectra were analyzed using the hybrid approach. The results showed that the comparison between the MEDUSA- and the HPGe-derived radon concentrations has factors of 0.86 ± 0.03 (Bq/l)/(Bq/l) and 1.10 ± 0.03 (Bq/l)/(Bq/l) for the drum and the tank, respectively. This means that for the drum the MEDUSA-derived radon concentration are 14% less than those derived from the HPGe whereas for the tank the concentrations are 10% higher than those of the HPGe. These differences are not unreasonable considering that we are comparing field measurements, associated with various systematic effects, and well controlled laboratory measurements.

The minimum detectable activity (MDA) of the method was estimated using the Theewaterskloof background spectrum (measured for ~ 1.3 hrs) and found to be 0.4 Bq/l ^{222}Rn for the MEDUSA inserted in the tank and 0.6 Bq/l ^{222}Rn for the MEDUSA inserted in the drum. It is expected that the statistical uncertainty leading to the MDA can be further reduced by a longer measuring time of the “background” spectrum.

Measurements were also carried out to investigate variability of ambient background γ -rays and to explore the effective shielding of these γ -rays. These background measurements showed that the ambient background was not constant due to variability in radon in the surrounding air.

In this chapter, a new method was described and calibrated. A good MDA was achieved and the radon in the iThemba LABS borehole was measured with an uncertainty of not more than 17%. From comparing the present drum and tank geometries, it seems that the drum geometry is practically suitable for measuring radon in the field more rapidly and reliably. Future work to be carried out includes the measurement of the background for a longer time and to test the set-up by measuring radon in-water in some other locations. However, the drum geometry is sensitive to ambient background radiation; therefore, one has to take into consideration background effects.

CHAPTER 7 SUMMARY, CONCLUSIONS AND OUTLOOK

7.1 Introduction

There is a growing interest, worldwide and in South Africa in particular, of using radon (^{222}Rn) as a natural tracer in hydrogeological applications. As mentioned in CHAPTER 1, the Water Research Commission (WRC), the CSIR (South Africa) and the iThemba LABS have embarked on a multi-disciplinary project to look into the prospect of using radon as a tracer to assess the possible influence of gold-mining activities on the fresh water aquifers in the West Rand Basin area near Krugersdorp and part of the Vaal River near Orkney.

This work emerged from the potential use of radon as a natural tracer in South African aquifers and rivers with specific focus on investigating the aspects of radon measurement methodologies within the context of the project taking into account the available radon measuring techniques. Therefore, the aims as stated in CHAPTER 1 were: (1) *to optimize the measurement of radon in water via γ -ray spectrometry using a laboratory-based hyper-pure germanium (HPGe) detector*. The optimization involves investigating statistical and systematic uncertainties due to sampling, measurement and analysis; (2) *to develop a model that may describe the time evolution of radon concentrations during aquifer sampling to help estimate some of the aquifer characteristics*. After optimization, the HPGe method was used for carrying out borehole water measurements for testing the model; (3) *to develop an in-field radon measurement technique based on a MEDUSA system that comprises a CsI(Na) scintillation detector*. The idea behind measuring radon in-field was to avoid sending samples to laboratories when studying remote areas. Sending samples to laboratories is associated with the risk of radon loss due to radon decay and water shakeup during transport in addition to possible delay of laboratory results, which may be received long after field trip has finished.

It was also stated in CHAPTER 1 that for hydrogeological applications of radon measurements, minimum detectable activity (MDA) and precision are the key parameters whereas accuracy is of lower priority. In this regard, an accuracy of 25% due to systematic uncertainties is good enough when it is compared to uncertainties in

geological and hydrological description of radon generation in aquifers. The requirements of low MDA and good precision are constrained by the preference of short measuring time to survey large areas with a high density of measuring points.

Radon concentrations in groundwater are generally higher than those of surface water. This is partly due to the occurrence of groundwater within rock and soil formations that contains relatively high radium content, thus radon is generated continuously. In addition, radon loss (discounting radioactive decay) is minimal since groundwater is not in direct contact with air as compared to surface water. Radon concentrations measured in some of the Western Cape groundwaters are typically in the range from 3 to 380 Bq/l whereas water from mining areas (borehole, springs, and mines water) has radon concentration in the range from 1.5 to 70 Bq/l. On the other hand, radon flux from some mine dumps in the Witwatersrand mining area was estimated to be about $0.1 \text{ Bqm}^{-2}\text{s}^{-1}$ [Lindsay *et al.*, 2004]. Although radon in air was not measured in this area, if one assumes an upper limit for radon in air of concentration of 100 Bq/m^3 (which corresponds to 0.1 Bq/liter), then surface water in equilibrium with this air will have a radon concentration of only 0.02 Bq/l. This latter value was estimated from the Oswald partition coefficient (~ 0.2) at a temperature of about 25°C , see CHAPTER 2 (Table 2-3). So, even 1 Bq/liter in the water could indicate an influx from an on-land source. Therefore, a method that measures at a level of 1.0 Bq/l in surface water would be sensitive enough. Therefore, a radon concentration of 3 Bq/l (lower limit) in mine and groundwater may be a target for the investigated methods.

7.2 Achievements

7.2.1 Validation of the HPGe method

Radon in water has been measured *via* γ -ray spectrometry using a HPGe detector situated at iThemba LABS – Cape Town and a 1.3-liter Marinelli beaker. The optimum results were obtained by deriving radon concentration from six γ -ray lines emitted in the decay of ^{214}Pb and ^{214}Bi , assumed to be in secular equilibrium with radon. The full-energy peak (FEP) efficiencies were determined by using KCl salt dissolved in tap water and borehole water of unknown radon concentration. The procedure involved using the FEP efficiency of ^{40}K at $E_\gamma = 1.46 \text{ MeV}$ to scale the six FEP efficiencies associated with the radon daughters and obtained from the measurement of the borehole water. The FEP efficiencies were validated against their counterparts simulated using the MCNPX code. For a measuring time of two hours and a full Marinelli beaker, a

the MCNPX code. For a measuring time of two hours and a full Marinelli beaker, a Minimum Detectable Activity (MDA) of 0.2 Bq/l (3σ) was obtained. As such, the first aim of optimizing the HPGe method was met. Further validation of the HPGe measurements is provided by the comparison to other methods as described in subsection 7.2.4 below.

7.2.2 Radon for representative sampling of aquifers

To investigate the role of radon in sampling aquifers, a borehole at iThemba LABS was studied over more than one year by carrying out ten pumping tests. In these investigations, the radon concentration was found initially increasing, as expected, with pumping time and eventually reaching a steady level. The time needed for the radon concentration to reach this level was estimated to be between the time required to pump out water equivalent to three to four of the borehole volumes (1.2 m^3), which is a generally known practice among hydrogeologists. After pumping out about 20 borehole volumes, a second jump in the radon was noticed. Therefore, the time for pumping-out four to 20 borehole water-volumes is most likely the time window for representative sampling of the iThemba LABS borehole.

7.2.3 A model for predicting time of borehole sampling

Based on the radon measurements for pumping tests, a physical model has been developed, derived from an activity balance. This model reproduces the change of radon concentration with pumping time and predicts the time for representative sampling. The analysis of the data produces almost a constant steady level of (33.4 ± 0.3) Bq/l radon concentration for the pumping tests over a period of one year and indicates that this value is characteristic for the aquifer. Thus, the first aim of this thesis (*to optimize the measurement of radon in water via γ -ray spectrometry using a laboratory-based hyper-pure germanium (HPGe) detector*) has been achieved with a sensitivity better than the traditional methods. By describing the radon concentrations in the pump tests by a simplified model, the second aim of the thesis (*to develop a model that may describe the time evolution of radon concentrations during aquifer sampling to help estimate some of the aquifer characteristics*) has been fulfilled. However, this model needs to be further developed and tested.

7.2.4 Radon-in-water measurements in mining areas

Radon has been measured in two South African areas where there are gold mining activities. The areas are West Rand Basin near Krugersdorp, Gauteng province, and the Vaal River near Orkney (North West province). The focus was on assessing the measurement procedure including the minimum detectable activity (MDA) of the various techniques used. A second objective that has also been achieved was to cross-check the various techniques as discussed in the next paragraphs.

Five techniques have been used to measure radon in water. Three of the techniques are based on alpha spectrometry. These are: the DurrIDGE RAD7 radon detector and two LS (liquid Scintillation) counters situated at NECSA, Pretoria, and at iThemba LABS-Gauteng, Johannesburg, laboratories. The other two are novel methods based on γ -ray spectrometry using the HPGe detector discussed in subsection 7.2.1 and the MEDUSA detector *in-situ* in the Vaal River only.

The existing techniques have the following MDAs: The RAD7 is used in the laboratory and in field measurements. The RAD7 MDA = 0.4 Bq/l for a sample volume of 0.25 l and 30 minutes measuring time. Due to low collection efficiency of the RAD7, the statistical uncertainties are above 70% for measuring samples of radon concentration ≤ 2.0 Bq/l. The LSC situated at the laboratory of the iTL-G was not calibrated for efficiency and provided results in counts per minute (CPM) for radon extracted from one liter water sample. Its minimum count per minute was ~ 1 CPM; the MDA for the LSC (NECSA), sample volume of 0.007 l, was determined for each measurement at 95% level and it was found to be in the range from 0.095 to 6.6 Bq/l.

The HPGe method optimized in this work has an MDA of 0.2 Bq/l for 1.3 l sample volume and two hours measuring time.

A conclusion was reached that the MEDUSA detector cannot be used for measuring radon in the Vaal River *in-situ*. This was due to the low radon concentration in the river-water, which is probably aggravated by agitation due to turbulent water flow.

The results showed that there is a good correlation between the RAD7 and the LSC (iTl-G) with a reduced chi-square value of 1.8. The RAD7 and the HPGe also showed good correlation with a reduced chi-square value of 2.7 and slope of 0.90 ± 0.04 . The slightly higher chi-square value, 2.7, associated with the RAD7-HPGe correlation suggests that some of the measurements may be prone to systematic uncertainties that most likely occurred during sampling. Similar to the HPGe, the LSC (NECSA) and the

RAD7 have a reasonable correlation with slope of 0.80 ± 0.07 and reduced chi-square value of 7. This latter high value of the reduced chi-square was attributed to discrepancies of radon concentration in some groundwater samples from the WRB area, which was also noticed to have extreme disequilibrium in the U-decay series as deduced from the high $^{234}\text{U}/^{238}\text{U}$ ratios ($\gg 1$) presented in Table 5-4 (CHAPTER 5, subsection 5.5.1).

In view of the results obtained, the LSC of iTL-G seems to have the lowest MDA, hence it is suitable for measuring water samples of low radon concentration. The RAD7 represents (to our knowledge) the only available in-field method in South Africa for measuring radon in water. However, the low collection efficiency and the small sample size may set a limit on comparing water samples of low radon concentration. The optimized HPGe method has the advantage of high reliability and relatively low MDA but it remains a laboratory-based method with low sample throughput.

The radon may also be concentrated using liquid scintillation oil and measured on a HPGe detector (destructive method). This method was also shown to have low MDA [Shizuma *et al.*, 1998]. The iTL-G method, however, is automated and has more sample throughput than the destructive HPGe method. However, both methods are laboratory-based and results may only be received after the field work is completed.

7.2.5 A novel method for measuring radon in the field

The third aim of this study, as mentioned in CHAPTER 1, is to develop a novel method for measuring radon-in-water in the field. The method comprises a MEDUSA detector inserted in a drum (volume ~ 210 l) or in a tank (volume ~ 1000 l) and analyzing the γ -ray spectra using a hybrid approach that combines the advantages of the full-spectrum analysis (FSA) method and the “windows” method. The hybrid analysis approach involves setting four energy intervals in the γ -ray spectra, each interval with a dominant contribution of one source of γ -radiation. Contributions of other radionuclides to these intervals were corrected using standard spectra simulated using the MCNPX code in the geometry of the MEDUSA detector inserted in a drum or in a tank. KCl salt in various quantities was dissolved in the tank and in the drum filled with tap water to determine the calibration of the MCNPX standard spectra.

The method was used to measure radon in the iThemba LABS borehole water in the field and the results were validated against their respective results obtained by measuring subsamples, sealed in Marinelli beakers, with the HPGe detector. The field

and the laboratory derived radon-concentrations agreed within $\pm 17\%$, which is within the accuracy required by hydrogeological applications of radon (25%) as discussed in CHAPTER 1. The MDA of the method was estimated using a background spectrum measured for about 1.3 hrs. The MDA was determined to be 0.4 and 0.6 Bq/l (at 2σ for half an hour measuring time) for the tank and the drum, respectively. These values are well within the requirements stated in the aim of this work for measuring both groundwater and mine water. The fact that this value is almost an order of magnitude higher than the estimated surface water concentration is not a serious limitation because the origin of lower radon concentrations would be disputed. In addition, the MDA values of the developed method are comparable to that of α -spectrometry using the RAD7 for in-the-field radon in water measurements. The advantage of the drum/tank method is that it may be more representative due to the large sample volume.

In the case of the drum geometry, caution need to be taken in accounting for surrounding radon. This component was estimated to be equivalent to radon concentration in water in the order of 2 Bq/l from measurements at the iThemba LABS.

7.3 Conclusions, outlook and recommendations

The method of measuring radon by γ -ray spectrometry using a HPGe detector and Marinelli beakers has been optimized. The results showed that a radon concentration of 30 Bq/l in water can be determined with good precision (5%) in a reasonable time by taking the weighted average of radon concentrations derived from six γ -lines associated with the decay of ^{214}Bi and ^{214}Pb in secular equilibrium with ^{222}Rn .

A model has been developed that uses the time-evolution of radon concentration in borehole water to indicate the pumping time required for sampling an aquifer. Given knowledge of the pump speed (v_p) and the borehole geometry (V_0), one can use the model to estimate the time for representative sampling from the aquifer (using a semi-cased borehole) by measuring only C_0 and $C(t)$ at a slightly later time.

A novel method has been developed, calibrated and tested for measuring radon in-water *quasi in-situ*, using the MEDUSA detector and a large volume of water in a container. The method's MDA is good enough to allow investigating aquifer characteristics and measuring radon in mine water. However, the method may not be sensitive enough to measure very low radon concentration (of the order of mBq/l) in

surface water. It should be noted that the method can be used in the field and it supplies results instantly.

The model described in subsection 7.2.3 above was derived for the particular case of the iThemba LABS borehole. Therefore, the model needs to be developed and tested at other boreholes and aquifers.

The hybrid analysis approach described in section 6.3 involves measuring a background spectrum and simulating standard spectra for ^{40}K , and the nuclides from the Th and U decay series using the MCNPX code. The statistical uncertainties associated with this background spectrum, taken at Theewaterskloof, would have been decreased if the measurement time was longer. Thus, it is recommended that the background spectrum be measured for a longer time. For the traditional FSA procedure, the inappropriate fitting of the peaks of the measured spectra yielded high chi-square values. This is most likely caused by the fact that the broadening function was not optimized in the simulation of the standard spectra used for this work. Hence, further investigation of the broadening function may be needed.

The developed *quasi in-situ* method of measuring radon in water using the MEDUSA-drum set-up needs to be tested at several aquifers. For surveying a large area using this method, the following procedure is recommended:

- We propose deploying six steel drums at pre-planned positions in the field. The drums can be filled with water from source of interest (ground or mine water) using for example a water pump.
- By measuring each drum for half an hour, one would expect to take three hours to measure the first set of drums. Each drum measured will be emptied and taken to another position.
- In this way, one can make a series of about 15 sequential measurements of radon-in-water in the field per day.

The results of this thesis have improved the method for radon-in-water measurements which should be useful in future applications of radon as a tracer.

REFERENCES

- Abass, M.I., 2006. *Validation of analytical formulae for the efficiency calibration of gamma detectors used in laboratory and in-situ measurements*. Appl. Radiat. Isot. 64, 1661 – 1664.
- Added, A. *et al.*, 2005. *Distribution of uranium and radium isotopes in an aquifer of a semi-arid region (Manouba-Essijoumi, North Tunisia)*. J. Environ. Radioact. 82, 371 – 381.
- Adelana, S. M.A., 2006. Department of the Earth Sciences, University of the Western Cape, South Africa. Private communication.
- Ahmed, N.K., 2004. *Natural radioactivity of ground and drinking water in some areas of Upper Egypt*. Turkish J. Eng. Environ. Sciences 28, 345 – 354.
- Al-Kazwini, A.T. and Hasan, M.A., 2003. *Radon concentration in Jordan drinking water and hot springs*. Journal of Radiological Protection 23, 439 – 448.
- Al-Masri, M. S. and Blackburn, R., 1999. *Radon-222 and related activities in surface waters of the English Lake District*. Appl. Radiat. Isot. 50, 1137 – 1143.
- Amrani, D., and Cherouati, D.E., 1999. *Health effects from radon-222 in drinking water in Algiers*. Journal of Radiological Protection 19, 275 – 279.
- Andersson, P.S. *et al.*, 1995. ^{238}U – ^{234}U and ^{232}Th – ^{230}Th in the Baltic Sea and in river water. Earth Planet Sci. Lett. 130, 217 – 234.
- Barnett, J.M. *et al.*, 1995. *Lung dose estimates from ^{222}Rn in Arizona groundwater based on liquid scintillation measurements*. Health Phys. 68, 699 – 703.
- Bertin, C., Bourg, A.C.M., 1994. *Radon-222 and chloride as natural tracers of the infiltration of river water into an alluvial aquifer in which there is significant river/groundwater mixing*. Environmental Science and Technology 28 (5), 794 – 798.
- Bertolo, A. and Bigliotto, C., 2004. *Radon concentration in waters of the geothermal Euganean basin—Veneto, Italy*. Radiation Protection Dosimetry 111(4), 355 – 358.
- Boeker, E., and van Grondelle, R. *Environmental Physics*. 2nd edition, 1999, John Wiley & Sons, Ltd.

- Bonotto, D.M. and Andrews, J.N., 1997. *The implications of laboratory ^{222}Rn flux measurements to the radioactivity in groundwater: the case study of a karstic limestone aquifer*. Applied Geochemistry 12, 715 – 726.
- Bonotto, D.M. and Andrews, J.N., 1999. *Transfer of radon and parent nuclides ^{238}U and ^{234}U from soils of the Mendip hills area, England, to the water phase*. Journal of Geochemical Exploration 66, 255 – 268.
- Bonotto, D.M. and Mello, C.B., 2006. *A combined method for evaluating radon progeny in waters and its use at Guarani aquifer, Sao Paulo State, Brazil*. J. Environ. Radioact. 69, 21 – 35.
- Bonotto, D.M., 2004. *Doses from ^{222}Rn , ^{226}Ra , and ^{228}Ra in groundwater from Guarani aquifer, South America*. J. Environ. Radioact. 76, 319 – 335.
- Bowring, C.S. and Banks, D., 1995. *Radon in private water supplies in SW England*. Journal of Radiological Prot. 15 (1), 73 – 76.
- Briesmeister, J.F., (Ed.): *“MCNP – A General Monte Carlo N-Particle Transport Code, Version 4C”*, LA-13709-M, Los Alamos National Laboratory (April 2000).
- Burnett, W.C. and Dulaiova, H., 2003. *Estimating the dynamics of groundwater input into the coastal zone via continuous radon-222 measurements*. J. Environ. Radioact. 86, 337 – 353.
- Burnett, W.C. *et al.*, 2001. *A continuous radon monitor for assessment of radon in coastal ocean waters*. J. Radioanalytical Nucl. Chem. 249, 167 – 172.
- Cecil, L.De., and Green, J.R., 2000. Radon-222. Chapter 6 in reference: Cook and Herczeg, 2000.
- Chuma, J.L., 1994. *Physica© Reference Manual*. TRIUMF, 4004 Wesbrook Mall, Vancouver, B.C., Canada V6T 2A3.
- Clark, I. and Fritz, P., 1997. *Environmental Isotopes in Hydrogeology*. CRC press LLC.
- Cohen, B.L. and Cohen, E.S., 1983. *Theory and practice of radon monitoring with charcoal adsorption*. Health Phys. 45, 501 – 508.
- Cook, G.T., *et al.*, 2003. *Environmental liquid scintillation analysis*. In reference: L'Annunziata, M.F. (ed.), 2003, 537 – 607.

- Cook, P.G. and Herczeg, A.L., 2000 (editors). *Environmental Tracers in Subsurface Hydrology*. Kluwer Academic Publishers.
- Cook, P.G. *et al.*, 2003a. *Determining natural groundwater influx to a tropical river using radon, chlorofluorocarbons and ionic environmental tracers*. *Journal of Hydrology* 277, 74 – 88.
- Corbett, D.R. *et al.*, 1997. *Radon tracing of groundwater input into Par Pond, Savannah River Site*. *Journal of Hydrology* 203 (1-4), 209 – 227.
- Cosma, C. *et al.*, 2008. *Radon in water from Transylvania (Romania)*. *Radiation Measurements* 43, 1423 – 1428.
- Cothorn, C. R. and Smith, J. E., 1987. *Environmental radon (Environmental science research, v.35)*. Plenum Press, New York (Google book).
- Countess, R.J., 1976. *Rn-222 flux measurements with a charcoal Canister*. *Health Phys.* 31, 456 – 457.
- Countess, R.J., 1978. *Measurement of ^{222}Rn in water*. *Health Phys.* 34, 390 – 391.
- Cozmuta, I., 2001. *Radon Generation and Transport – A Journey Through Matter*. A Ph.D. thesis; Rijksuniversiteit Groningen, The Netherlands.
- D'Alessandro, W. and Vita, F., 2003. *Groundwater radon measurements in the Mt. Etna area*. *J. Environ. Radioact.* 65, 187 – 201.
- Damon, R.W., 2005. *Determination of the photopeak detection efficiency of a HPGe detector, for volume sources, via Monte Carlo simulations*. Masters Thesis, University of the Western Cape (unpublished).
- Danali-Cotsaki, S. and Margomenou-Leonidopoulou, G., 1993. *^{222}Rn in Greek spa waters: correlation with rainfall and seismic activities*. *Health Phys.* 64, 605 – 612.
- David R. Lide (Ed.). *Handbook of chemistry and physics*. 77th edition, 1996 – 1997, CRC press.
- Davis, B.M. *et al.*, 2002. *Push-pull partitioning tracer tests using radon-222 to quantify non-aqueous phase liquid contamination*. *Journal of Contaminant Hydrology* 58, 129 – 146.
- Debertin, K. and Helmer, R. G., 2001. *Gamma- and X-ray Spectrometry with Semiconductor Detectors*. North-Holland. Physicist

- de Groot, A.V. *et al.*, 2008. *Sensitivity of in-situ γ ray spectra to soil density and water content*. Nucl. Instr. and Meth. A 600, 519 – 523.
- Dehnert, J. *et al.*, 1999. *Measurement of the infiltration speed of surface water with the help of the natural isotope radon-222* [Messung der infiltrations-geschwindigkeit von ober-flächenwasser mit hilfe des natürlichen Isotops Radon-222] Grundwasser 4 (1), 18 – 30.
- de Meijer, R. J. *et al.*, 1996. *Radiometry as a technique for use in coastal research*. New Techniques in Continental Shelf Research. Geological Society Special Publications 117, 289 – 297.
- de Meijer, R. J., 1998. *Heavy minerals: From 'Edelstein' to Einstein*. Exploration and Mining Geology 62, 81 – 103.
- Dosseto, A. *et al.*, 2008. *Uranium-series isotopes in river materials: Insights into the timescales of erosion and sediment transport*. Earth Planet Sci. Lett. 265, 1–17.
- Dua, S.K. *et al.*, 1995. *Electret method for continuous measurement of the concentration of radon in water*. Health Phys. 64, 605 – 612.
- Dubinchuk, V.T., 1981. *Radon and radium discharge to surface streams*. Water Resources 8 (1), 40 – 52.
- Dulaiova, H. *et al.*, 2005. *A multi-detector continuous monitor for assessment of ^{222}Rn in the coastal ocean*. J. Radioanal. Nucl. Chem. 263, 361 – 365.
- Durrani, S.A. and Ilic, R., 1997. *Radon Measurements by Etched Track Detectors*. World Scientific.
- Ellins, K.K., Roman-Mas, A., Lee, R., 1990. *Using ^{222}Rn to examine groundwater/surface discharge interaction in the Rio Grande de Manati, Puerto Rico*. Journal of Hydrology 115 (1-4), 319 – 341.
- Erees, F.S. *et al.*, 2007. *Radon concentrations in thermal-waters related to seismic events along faults in the Denizli Basin, Western Turkey*. Radiation Measurements 42, 80 – 86.
- Erlandsson, B. *et al.*, 2001. *Studies of the radon concentration in drinking water from the horst Söderåsen in Southern Sweden*. J. Environ. Radioact. 53, 145 – 154.

- Etiopio, G. and Martinelli, G., 2002. *Migration of carrier and trace gases in the Geosphere: an overview*. Physics of the Earth and Planetary Interiors 129, 185 – 204.
- Farai, I.P., and Sanni, A.O., 1992. ^{222}Rn in groundwater in Nigeria: a survey. Health Phys. 62, 96 – 98.
- Firestone, R.B., 1998. *Table of Isotopes*. 8th edition, John Wiley & Sons, Inc.
- Fleischer, R. L., 1983. *Theory of alpha recoil effects on radon releases and isotopic disequilibrium*. Geochimica et Cosmochimica Acta 47, 779 – 784.
- Fleischer, R. L., 1988. *Alpha-recoil damage: Relation to isotopic disequilibrium and leaching of radionuclides*. Geochimica et Cosmochimica Acta 52, 1459 – 1466.
- Freyer, K. *et al.*, 1997. *Sampling and Measurement of Radon-222 in Water*. J. Environ. Radioact. 37(3), 327 – 337.
- Garcia-Talavera, M., 2003. *Evaluating the suitability of various γ lines for the γ spectrometric determination of the ^{238}U in environmental samples*. Appl. Radiat. Isot. 59, 165 – 173.
- Garcia-Talavera, M., *et al.*, 2000. *Towards a proper modelling of detector and source characteristics in Monte Carlo simulations*. Appl. Radiat. Isot. 52, 777 – 783.
- Garcia-Talavera, M., *et al.*, 2001. *Coincidence summing corrections for the natural decay series in γ ray spectrometry*. Appl. Radiat. Isot. 54, 769 – 776.
- Ghose, S., Alam, M.N., Islam, M.N., 2000. *Concentrations of ^{222}Rn , ^{226}Ra and ^{228}Ra in surface sea water of the Bay of Bengal*. J. Environ. Radioact. 47 (3), 291 – 300.
- Gilmore, G. and Hemingway, J., 1995. *Practical Gamma-Ray Spectrometry*. John Wiley & Sons, Ltd.
- Godoy, J.M. and Godoy, M.L., 2006. *Natural radioactivity in Brazilian groundwater*. J. Environ. Radioact. 85, 71 – 83.
- Gutierrez-Villanueva, J.L. *et al.*, 2008. *Calibration of a portable HPGe detector using MCNP code for the determination of ^{137}Cs in soils*. J. Environ. Radioact. 99, 1520 – 1524.
- Hamanaka, S. *et al.*, 1998. *Radon concentration measurement in water by means of a liquid-scintillation spectrometry with a PERALS spectrometer*. Nuclear Instrument and Methods in Physics Research A 410, 314 – 318.

- Harris, C. *et al.*, 1999. *A preliminary investigation of the oxygen and hydrogen isotope hydrology of the greater Cape Town area and an assessment of the potential for using stable isotopes as tracers*. Water SA 25 (1), 15 – 24.
- Helmer, R.G. *et al.*, 2004. *Precise efficiency calibration of a HPGe detector up to 3.5 MeV, with measurements and Monte Carlo calculations*. Appl. Radiat. Isot. 60, 173 – 177.
- Hendriks, P. H. G. M., *et al.*, 2001. *Full-spectrum analysis of natural γ -ray spectra*. J. Environ. Radioact. 53, 365 – 380.
- Hendriks, P. H. G. M. *et al.*, 2002. *MCNP modelling of scintillation-detector γ -ray spectra from natural radionuclides*. Appl. Radiat. Isot. 57, 449 – 457.
- Hendriks, P., 2003. *In-depth γ -ray studies: Borehole measurements*. A Ph.D. thesis; Rijksuniversiteit Groningen, The Netherlands.
- Hobbs, P.J., 2008. *The use of ^{222}Rn as a hydrological tracer in natural and polluted environments*. Progress report No. 2, CSIR, South Africa.
- Hoehn, E., Von Gunten, H.R., 1989. *Radon in groundwater: a tool to assess infiltration from surface waters to aquifers*. Water Resources Research 25 (8), 1795 – 1803.
- Höhener, P. and Surbeck, H. 2004. *Radon-222 as a tracer for non-aqueous phase liquid in the Vadose zone: experiments and analytical model*. Vadose Zone Journal 3, 1276 – 1285.
- Hussain, N. *et al.*, 1999. *Use of ^{222}Rn and ^{226}Ra to trace groundwater discharge into the Chesapeake Bay*. Marine Chemistry 65, 127 – 134.
- IAEA-TECDOC-777, 1993. *Mathematical models and their applications to isotope studies in groundwater hydrology*. International Atomic Energy Agency.
- Inoue, M. *et al.*, 2006. *Seasonal variations in $^{228}\text{Ra}/^{226}\text{Ra}$ ratio within coastal waters of the Sea of Japan: implications for water circulation patterns in coastal areas*. J. Environ. Radioact. 89, 38 – 149.
- Johnston, A. and Martin P., 1997. *Rapid analysis of ^{226}Ra in waters by γ -ray spectrometry*. Appl. Radiat. Isot. 48 (5), 631 – 638.
- Kahn, B. *et al.*, 1990. *Analysis of ^{228}Ra and ^{226}Ra in public water supplies by a γ -ray spectrometer*. Health Phys. 59(1), 125 – 131.

- Kelly, W., 2006. University of Illinois. Private communication (14 June, 2006).
- Kendal, G.M., 2004. *Controls on radioactivity in water supplies in England and Wales, with special reference to radon*. Journal of Radiological Protection 24, 409 – 412.
- Kessler, M.J., 1989. *Liquid Scintillation Analysis*. Publication no. 169.3052 © PACKARD Instrument Co. Inc.
- Kluge, T. *et al.*, 2007. *Tracing and quantifying groundwater inflow into lakes using a simple method for radon-222 analysis*. Hydrol. Earth Syst. Sci. 11, 1621 – 1631.
- Knoll, F., 2000. *Radiation Detection and Measurement*. Third edition, John Wiley & Sons, Inc.
- Kobayashi, Y., 1988. *Laboratory manual for Liquid Scintillation Counting*. PACKARD © Instrument Co. Inc.
- Köhler, M. *et al.*, 2002. *Comparison of methods for the analysis of ^{226}Ra in water samples*. Appl. Radiat. Isot. 56, 387 – 392.
- Kotrappa, P. and Jester, W.A., 1993. *Electret ion chamber radon monitors measure dissolved ^{222}Rn in water*. Health Phys. 64, 397 – 405.
- Kotrappa, P. *et al.*, 1988. *An electret passive environmental ^{222}Rn monitor based on ionization measurement*. Health Phys. 43, 399 – 405.
- Kotrappa, P. *et al.*, 1990. *A practical E-PERMTM (electret passive environmental radon monitor) system for indoor ^{222}Rn measurement*. Health Phys. 58, 461 – 467.
- Kotze, D. *et al.*, 2008. *Radioactivity analysis of water*. Report no. RA-08894, RadioAnalysis laboratory, Nuclear Energy Corporation of South Africa (NECSA), Pretoria.
- Kraemer, T.F. and Genereux, D.P., 2000. *Applications of Uranium- and Thorium-Series Radionuclides in Catchment Hydrology Studies*. Chapter 20 in reference: Cook, P.G. and Herczeg, A.L., 2000 (editors).
- Krane, K.S., 1988. *Introductory Nuclear Physics*. John Wiley & Sons, Inc.
- Krest, J.M. and Harvey, J.W., 2003. *Using natural distributions of short-lived radium isotopes to quantify groundwater discharge and recharge*. Limnol. Oceanogr. 48(1), 290 – 298.

- Kronfeld, J. *et al.*, 1994. *A new explanation for extreme $^{234}\text{U}/^{238}\text{U}$ disequilibria in a dolomitic aquifer.* Earth Plan. Sci. Lett. 123, 81 – 93.
- Kullab, M., 2005. *Assessment of radon-222 concentrations in buildings, building materials, water and soil in Jordan.* Appl. Radiat. Isot. 62, 765 – 773.
- L'Annunziata, M.F. (ed.), 2003. *Handbook of Radioactivity Analysis.* 2nd edition, Academic Press.
- L'Annunziata, M.F., 2003a. *Solid Scintillation Analysis.* In reference: L'Annunziata, M.F. (ed.), 2003, 845 – 988.
- L'Annunziata, M.F., 2003b. *Cherenkov counting.* In reference: L'Annunziata, M.F. (ed.), 2003, 719 – 797.
- Lawrence, E. *et al.*, 1991. *Geohydrologic, Geochemical, and geologic controls on the occurrence of radon in ground water near Conifer, Colorado, USA.* Journal of Hydrology 127, 367 – 386.
- Lee, J.-M. and Kim, G., 2006. *A simple and rapid method for analyzing radon in coastal and ground waters using a radon-in-air monitor.* J. Environ. Radioact. 89(3), 219 – 228.
- Lee, M.H. *et al.*, 2008. *Determination of a Minimum Detectable Activity through a measurement of Pu isotopes in environmental samples.* Bull. Korean Chem. Soc. 29(6), 1162 – 1166.
- Lehmann, B.E. and Purtschert, R., 1997. *Radioisotope dynamics- the origin and fate of nuclides in ground water.* Applied Geochemistry 12, 727 – 738.
- Leo, W.R., 1994. *Techniques for Nuclear and Particle Physics Experiments.* Second edition, Springer-Verlag.
- Ligero, R.A. *et al.*, 2006. *Diffusion of ^{226}Ra and ^{40}K radionuclides reproduce in underwater sedimentary columns in laboratory.* J. Environ. Radioact. 87, 325 – 334.
- Lilley, J.S., 2001. *Nuclear Physics: Principles and Applications.* John Wiley & Sons, Ltd.
- Lindsay, R. *et al.*, 2004. *Measurement of radon exhalation from a gold-mine tailings dam by γ ray mapping.* Radiation Physics and Chemistry 71, 797 – 798.

- Lippmann, J. *et al.*, 2005. *On the geochemistry of gases and noble gas isotopes (including ^{222}Rn) in deep crustal fluids: the 4000 m KTB-pilot hole fluid production test 2002-03*. *Geofluids* 5, 52 – 66.
- Longoria, L.C. and Benitez, J.S., 1996. *Full energy efficiency of a Ge detector as a function of energy and distance*. *Appl. Radiat. Isot.* 47 (3), 339 – 343.
- Lucas, H.F., 1957. *Improved low-level alpha-scintillation counter for radon*. *Rev. Scientific Instrum.* 28, 680 – 683.
- Lucas, H.F., 1964. *A fast and accurate survey technique for both radon-222 and radium-226*. In: *The Natural Radiation Environment* (edited by J.A.S. Adams and W.M. Lowder), University of Chicago Press, p. 315.
- Lyons, L., 1986. *Statistics for nuclear and particle physicists*. Cambridge University Press.
- Maleka, P., 2007. Department of physics, University of the Western Cape, South Africa. Private communication.
- Mancini, C., Gianelli, G., 1994. *Determination of waterborne ^{222}Rn concentrations using AC canisters*. *Health Phys.* 69, 403 – 405.
- Marques, A.L., Dos Santos, W., Geraldo, L.P., 2004. *Direct measurements of radon activity in water from various natural sources using nuclear track detectors*. *Appl. Radiat. Isot.* 60 (6), 801 – 804.
- Mathieu, G.G. *et al.*, 1988. *System for measurement of ^{222}Rn at low levels in natural waters*. *Health Phys.* 55 (6), 989 – 992.
- Maučec, M. *et al.*, 2001. *Monte Carlo simulation of natural gamma ray spectrometry for underwater surfaces*. *Proceedings, International Conference on Advanced Monte Carlo for radiation physics, particle transport simulation and applications – MC 2000*, Lisbon, Portugal, in A. Kling *et al.* (Eds.), Springer, 773 – 777.
- Mulligan, A.E. and Charette, M.A., 2006. *Intercomparison of submarine groundwater discharge estimates from a sandy unconfined aquifer*. *Journal of Hydrology* 327, 411 – 425.
- Newman, R.T., 2006. Head: Physics Group, iThemba LABS, Cape Town, South Africa. Private communication.

- Nikezic, D. *et al.*, 2006. *Absorbed dose in target cell nuclei and dose conversion coefficient of radon progeny in the human lung*. J. Environ. Radioact. 89, 18 – 29.
- Nishizawa, S. *et al.*, 1998. *Radon, Cl, and SO₄²⁻ anomalies in hot spring water associated with the 1995 earthquake swarm off the east coast of the Izu Peninsula, central Japan*. Applied Geochemistry 13, 89 – 94.
- Oliveira, J. *et al.*, 2003. *Reconnaissance of submarine groundwater discharge at Ubatuba coast, Brazil, using ²²²Rn as a natural tracer*. J. Environ. Radioact. 69, 37 – 52.
- Osvath, I. and Povinec, P. P., 2001. *Seabed gamma-ray spectrometry: applications at IAEA-MEL*. J. Environ. Radioact. 53, 335 – 349.
- Parekh, P. *et al.*, 2003. *Non-destructive determination of ²²⁴Ra, ²²⁶Ra and ²²⁸Ra concentrations in drinking water by gamma spectroscopy*. Health Phys. 85(5), 613 – 620.
- Perez-Andujar, A. and Pibida L., 2004. *Performance of CdTe, HPGe and NaI(Tl) detectors for radioactivity measurements*. Appl. Radiat. Isot. 60, 41 – 47.
- Pohl, E. and Pohl-Ruling, 1976. *Determination of environmental or occupational ²²²Rn in air and water and ²²⁶Ra in water with feasible and rapid methods for sampling and measurement*. Health Phys. 31, 343 – 348.
- Povinec, P.P. *et al.* 1996. *Underwater Gamma spectrometry with HPGe and NaI(Tl) detectors*. Appl. Radiat. Isot. 47(9), 1127 – 1133.
- Povinec, P.P. *et al.* 2006. *Characterisation of submarine groundwater discharge offshore south-eastern Sicily*. J. Environ. Radioact. 89, 81 – 101.
- Prichard, H.M., 1983. *A solvent extraction technique for the measurement of Rn at ambient air concentrations*. Health Phys. 45 (2), 493 – 499.
- Prichard, H.M., and Gesell, T.F., 1977. *Rapid measurements of ²²²Rn concentrations in water with a commercial liquid scintillation counter*. Health Phys. 33, 577 – 581.
- Sanchez, M.A. *et al.*, 1995. *Gamma and alpha spectrometry for natural radioactive nuclides in the spa water of Extremadura (Spain)*. J. Environ. Radioact. 28(2), 209 – 220.

- Schubert, M. *et al.*, 2005. *Determination of radon distribution patterns in the upper soil as a tool for the localization of subsurface NAPL contamination*. Radiation Measurements 40, 633 – 637.
- Schubert, M. *et al.*, 2006. *On-site determination of the radon concentration in water samples: Methodical background and results from laboratory studies and a field-scale test*. Radiation Measurements 41, 492 – 497.
- Schubert, M. *et al.*, 2007. *Radon as a naturally occurring tracer for the assessment of residual NAPL contamination of aquifers*. Environmental Pollution 145, 920 – 927.
- Schwartz, M. C., 2003. *Significant groundwater input to a coastal plain estuary: assessment from excess radon*. Estuarine Coastal and Shelf Science 56, 31 – 42.
- Semprini, L., *et al.*, 2000. *Laboratory, field and modelling studies of radon-222 as a natural tracer for monitoring NAPL contamination*. Transp. Porous Media 38, 223 – 240.
- Sesana, L. *et al.*, 2006. ^{222}Rn as indicator of atmospheric turbulence: measurements at Lake Maggiore and on the pre-Alps. J. Environ. Radioact. 86, 271 – 288.
- Shizuma, K. *et al.*, 1998. *A method for measuring accurate radon concentration in water by means of γ ray spectrometry*. Nuclear Instrument and Methods in Physics Research A 410, 309 – 313.
- Simpson, B. R., 1992. *Guide to the Expression of Uncertainty in Measurement*. 1st edition. International Organization for Standardization, ISO/TAG 4/WG 3.
- Singh, N.P. *et al.*, 1984. *Uranium and radon estimation in water and plants using SSNTD*. Nucl. Tracks Radiat. Meas. 81, 483 – 486.
- Smoak, J. M. and Krest, J. M., 2006. *Source of radium in a well-water-augmented Florida Lake*. J. Environ. Radioact. 89, 102 – 114.
- Snow, D. D. and Spalding, R. F., 1997. *Short-term aquifer residence times estimated from ^{222}Rn disequilibrium in artificially-recharged ground water*. J. Environ. Radioact. 37, 307 – 325.
- Solecki, A.T., 2002. *Gamma spectrometric measurements of radon daughter ^{214}Bi in surface waters*. Geofisica Internacional 41 (3), 339 – 344.

- Speelman, W.J., 2004. *Modelling and measurement of radon diffusion through soil for application on mine tailings dams*. Masters Thesis, University of the Western Cape (unpublished).
- Strom, D.J. and Stansbury, P.S., 1992. *Minimum Detectable Activity when background is counted longer than sample*. Health Phys. 63(3), 360 – 361.
- Suksi, J. 2001. *Natural Uranium as a Tracer in Radionuclide Geosphere Transport Studies*. <http://ethesis.helsinki.fi/julkaisut/mat/kemia/vk/suksi/naturalu.pdf>. A Ph.D. thesis, cited on 25th May.2005.
- Sun, H. and Semkow, T.M., 1998. *Mobilization of thorium, radium and radon radionuclides in ground water by successive alpha-recoils*. Journal of Hydrology 205, 126 – 136.
- Surbeck, H., 1993. *Radon monitoring in soils and water*. Nuclear Tracks Radiation Measurement 22, 463 – 468.
- Surbeck, H., 1995. *Alpha spectrometry sample preparation using selectively adsorbing thin film*. Appl. Radiat. Isot. 53, 97 – 100.
- Surbeck, H., 1995. *Determination of natural radionuclides in drinking water; a tentative protocol*. The Science of the Total Environment 173/174, 91 – 99.
- Takeyasu, M. *et al.*, 2006. *Concentrations and their ratio of ²²²Rn decay products in rainwater measured by gamma-ray spectrometry using a low-background Ge detector*. J. Environ. Radioact. 88, 74 – 89.
- Talha, S.A. *et al.*, 2008. *γ Ray spectrometry of radon in water and the role of radon to representatively sample aquifers*. Appl. Radiat. Isot. 66, 1623 – 1626.
- Taylor, J. R., 1996. *An Introduction to Error Analysis*. 2nd Edition. University Science Books.
- Tommasino, L, 1998. *Passive sampling and monitoring of radon and other gases*. Radiation Protection Dosimetry 78(1), 55 – 58.
- Tommasino, L., 1990. *Radon monitoring by alpha track detection*. Nuclear Tracks 1791, 43 – 48.
- Tsabarlis, C. and Ballas D., 2005. *Online gamma-ray spectrometry at open sea*. Appl. Radiat. Isot. 62, 83 – 89.

- Tuccimei, P. *et al.*, 2005. *Groundwater fluxes into a submerged sinkhole area, central Italy, using radon and water chemistry*. Applied Geochemistry 20, 1831 – 1847.
- Tykva, R. and Sabol, J., 1995. *Low-level environmental radioactivity: sources and evaluation*. Technomic Publishing Company, Lancaster (USA).
- van der Spoel, W. H., 1998. *Radon Transport in Sand: A laboratory study*. A Ph.D. thesis: Technische Unversiteit Eindhoven, The Netherlands.
- van Wijngaarden, M. *et al.*, 2002. *Radiometric sand mud characterisation in the Rhine-Meuse Estuary-part B: in-situ mapping*. Geomorphology 43, 103 – 116.
- Vasarhelyi, A. *et al.*, 1997. *Spatial distribution of radon content of soil-gas and well-water measured with Etched Track radon monitors*. Radiation Measurement 28 (1-6), 685 – 690.
- Venema, L., B. and de Meijer, R., J., 2001. *Radionuclides as tracers of the dispersal of dredge spoil dumped at sea*. J. Environ. Radioact. 55, 221 – 239.
- Vigier, N. *et al.*, 2001. *Erosion timescales derived from U-decay series measurements in rivers*. Earth Planet. Sci. Lett. 193, 549 – 563.
- Vitz, E., 1991. *Towards a standard method for determining waterborne radon*. Health Physics 60, 817 – 829.
- Vlastou, R. *et al.*, 2006. *Monte Carlo simulation of γ ray spectra from natural radionuclides recorded by a NaI detector in the marine environment*. Appl. Radiat. Isot. 64, 116 – 123.
- Vogel, J. C. *et al.*, 1999. *Evaluating the rate of migration of an uranium deposition front within the Uitenhage Aquifer*. Journal of Geochemical Exploration 66, 269 – 276.
- Walton, W. C., 1987. *Groundwater pumping tests*. Lewis Publishers Inc., Michigan.
- Wikipedia, the free encyclopedia. <http://www.reference.com/browse/wiki/Aquifer> (accessed: June 15, 2008).
- Winde, F. *et al.*, 2004. *Gold tailings as a source of waterborne uranium contamination of streams – The Koekemoerspruit (Klerksdorp goldfield, South Africa) as a case study; Part I of III: Uranium migration along the aqueous pathway*. Water SA 30(2), 219 – 225.

Wu, Y., Wen, X., Zhang, Y., 2004. *Analysis of the exchange of groundwater and river water by using Radon-222 in the middle Heihe Basin of northwestern China.* Environmental Geology 45 (5), 647 – 653.

Yoneda, M. *et al.*, 1991. *Location of groundwater seepage points into a river by measurement of ^{222}Rn concentration in water using activated charcoal passive collectors.* Journal of Hydrology 124 (3-4), 307 – 316.

Yoneda, M. *et al.*, 1994. *Quantitative measurement of ^{222}Rn in water by the activated charcoal passive collector method: The effect of water in a collector.* Journal of Hydrology 155 (1-2), 199 – 223.

Zahorowski, W. *et al.*, 2004. *Ground based radon-222 observations and their application to atmospheric studies.* J. Environ. Radioact. 76, 3 – 33.

Zalewski, M. *et al.*, 2001. *Study of ^{222}Rn concentrations in drinking water in north-eastern hydro-regions of Poland.* J. Environ. Radioact. 53, 167 – 173.

Zereshki, A., 1983. *The solution of ^{222}Rn by groundwaters.* A Ph.D. thesis, University of Bath (unpublished).

Zhuo W. *et al.*, 2001. *Occurrence of ^{222}Rn , ^{226}Ra , ^{228}Ra and U in groundwater in Fujian Province, China.* J. Environ. Radioact. 53, 111 – 120.

www1: Vaal River, <http://en.wikipedia.org/w/index.php> (cited Nov. 22, 2008).

www2: <http://www.ewater.co.za/misc/RiverVaal/defaultgeo.htm>. Cited 22 Nov. 2008.